INFORMATION TO USERS

This manuscript has been reproduced from the microfilm master. UMI films the text directly from the original or copy submitted. Thus, some thesis and dissertation copies are in typewriter face, while others may be from any type of computer printer.

The quality of this reproduction is dependent upon the quality of the copy submitted. Broken or indistinct print, colored or poor quality illustrations and photographs, print bleedthrough, substandard margins, and improper alignment can adversely affect reproduction.

In the unlikely event that the author did not send UMI a complete manuscript and there are missing pages, these will be noted. Also, if unauthorized copyright material had to be removed, a note will indicate the deletion.

Oversize materials (e.g., maps, drawings, charts) are reproduced by sectioning the original, beginning at the upper left-hand corner and continuing from left to right in equal sections with small overlaps.

Photographs included in the original manuscript have been reproduced xerographically in this copy. Higher quality 6" x 9" black and white photographic prints are available for any photographs or illustrations appearing in this copy for an additional charge. Contact UMI directly to order.

Bell & Howell Information and Learning
300 North Zeeb Road, Ann Arbor, MI 48106-1346 USA
800-521-0600

Development of Grating Light Reflection Spectroscopy For Chemical Sensing Applications

Sean A. Smith

A dissertation submitted in partial fulfillment of the
requirements for the degree of

Doctor of Philosophy

University of Washington

2000

Program Authorized to Offer Degree: Department of Chemistry

In presenting this dissertation in partial fulfillment of the requirements for the Doctoral degree at the University of Washington, I agree that the Library shall make its copies freely available for inspection. I further agree that extensive copying of the dissertation is allowable only for scholarly purposes, consistent with "fair use" as prescribed in the U.S. Copyright Law. Requests for copying or reproduction of this dissertation may be referred to Bell and Howell Information and Learning, 300 North Zeeb Road, Ann Arbor, MI 48106-1346, or to the author.

Signature 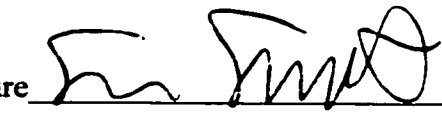

Date June 8th, 2000

University of Washington
Graduate School

This is to certify that I have examined this copy of a doctoral dissertation by

Sean A. Smith

and have found that it is complete and satisfactory in all respects,
and that any and all revisions required by the final
examining committee have been made.

Chair of Supervisory Committee:

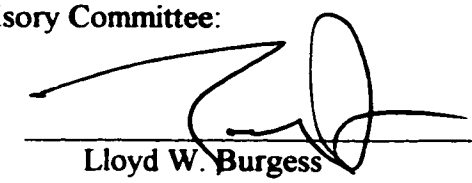

Lloyd W. Burgess

Reading Committee:

Lloyd W. Burgess

Charles B. Campbell

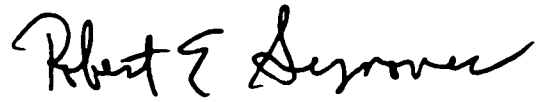

Robert E. Synovec

Date: June 8, 2000

University of Washington

Abstract

Development of Grating Light Reflection Spectroscopy

For Chemical Sensing Applications

by Sean A. Smith

Chairman of the Supervisory Committee: Professor Lloyd W. Burgess

Department of Chemistry

Grating Light Reflection Spectroscopy (GLRS) exploits the interaction of light with a transmission diffraction grating in contact with a sample. With this technique, light reflected from the grating exhibits a redistribution of spectral intensity and phase dependent upon the bulk dielectric properties (refractive index and absorbance) of the sample. The use of a transmission diffraction grating makes GLRS unique within the field of reflection-based optical measurements, in that it can operate at the critical point of reflection sensitivity to sample properties regardless of the state of the reflection interface. In addition, recent theoretical advances have demonstrated the ability of GLRS to make absolute determinations of the size and concentration of scattering inhomogeneities in the sample matrix. These properties make GLRS attractive as a sensor in complex or difficult analytical environments due to its relative insensitivity to fouling layers and by its ability to characterize the bulk properties of optically dense and/or heterogeneous matrices.

Recent efforts have implemented GLRS as an on-column detector for samples flowing through rectangular micro-channels 100 microns wide by 10 microns deep. This has resulted in a significant enhancement of measurement precision, so that the technique may take full advantage of its inherent sensitivity. The coupling of this performance enhancement to the theoretical development mentioned above has resulted in sub-nanometer determinations of the radii of dendrimeric particles in aqueous solvent at concentrations that prohibit the use of transmission-based particle sizing techniques. These experiments led to the use of GLRS as an "in-column" liquid chromatography detector, where it proved useful in the identification and quantitation of absorbing and non-absorbing analytes. Building upon these advances, initial steps toward the embodiment of GLRS in a self-contained probe have shown great promise with respect to the creation of a rugged, sensitive, and versatile chemical sensor.

Table of Contents

List of Figures

List of Tables

Chapter 1

Introduction and Overview

1.1 Introduction

Grating Light Reflection Spectroscopy (GLRS) provides a simple, robust method for determining the optical properties of a sample based upon the interaction of light with a transmission diffraction grating in contact with that sample. This technique operates even in opaque solutions, because sample-induced changes in the transmitted portion of the diffracted incident beam are monitored in a reflected order. Furthermore, a rigorous optical theory has been developed that can provide absolute determinations of the refractive index and absorbance of the sample, along with the size and concentrations of any heterogeneities (i.e. solid particles) within the sample medium. These determinations can be made rapidly and in a variety of implementations without disturbing the sample. Therefore, GLRS is ideally suited for use as a sensing probe in demanding industrial processes or for field work.

There are no constraints in the materials out of which a GLRS interface can be made, except that a regular permittivity modulation exist at the interface in order to create diffracted light that can undergo a transition from traveling waves to evanescent ones.

Thus the substrate and "permittivity modulator" can be made out of materials that are either inert to the sample matrix or selective for some desirable component of that matrix. This makes GLRS attractive for the determination of bulk optical properties in specialized applications where a particularly harsh environment would preclude similar techniques such as ATR or SPR. It also makes GLRS attractive as a general-purpose sensor, because the materials of its interface can be chosen so that it exhibits a continuous and virtually constant sensitivity to sample optical properties across the electromagnetic spectrum from the UV to the near IR.

The performance enhancement for GLRS in bulk media relative to other reflection-based evanescent wave sensors results from the fact that GLRS to date remains the only true critical point sensor. The critical point is the position in angle and wavelength space at which an incident beam transitions from propagating across a reflection/transmission interface to becoming evanescent, at which point its electric field vector is oriented normal to the interface. This is analogous to the onset of Total Internal Reflection (TIR) of the incident light. In this circumstance, the light no longer exists as a transverse electromagnetic wave. Instead, it is an exponentially decaying electric field normal to the interface. The amplitude of this field vector oscillates parallel to the interface, resulting in a time-average of zero energy propagated across the interface – unless it is absorbed or scattered by the sample within the period of an oscillation. At angles and/or wavelengths above the critical one this evanescent condition still holds; however, the penetration depths of these waves decrease rapidly.

1.2 The Field of Total Internal Reflection Chemical Sensors

The transition between internal and external reflection cannot be maintained at a single point in angle or wavelength space during contact with a sample medium in which the refractive index is changing. Therefore, all reflection techniques operate well above the critical point to ensure that the measurement remains stable. This is done at the expense of the penetration depth of the electric field. Even though the effective pathlength of a measurement can be increased by increasing the interaction length of the evanescent wave with the sample medium, the small penetration depth per reflection makes such measurements extremely sensitive to changing properties of the interface layer. This can be advantageous, as in for example biological assays, where a selective layer deposited on the reflection interface ensures that the evanescent wave sees only that layer. However, for bulk solution measurements this property is obviously a hindrance, since even a minute fouling layer will disrupt the measurement.

To date, only one other true critical point has been developed. However, it was inhibited by the fact that it required the measurement of the differential intensities of the transmitted and reflected portions of an incident laser beam positioned near the critical angle. The noise content of the transmitted beam due changing sample turbidity made this

"critical angle" sensor of limited use.[1] GLRS overcomes this problem by using the dispersive properties of the diffraction grating to maintain the critical condition independent of the measurement beam.

Unlike the other techniques that exploit TIR-type phenomena, GLRS relies not on attenuation of its sampling beam, but on the loss of coherence of the penetrating evanescent wave relative to the wave that originates at the grating. In this way there is no problem measuring high absorbances, as there is with transmission measurements. This contrasts with the attenuation mechanism of SPR, in which it has been demonstrated that phase measurements are extremely difficult because of the lack of light present at the SPR reflection minimum.[2] In such cases the low signal to noise resulting from the decreased fringe amplitudes completely erases any sensitivity increase from the phase measurement. However, the "coherence loss" mechanism suggests that phase-sensitive measurements are possible with GLRS: this principle has been demonstrated with monochromatic light as the sampling beam. This result holds promise for the construction of extremely sensitive GLRS sensors that would compete with conventional interferometric approaches.

---

[1] Schipper, E. F.; Kooyman, R. P. H.; Borreman, A.; Greve, J. *Biosensors & Bioelectronics*, **1996**, vol. 11, no. 3, pp. 295-304.

[2] Nelson, S. G.; Johnston, K. S.; Yee, S. S. *Sensors and Actuators B*, **1996**, vol. 35-36, pp.187-191.

It is this coherence loss mechanism that is also responsible for the high sensitivity of GLRS measurements to very small particles with radius << wavelength, which is the size regime where incident beam coherence changes upon scattering are the greatest. The fact that GLRS is a reflection technique also allows it to operate in high scattering concentrations. In fact, GLRS becomes more sensitive to scattering particles at higher concentration. This is in general true for all scattering measurements. However, transmission methods have a relatively narrow "window" of particle concentrations in which to conduct measurements due to the relatively long path length the light must travel through the sample. Within this volume, the number of scatterers present must be large enough to cause appreciable scattering but still low enough to avoid the erroneous size predictions that result from scattering of the light by more than one particle in a dense collection of particles. This practical limit is less than 1% volume fraction for most optical transmission-based methods. Only fiber-optic based Photon Correlation Spectroscopy (PCS) has demonstrated the same degree of size determination sensitivity as GLRS at high particle concentrations.[3] However, with GLRS the experimental parameters are fewer and simpler to determine,[4] since the viscosity of the particle matrix

---

[3] Allen, T. *Particle Size Measurement, Volume 1*, 5th edition, Chapman & Hall, London, **1997**, pp. 426-436.

[4] Smith, S. A.; Brodsky, A. M.; Burgess, L. W. "Nanoparticle Characterization in Nanoliter Volumes", submitted to *Analytical Chemistry*, April, **2000**.

does not need to be known and far fewer measurements are required for statistical accuracy.[5]

GLRS also exhibits a much broader dynamic range with respect to other optical sensing schemes. A prototypical GLRS immersion probe is capable of a linear refractive index response range from 1 to 1.7 with no moving parts – this range covers virtually all industrially and environmentally significant gas and liquid phase samples. This is in sharp contrast to SPR sensors, in which the sensitivity to refractive index is not linear with respect to wavelength or coupling angle, except over a narrow measurement range;[6] furthermore, SPR sensors have a dynamic range of at most roughly 0.3 refractive index units.[7] GLRS also has a fairly broad dynamic range with respect to absorbance, covering the range from 0.1 to over 200 A.U.

Furthermore, the detection limits of all currently available refractive index sensors are limited by temperature changes, and mechanical instability of the optical trains and/or sensing interface, so that the decision to use one or another particular measurement methodology is ultimately based upon one's personal preference and not upon the

---

[5] De Jaeger, N.; Demeyere, H.; Finsy, R.; Sneyers, R.; Vanderdeelen, J.; van der Meeren, P.; van Laethem, M. *Particle and Particle Systems Characterization*, **1991**, vol. 8, pp. 179-193.

[6] Jung, L. S.; Campbell, C.; Chinowsky, T. M.; Mar, M. N.; Yee, S. S. *Langmuir*, **1998**, vol. 14, no. 19, 15 Sept., pp. 5636-5648.

[7] Jorgenson, R. C. *Surface Plasmon Resonance Based Bulk Optic and Fiber Optic Sensors*, Ph.D. Thesis, University of Washington, **1993**, p. 97.

analytical perfomance of the instrument. (This is not to say that particular techniques, when used by an experienced practitioner in a well-controlled laboratory experiment, will not show significant benefits or drawbacks with respect to other implementations.) For example, integrated optical SPR[8] and grating-coupler[9] sensor implementations have calculated theoretical refractive index detection limits on the order of 10^{-6} or 10^{-7} RIU, but virtually all integrated optics setups have reported detections limits on the order of 10^{-4} to 10^{-5} RIU due to difficulties in controlling signal drift during a measurement. Indeed, sensor configurations are now available commercially based on SPR,[10] grating-coupler,[11] and "resonant mirror"[12] (basically a Mach-Zender interferometer), implementations, but they all exhibit approximately these same detection limits.[13]

To date, all of these sensors have been concerned only with measuring the real part of the complex refractive index. Thus, they provide no information about potential

---

[8] Harris, R. D.; Luff, B. J.; Wilkinson, J. S.; Piehler, P.; Brecht, A.; Gauglitz, G.; Abuknesha, R. A. *Biosensors & Bioelectronics*, **1999**, vol. 14, no. 4, pp. 377-386.

[9] Brynda, E.; Houska, M.; Brandenburg, A.; Wikerstal, A.; Skvor, J. *Biosensors & Bioelectronics*, **1999**, vol. 14, no. 4, pp. 363-368.

[10] BiaCore AB in Uppsala, Switzerland.

[11] ASI, Zurich, Switzerland.

[12] Affinity Sensors, Ltd., Cambridge UK.

[13] Melendez, J.; Carr, R.; Bartholomew, D. U.; Kukanskis, K.; Elkind, J.; Yee, S. S.; Furlong, C.; Woodbury, R. *Sensors & Actuators B*, **1996**, vol. 35-36, pp. 212-216.

absorption properties of a sample. Some attempts have been made to quantitiate absorption with the SPR technique, using the fact that the depth of the reflection minimum is inversely proportional to sample-induced losses in the energy of the SPR resonance wavelength. However, these techniques are hampered by the fact that anomalous dispersion of the refractive index that occurs with such absorption losses causes significant distortion of the SPR resonance "dip", requiring more complicated data analysis.[14] In addition, the sensitivity of the technique to absorbance is limited to approximately 3 A.U., though it does possess an extremely broad dynamic range of nearly 2000 A.U. because "SPR is a surface phenomenon, and is therefore relatively insensitive to bulk absorbance."[15] Finally, some recent work involving Cavity Ring-Down Spectroscopy (CRDS) has extended this technique to use with condensed phase samples by altering the method from a transmission-based measurement to a TIR strategy. CRDS is extremely sensitive to gas phase samples when used in transmission mode, however, such an implementation can only measure absorption losses at one wavelength within a given CRDS sampling cell. (Initiating a measurement at a different wavelength would require changing the laser source and changing the dimensions of the ring-down cavity.) By transferring the principles of the technique to a TIR measurement,

---

[14] Hanning, A.; Roeraade, J.; Delrow, J. J.; Jorgenson, R. C. *Sensors & Actuators B*, **1999**, vol. 54, pp. 25-36.

[15] Karlsen, S. R.; Johnston, K. S.; Jorgenson, R. C.; Yee, S. S. *Sensors & Actuators B*, **1995**, vol. 24-25, pp. 747-749.

CRDS can be used in a quasi-broadband format to achieve fairly impressive limits of detection for an evanescent wave measurement: detection on the order of several ppm has been reported.[16] GLRS measurements, though, have yielded detection limits on the ppb level (see below). Again, this is because GLRS is a true critical point measurement. All other TIR methods operate above the critical angle/wavelength for stability purposes, and so are not capable of the sensitivity observed with GLRS. The CRDS method furthermore provides no information about the refractive index of a sample.

Therefore, a need exists within the field of optical detectors for a technique that possesses enough sensitivity to absorbing and non-absorbing materials to yield reliable, bulk-sample measurements in circumstances that preclude the use of conventional spectroscopic methods. GLRS is well suited to occupy this niche, since its simple, versatile, and durable interface allows it to operate in environments that would otherwise require a combination of more complicated techniques. For example, a recent study that combined an SPR measurement with a sophisticated specular reflectance bulk optic apparatus was able to obtain complete complex refractive index spectra (i.e. refractive index and absorbance dispersions) on highly concentrated liquid samples within the visible region of the spectrum, with the goal of implementing such a setup as an on-line

---

[16] Pipino, A. C. R. *SPIE Conference on Advanced Sensors and Monitors for Process Industries and the Environment*, SPIE vol. 3535, **1998**, pp. 57-67.

industrial process instrument.[17] However, because the specular reflectance measurement is not a critical point determination, this method is only applicable for extremely concentrated analytes, whereas GLRS has a broader dynamic range with respect to refractive index and absorbance determinations (albeit over a narrow range of wavelengths per measurement). Furthermore, GLRS has the added property of being useful for determining the size and concentration of heterogeneities in a sample matrix. Finally, the complexity of the SPR/reflectance apparatus would prevent its implementation as a remote or hand-held sensor, while GLRS is ideally suited for such use.

The GLRS interface also allows for the easy implementation of various instrument modulation strategies. For example, in a recent collaboration with Sandia National Laboratories, a gold layer deposited directly on to the GLRS diffraction grating formed part of an electrochemical cell. Electrical modulation of the cell's potential generated oxidized forms of an electro-active molecule near the grating interface that exhibited significant absorption at the GLRS evanescent wavelength. This sample modulation technique led to concentration determinations of 50ppb for an electro-active dye molecule. This result shows that similar experiments performed in the near UV, where many organic species of interest absorb light very strongly, could be implemented

---

[17] Peiponen, K.; Raty, J.; Vartainen, E. M.; Sugiura, T.; Kawata, S. *Measurement Science and Technology*, 1999, vol. 10, N145-N148.

with a remote GLRS probe to conduct measurements at trace concentration levels in aqueous environments (e.g. ground water contamination monitoring).

1.3 Overview of Thesis Work

Work done previous to this thesis demonstrated the principles of GLRS as a multipurpose optical detector for sample refractive index, absorption, and homogeneity (i.e the average size and concentration of any particles present).[18,19,20]

Upon completion of this basic characterization work, an Applied Spectroscopy Focal Point article was published to mark the significant level of maturity that the technique had achieved.[21] However, work still needed to be done to determine the sensitivity of GLRS to these components, as well as the optimal method by which to analyze GLRS data. These efforts, with refractive index perturbing samples, absorbing dyes, and very small scattering particles, found that simple equations derived from the

---

[18] Anderson, B. B.; Brodsky, A. M.; Burgess, L. W. *Analytical Chemistry*, **1996**, vol. 68, no. 7, pp. 1081-1088.

[19] Anderson, B. B.; Brodsky, A. M.; Burgess, L. W. *Physical Review E*, **1996**, vol. 54, no. 1, pp. 912-923.

[20] Anderson, B. B.; Brodsky, A. M.; Burgess, L. W. *Langmuir*, **1997**, vol. 13, no. 15, 1 Aug, pp. 4273-4281.

[21] Brodsky, A. M.; Burgess, L. W.; Smith, S. A. *Applied Spectroscopy*, **1998**, vol. 52, no. 9, pp. 332A-343A.

GLRS optical theory, when fitted to the reflection spectra, returned accurate and absolute determinations of their properties. The most significant results of these experiments were the wide and linear dynamic range with respect to refractive index, the wide dynamic range with respect to absorbance, and the extreme sensitivity (< 1nm) to particle size at high particle concentrations. Additionally, experiments were done to demonstrate the phase dependence of the reflected light on the changes occurring in the critical diffraction order. This result, in addition to confirming the theoretical interpretation of the GLRS technique as a coherence (and not an attenuation) measurement, implies that the extreme sensitivity inherent in phase (i.e. interferometric) measurements could be exploited with GLRS.

Furthermore, having demonstrated the proof of principle of the technique, the utility of the method within the field of analytical measurements needed to be demonstrated. This was done by implementing GLRS as a detector for a micro-capillary liquid chromatography device. These experiments showed that GLRS detection of the chromatographic eluents exhibited both quantitative and qualitative information on the chemical species present in the column. Absorbing and non-absorbing analytes could be differentiated based upon their reflectivity versus wavelength response, while the amount of analyte present could be determined fairly sensitively by summing the GLRS response versus the analyte elution time. In fact, the GLRS sensitivity with respect to absorbance proved to be within an order of magnitude of the sensitivity of a transmission-based absorbance measurement conducted on the same system.

Finally, construction has begun of a self-contained GLRS immersion probe, where for the first time the technique will be realized as an instrument independent from the sample cell. This work has necessitated the consideration of how best to implement the GLRS technique as a sensitive and broadly applicable sensor.

This thesis will cover in detail the above-mentioned developments in the practice and application of GLRS as both a technique and an instrument. Chapter 2 discusses those theoretical details that have the most significant impact on the gathering and analysis of GLRS data. This will include particular elements of optical theory that allow for a deeper understanding and appreciation of the GLRS instrumentation and of the type of information that GLRS can provide about an analyte of interest. Chapter 3 describes the benchtop GLRS apparatus constructed to determine the method's response to various types of analytes. A general description of the type of reflection spectra generated by this apparatus is given in Chapter 4, along with a discussion of the sensitivity of the GLRS response to analyte optical properties. Chapter 5 includes the results of experiments performed with nanometer-scale scattering particles that demonstrate the application of the theory to the reflection spectra in order to extract the optical properties of the analytes. Then Chapter 6 details the implementation of GLRS as a micro-capillary liquid chromatography detector. The discussion concludes in Chapter 7 with an overview of how best to implement GLRS as an independent probe-type sensor, since this appears to be its most promising niche within the family of optical spectroscopy techniques.

Chapter 2

GLRS & Related Optical Theory

2.1 Introduction

This chapter provides a summary of the optical concepts that are likely to arise when conducting GLRS measurements, and then describes the mathematical relationships that are particular to GLRS itself. The mechanism through which GLRS operates involves several ideas that are usually discussed separately in the literature, so that a good deal of effort is required to form a simple, coherent, and reasonably complete picture of *"what is going on"* when one employs this technique. Therefore, this chapter will not merely list off the concepts; it will try to relate them to each other as intuitively as possible. The explanations will concentrate more on verbal, qualitative descriptions of phenomena (and it is therefore rather long), since one may consult the many textbooks available on the subject of optics and the interaction of light with matter[22,23,24,25,26,27,28] to

---

[22] Born, M.; Wolf, E. *Principles of Optics*, 3rd Edition, Pergamon Press Ltd., Oxford, **1965**.

[23] Garbuny, M. *Optical Physics*, Academic Press Inc., New York and London, **1965**.

[24] Ditchburn, R. W. *Light*, Dover Publications Inc., New York, **1991**.

[25] Van de Hulst, H. C. *Light Scattering by Small Particles*, John Wiley & Sons Inc., New York, **1957**.

[26] Hutley, M.C. *Diffraction Gratings*, Academic Press Inc., New York and London, **1982**.

find more elaborate quantitative derivations. The discussion will include only those equations that are the most central and most general to the application of optical phenomena for quantitative materials analysis.

Finally, note that some texts may interchange designations of certain quantities: this is a too-frequent trend in the literature, whereby authors will denote the same quantity by different and sometimes contradictory representations! This tendency is very frustrating to the student attempting to learn this material, so that much of the apparent difficulty of understanding the concepts actually results merely from this inconsistent transfer among authors of supposedly standard quantities and derivations. Therefore, this chapter attempts to alert the reader of these occurrences, but one must ultimately refer to the literature (and all of the detective work which that imposes) to resolve *apparently* conflicting notations.

2.2 Representation of Plane Waves and Complex Notation

The theoretical discussion begins with the description of transverse plane waves and complex numbers, because an intuitive understanding of these two concepts will make virtually all aspects of the optical theory that follows in the sections below much easier to grasp.

---

[27] Harrick, N. J. *Internal Reflection Spectroscopy*, Harrick Scientific Corporation, New York, **1979**.

[28] Pedrotti, F. L.; Pedrotti, L. S. *Introduction to Optics*, Prentice-Hall Inc., Englewood Cliffs, **1987**.

First, even though quantum mechanics has shown that light behaves as both a wave and a particle, for practical purposes the wave characteristic alone suffices to describe light of optical and infrared frequencies. Therefore, we can represent light by the basic equation for a sinusoidal plane wave:

$$A(x,t) = A_0 \sin 2\pi\left[vt - \left(\frac{x}{\lambda}\right)\right] \qquad (1)$$

Here the amplitude A(x) of the wave as a function of distance traveled x is seen to be equal to the initial amplitude of the wave A_0 multiplied by a sinusoidally varying phase term. This phase term includes a time varying component *vt* and a component that varies with distance x/λ. Note that this is the most general description of a wave, and that in most optical measurements either the time or the distance component is effectively held constant. Thus, the equation above will usually be only time-dependent:

$$A(t) = A_0 \sin(2\pi vt + \delta) \qquad (2)$$

or distance-dependent:

$$A(x) = A_0 \sin\left(\frac{2\pi x}{\lambda} + \phi\right) = A_0 \sin(kx + \phi) \qquad (3)$$

where the two phase-offset constants δ and ϕ are included to reflect the fact that in most measurements the phase of the light is arbitrary. Here the wavelength constant (or propagation constant) $k = 2\pi/\lambda$ has been introduced, since many authors in the optical literature use it in place of λ for mathematical convenience. This notation can be

confusing, however, since the same letter k is used to refer to the extinction coefficient and the attenuation index (see below).

Note that equations (1), (2), and (3) state the phase-dependent amplitude of the wave as a scalar quantity, even though light of course has a direction of propagation and is thus fully expressed as a vector. Thus, the literature also defines a wave vector $\vec{k}$ that is equal in magnitude to this wavelength constant, and is simply the product of k and a unit vector **s** in the direction of propagation of the wave. (This unit vector is usually denoted by **s** because it is related to Poynting's Vector **S** - see below.) Finally, note that the wavelength of light in a medium is dependent upon the speed of light in that medium, since energy (and thus frequency) must be conserved in all physical interactions. The speed of light in a particular medium is usually represented by a refractive index n, which is the ratio of the speed of light in a vacuum to that in the medium (see the section on Maxwell's equations below).

Therefore, we can represent k by:

$$k = \frac{2\pi}{\lambda_0} n = \frac{2\pi}{\lambda} \qquad (4)$$

where λ_0 is the wavelength of light in vacuum and λ is the wavelength in the medium being considered. Note that, since all media are more dense than a vacuum, n is (usually) greater than 1 (except in some metals, see below). Therefore the wavelength of a beam of light will become shorter upon traveling from a vacuum to a medium, so that its frequency increases and energy is conserved (remember $E = h\nu$, where h is Planck's

constant and ν is the photon frequency) despite the slower rate of transmission of the light energy through the medium.

The equations above are sufficient to describe a single monochromatic beam of light: it has an amplitude, a phase, and a frequency. To describe the interaction of such a wave with another wave at a particular point in space or time, one merely has to sum up the amplitudes and phases of the two waves to see what the result of that interaction will be. This may be done trigonometrically by using the properties of vectors. Here, the amplitudes of the waves are translated into the magnitude of a two-dimensional vector, and the phases are translated into directions or angles for each vector. This translation becomes immediately intuitive when one considers that a line may be drawn from the origin of the propagation axis to the crest of the wave, and the length of this line, i.e. its "magnitude", is equal to the amplitude term of the wave equation. Likewise, the phase term of the wave equation above is in fact an "angle" that varies from 0 to 2π radians (or 0 to 360 , depending upon what notation you are most comfortable with).

Vector operations on these waves are most conveniently done using the properties of complex numbers, which are represented by

$$z = x + iy \qquad (5)$$

where the complex number z is composed of a real part x and an imaginary part y. Note that, when complex notation is applied to physically observable relationships, the variables x and y are themselves each "real" quantities: they just happen to be related to each other in a way that is conveniently expressed via complex notation as a "real" and

an "imaginary" component of a complex number. It is also useful to define the complex conjugate, z^*, of the complex number z:

$$z^* = x - iy \qquad (6)$$

With this, the modulus or absolute value of the complex number is defined as:

$$|z| = \sqrt{z \cdot z^*} \qquad (7)$$

Because complex numbers are a mathematical construct, the modulus is defined in order to extract a physically observable quantity from the "complex" relationship between the two variables x and y.

Complex numbers are used in optics because they render many cumbersome equations much easier to understand and work with. Much of the convenience results from the way they operate on the trigonometric functions that often arise in the mathematics that describes the generation and interaction of light with matter. For example, all of the fundamental processes that light may undergo, such as reflection, refraction, absorption, and scattering may be best understood geometrically as the interaction between two or more "wave-vectors": quantities with a direction and magnitude that behave like waves in their interactions with each other. However, many of the equations that are necessary to quantitate these phenomena become unnecessarily complicated by trigonometric identities. Therefore, the discussion will now focus on those properties of complex numbers that aid in the manipulation of "wave-vector"

quantities by showing how the wave equations (1,2,3) listed above are translated into complex notation.

The sinusoidal equations described above are convenient for representing the wave nature of light, because when plotted versus phase angle they result in the familiar undulating pattern associated with waves. However, as mentioned above, this representation is not very convenient for manipulating any but the most basic equations involved in the propagation and interaction of light in matter. Complex vector notation makes such manipulations simple according to the following identities:

$$Ae^{i\phi} = A(\cos\phi + i\sin\phi) \qquad (8)$$

and

$$A_3e^{i\phi_3} = A_1e^{i\phi_1} + A_2e^{i\phi_2} \qquad (9)$$

where

$$\phi = (\nu t + kx) \qquad (10)$$

so that the time and distance dependent terms are both included in this representation. Here it is seen that sinusoidal waves are mathematically equivalent to a complex exponential function $e^{i\phi}$. Furthermore, the resultant $A_3e^{i\phi_3}$ of the interaction between two such waves $A_1e^{i\phi_1}$ and $A_2e^{i\phi_2}$ can be determined merely by adding them together. When expressed in this form, light waves are denoted by their amplitude A and their phase or phase-angle ϕ. Figure 2.1 show their graphical depiction in the complex plane by drawing them on an Argand Diagram (named for its inventor) as vectors of length A that are

rotated ϕ degrees relative to the real or x-axis. The sinusoidal variation in amplitude with phase is found by calculating the vector's projection on the imaginary or y-axis. Figure 2.2 shows how the components of the complex vector notation relate to their counterparts in the sinusoidal notation for a plane wave.

Finally, note that when applied to light waves, the amplitude A in the equations above represents the magnitude of the electric field energy generated by the photon of light, so that the light wave is often represented as $Ee^{i\phi}$. Light has both electric and magnetic fields (this is discussed in the next section), but it is the interaction of matter with the electric field of light that dominates most optical measurement applications. Furthermore, in virtually all spectroscopic measurements, the Intensity, rather than the Amplitude, of the light is actually measured. Intensity is defined as the amount of energy passing through or impinging upon a surface of unit area (i.e. meters^2) per second. This quantity is equal to the square of the amplitude, so that the intensity of a measured wave using the complex notation above is simply the complex amplitude multiplied by its complex conjugate:

$$I = A^2 = Ae^{i\phi} \times Ae^{-i\phi} = A^2 e^{i(\phi-\phi)} = A^2 \qquad (11)$$

Also, note from Figure 2.2 that the phase angle ϕ may be calculated from:

$$\phi = \tan^{-1}\left(\frac{iy}{x}\right) \qquad (12)$$

$$y = \sin\phi, x = \cos\phi \qquad (13)$$

Thus, one can see that the complex vector notation allows for the simple calculation of the amplitude and phase of a wave.

Having introduced this complex notation for waves and their interaction, the next section will show how these mathematical concepts are actually applied to quantifying the interaction of light with matter.

2.3 The Electromagnetic Theory of Light

By the nineteenth century, light was generally thought of as an energy-carrying wave that (unlike sound waves) could propagate through a vacuum as well as through most forms of matter, though at different speeds. The concepts of reflection, refraction, absorption, interference and polarization of light had been introduced.

However, the exact relationships between these quantities had not been determined until James Clerk Maxwell summarized a set of relatively simple equations to quantitate the behavior of electric charges in space and at boundaries between different types of material. One of the consequences of his derivations was a constant c representing the speed of electromagnetic waves in vacuum that happened to have the same value as the independently determined speed of light. Thus, Maxwell determined that light does indeed consist of electromagnetic waves, and furthermore that these waves are composed of an electric (depending on the separation of charges in space) and a

magnetic (depending on the relative movement of those charges) vector directed normal to the direction of propagation of the energy in the wave.

Historically, these vectors are denoted by **E** and **H** respectively in vacuum, and are replaced by the vectors **D** and **B** in physical media. The electric and magnetic components of the wave have equal amplitudes in vacuum, but this is usually not the case in any other medium. In addition, these vectors are mutually perpendicular to each other and oscillate in phase with each other. The direction and magnitude of the energy flow generated by these oscillating fields is denoted by Poynting's vector, **S** (or **G**!), which is proportional to the vector product of the fields: $\mathbf{S} \approx \mathbf{E} \times \mathbf{H}$ (see figure 2.3). The magnitude of this quantity represents the amount of energy crossing a unit area per second, and is equal to the more familiar optical unit of Intensity (or Power, i.e. Joules/m^2s).

Other properties of interest that are determined by Maxwell's equations include the three so-called material constants ε, μ, and σ. The dielectric constant (or dielectric permittivity) ε is of the most interest to chemical spectroscopists, since it may be broken up into terms for the "optical constants" of a given substance: the refractive index n and attenuation index K (these will be described in more detail shortly). Furthermore, the parameters μ and σ are small compared to ε in most materials, except for magnetic metals. Two of these constants, ε and μ, combine to determine the velocity v of electromagnetic waves by

$$n_m = \frac{c}{v} = \sqrt{\frac{\varepsilon_m \mu_m}{\varepsilon_0 \mu_0}} \qquad (14)$$

in a medium of refractive index n_m. Since the magnetic permeability is equal to or very near the magnetic permeability of vacuum for most substances, the term μ_m / μ_0 reduces to 1, and so the refractive index is usually related to the dielectric constant by $n_m^2 = \varepsilon_m$, where ε_0 is implicitly included so that n is unitless. This is the same refractive index as used in Snell's Law. Finally, the conductivity σ obviously relates to the presence of free conduction electrons in a material, and is very close to 0 in most non-metallic and non-ionized substances.

As mentioned above, the dielectric constant contains terms for both the refractive index and the attenuation index. Therefore, the dielectric constant is only equal to the square of the refractive index in a medium that does not attenuate the light passing through it (i.e. it is transparent). Otherwise, we must adopt a complex refractive index of the form

$$\eta = n + iK \qquad (15)$$

Authors use various forms of this relationship, including $= n - iK$, $= n(1+iK)$, and $= n(1-iK)$; however, they all represent the same properties. Although it may be obvious, the reader is reminded that this complex refractive index no longer bears the $n^2 = \varepsilon$ relationship to the dielectric constant as the "Snell's Law" refractive index. Instead, the dielectric constant may be separated into real and imaginary parts according to:

$$\varepsilon = \eta^2 = (n + iK)^2 = n^2 - K^2 + i2nK \qquad (16)$$

so that:

$$\varepsilon_{Real} = n^2 - K^2, \varepsilon_{Imag} = i2nK \qquad (17)$$

However, chemists prefer to use n and K directly, since the magnitude of K is always much less than n in all substances except for pure metallic solids. Note that the dielectric constant ε can be expressed in terms of the optical parameters n and K by:[29]

$$n = \sqrt{\frac{\sqrt{\varepsilon_R^2 + \varepsilon_I^2} + \varepsilon_R}{2}} \qquad (18)$$

$$K = \sqrt{\frac{\sqrt{\varepsilon_R^2 + \varepsilon_I^2} - \varepsilon_R}{2}} \qquad (19)$$

Inspection of these equations reveals that if ε_I becomes insignificant, n again becomes equal to the square root of the dielectric constant ($n^2 = \varepsilon$) and K approaches zero. Notice that even though the parameters of Maxwell's equations are often stated as constants, the dielectric "constant" ε is actually a function of frequency, as are the components of the complex refractive index. This fact is accounted for in the so-called *dispersion* equations, which I discuss below. Now, however, I will continue the derivation of the attenuation index K (also known as the extinction coefficient or any

---

[29] For an excellent and extensive derivation of these equations, see: Pedrotti, F. L.; Pedrotti, L. S. *Introduction to Optics*, Prentice-Hall Inc., Englewood Cliffs, 1987.

combination of the words attenuation, absorption, extinction, index, and coefficient), by relating it to the absorption coefficient k, which is more familiar to chemists. The relationship is straightforward:

$$\frac{I(z)}{I_0} = e^{-kz} = e^{-\frac{2\omega}{c}Kz} \qquad (20)$$

Here the intensity loss of an incident light beam I_0 as it travels into a medium with the attenuation index K is seen to be an exponential function of z, the distance traveled. This makes the equality between k and K

$$k = \frac{2\omega}{c}K = \frac{4\pi}{\lambda_0}nK = \frac{4\pi}{\lambda}K \qquad (21)$$

where the usual relationships between circular frequency ω, wavelength λ, the speed of light c and refractive index n have been assumed. This simple equality becomes somewhat more complicated, however, when the form of k is restated in terms of Beer's Law as part of the Absorbance, A. This is because A is equal to $\log\left(I_0/I\right)$. Therefore, some mathematical juggling is required to correlate A with K or k:

$$\log\frac{I_0}{I} = A \rightarrow \frac{I_0}{I} = 10^A \rightarrow \frac{I}{I_0} = 10^{-A} = e^{-kz} \qquad (22)$$

so that

$$\ln(10)\cdot(-A) = \ln(e)\cdot(-kz)$$
$$\ln(10) = 2.303, \ln(e) = 1$$

and

$$A = \frac{kz}{2.303} \qquad (23)$$

Notice now the relationship between A and the attenuation index K derived earlier:

$$k = \frac{4\pi}{\lambda_0} K \rightarrow \frac{kz}{2.303} = \frac{4\pi}{2.303\lambda_0} Kz = A \qquad (24)$$

So we see that the extinction coefficient k is really just the natural logarithm equivalent of the base-10 logarithm Beer's Law Absorbance. This operation is familiar to chemists, because it results in Absorbance calibration plots that are linear with respect to the volume concentration of the absorbing analyte[30]. Finally, remember that absorption may be expressed via the imaginary part of the complex dielectric function, in which case the relationship $\mathrm{Im}(\varepsilon) = 2nK$ is substituted into the above derivation.

2.4 Interaction Between Light And Matter

The relationships established above between the electromagnetic "constants" and the optical "constants" show how the properties of materials affect an incident light wave and vice versa. However, one more step must be included in the discussion to provide a more practical result, at least in terms of spectroscopic measurements: that is, relating changes in the optical properties of materials to the frequency or wavelength of an

---

[30] Thomas, M. J. K. *Ultraviolet and Visible Spectroscopy*, 2nd Edition, John Wiley & Sons, Chichester, 1996, p. 18.

incident light field. We have seen in the equations for n and K above that they contain a frequency term; however, those relationships still depend explicitly on the material parameters μ, σ, and ε. In order to derive the relationship between an incident light field and the optical properties of a material, we may proceed from the idea that all interaction processes between the two consist of the interaction of the electromagnetic wave with the fields generated by the moving electrons surrounding the nuclei of the material's atoms. Furthermore, this relationship is rendered more intuitive if we consider that the electron movements can be characterized as those of a harmonic oscillator: that is, a "ball on a spring". Such an oscillator may be bound, as in the case of a so-called "dielectric" material, in which the electrons are effectively bound to an atom with infinite mass relative to the electron. Or the oscillator may be un-bound, as in a perfect metal (i.e. materials with high conductivity, σ), where the valence electrons are completely free from the atoms of the material. The displacement $x(t)$ of the oscillator as a function of time may be found from

$$a\frac{\partial^2 x}{\partial t^2} + b\frac{\partial x}{dt} + cx = f(t) = e_0 E_\omega e^{i\omega t} \qquad (25)$$

where a is the mass of the oscillator (the electron), b is the damping force and c is force constant of the "spring". In this case, b represents losses in energy of the electron due to friction (which will be relatively small in the case of metals, and will depend on their Resistance at a particular frequency), or through the emission of radiation. The force constant c represents the stiffness or strength of the bond between the electron and the

atom it bound to, causing the electron to oscillate at some resonant frequency ω_0; of course, in the case of metals this term will be absent, at least in the optical and sub-optical frequency range. Finally, the applied force *f(t)* is in this case the incident light wave multiplied by the base electron charge e_0 to produce units of Force. Applying Maxwell's equations to this problem allows the complex refractive index of a material to be calculated as a function of the *polarizability* of the electrons.[31] The derivation of this relationship leads to the following expressions for how *n* and *K* change as a function of the incident light frequency:

$$\left(n^2 - K^2\right) = 1 + \frac{Ne^2}{me_0} \frac{\omega_0^2 - \omega^2}{\left(\omega_0^2 - \omega^2\right)^2 + \gamma^2\omega^2} \qquad (26)$$

$$2nK = \frac{Ne^2}{me_0} \frac{\gamma\omega}{\left(\omega_0^2 - \omega^2\right) + \gamma^2\omega^2} \qquad (27)$$

(Notice that n and K are unitless, and indeed all of the units in the terms on the right hand sides of the these equations cancel each other: the grouping of Ne^2/me_0 reduces to sec^{-2}, while the frequency group reduces to sec^2.)

Figures 2.4, 2.5, and 2.6 show how these two equations vary over an arbitrary spectral range of wavelengths (converted from frequencies in the equations above for convenience). The term λ_0 represents a resonance wavelength of the material: these wavelengths are determined by the selection rules of quantum mechanics that dictate

---

[31] Garbuny, M. *Optical Physics*, Academic Press Inc., New York and London, **1965**, p. 267.

what energy levels the electrons within a particular atom are allowed to occupy. The classical relationships described here are sufficient to provide a good conceptual foundation for the student, but they do not predict the position of anomalous dispersion bands in real atoms or molecules. However, most chemists are more familiar with the rules of quantum mechanics than with the physical interpretation of optical interactions, so I have chosen to concentrate on this classical description.

To continue, the λ_0 term is related via the harmonic oscillator problem to the force constant c of the bond between the electron and its atom. The term γ represents the damping constant associated with this resonance frequency. Note that in the optical and sub-optical wavelengths range most metals do not have any resonant wavelengths. The figures show the functions n and K at several values of γ ("hi", "medium", and "low") to illustrate that the wavelength interval of the energy transition gets broader and less intense with increased damping (though notice that the area under the curve for K stays the same). The γ term is inversely proportional to the lifetime of the particular transition, so that it becomes evident that short-lived excited states exhibit broader absorbance and/or emission regions than do longer-lived states. This is in agreement with the quantum-mechanical phenomenon of lifetime broadening, in which it becomes harder to specify the energy levels occupied by a system as the lifetimes of those levels become smaller.[32] Thus, when combined with the selection rules for quantum mechanics, we see

---

[32] Atkins, P. W. *Physical Chemistry*, 4th Edition, Oxford University Press, **1990**, p. 471.

how this picture of electrons behaving as harmonic oscillators experiencing an incident force field qualitatively accounts for the features of a typical (i.e. dielectric, for which $n >> K$) absorbance or emission spectrum. The case for metals, where K often exceeds n, is very different practically, but not conceptually or mathematically. All of the optics texts referenced in this chapter discuss the properties of metals in detail.

2.5 Polarization of Light

Recall that light travels as electromagnetic waves with the transverse vectors **E** and **H**. Furthermore, one of the consequences of the electron oscillator model of matter is that the electric field vector **E** assumes the primary role in the interaction of light with the electric fields generated by the moving cloud of electrons surrounding the atoms of a given substance (assuming a dielectric substance, in which μ and σ are near 0). This is why the amplitude term in the wave equation for a light beam is often written as the magnitude of the **E** vector. Also, notice that interaction between the **E** fields of the light and the electrons will only occur if they are oriented parallel to each other. Thus, it becomes necessary to derive some notation for representing the relative orientations of the light and the matter it impinges on: such notation is called the polarization of the light beam. In optical applications, the state of polarization usually refers to the orientation of the **E** vector for the reasons described above, and this orientation is referenced via the plane containing the incident and resultant beam interacting with a substance. Figure 2.7

shows the two extreme possibilities of orientation with respect to this optical plane: s- or *sanskrecht* (German for "perpendicular"), also called TE (Transverse Electric), in which the **E** vector is perpendicular to the optical plane (and parallel to the incident plane); and p- or parallel, also called TM (Tranverse Magnetic), in which the **E** vector is parallel to the incident plane (and perpendicular to the incident plane). Note that these definitions imply that the path traveled by the light does indeed form a plane; that is, it is incident at some oblique angle on to the surface of interaction with the material. At normal incidence to a material no such plane exists, so that this notation fails to hold – though the light may still be polarized with the **E** vector directed "vertically" or "horizontally" relative to the direction of travel of the beam. Such polarization results from transmitting light through optical elements like anisotropic (i.e. containing two axes of molecular or atomic orientation) crystals or quarter-wave plates that produce a beam with individual photons having their **E** vectors all oriented in the same direction. Again, such a beam must be incident at some non-zero angle to a material for the s- and p- definitions above to apply.

2.6 Reflection and Refraction at an Interface

Having discussed the wave nature of light and the coefficients that describe the interaction of light with matter, we can now apply these properties to examining what happens when light strikes an interface.

Figure 2.7 shows such an interface, which can be thought of as a boundary between two media with the optical parameters n_1 and n_2 respectively. Of course, these can be replaced by the complex refractive index if the possible existence of light absorption should be taken into account – so the second medium is broken down into the complex refractive index $n + iK$. The light energy impinging on this interface is propagated according to the wave-vector $\boldsymbol{k}$ described above, which is proportional to Poynting's vector (i.e. **ExH**). Within the boundary plane, the phases of the parallel components of the incident, transmitted, and reflection wave-vectors must be equal *and* continuous, so that:

$$\vec{k}_i \cdot \vec{r} = \vec{k}_r \cdot \vec{r} = \vec{k}_t \cdot \vec{r}_t \qquad (28)$$

where $\vec{r}$ is the unit vector parallel to the interface. Their magnitudes are equal to:

$$k_i r \sin\theta_i = k_r r \sin\theta_r = k_t r \sin\theta_t \qquad (29)$$

Now we can use the fact that:

$$k_i = k_r = n_i \frac{2\pi}{\lambda_0}, k_t = n_t \frac{2\pi}{\lambda_0} \qquad (30)$$

where λ_0 is the light wavelength in air. Since $n_i = n_r$, the incident and reflected waves have equal but opposite angles of propagation with respect to the interface (i.e. the law of reflection), while the incident and transmitted propagation angles follow Snell's Law (since the $\frac{2\pi}{\lambda}$ terms cancel out):

$$n_i \sin\theta_i = n_r \sin\theta_r \qquad (31)$$

The parallel components of the electric vectors E, however, follow a cosine rule for the TM polarization:

$$-E_i \cos\theta_i + E_r \cos\theta_r = -E_t \cos\theta_t \qquad (32)$$

Figure 2.8 shows the trigonometry that establishes these relationships for the ***k*** and **E** vectors (only the incident vectors are shown, but the transmitted and reflected ones are similar). Note that for the TE polarization, since the **E** vectors are all parallel to the interface, they are related simply by:

$$E_i + E_r = E_t \qquad (33)$$

The so-called Fresnel coefficients are derived, which are expressions of E_r/E_i and E_t/E_i, when this treatment is carried out fully for the relationships between the electric field amplitudes for the TE and TM polarizations, relying on the identity:

$$\frac{n_2}{n1}\cos\theta_t = \sqrt{\left(\frac{n_2}{n_1}\right)^2 - \sin^2\theta_i} \qquad (34)$$

to eliminate the transmission angle θ_t. Since GLRS is a reflection-based technique, however, only the Fresnel reflection coefficients will be presented here.[33] Fresnel coefficients for reflection of light at incident angle θ_i from a material with relative

---

[33] many optical texts have complete derivations of these relationships; two good ones are Born and Wolf, *Principles of Optics*, and Pedrotti and Pedrotti, *Introduction to Optics*.

complex refractive index coefficients η_2/η_1, which according to the rules for division of complex numbers,[34] gives $n = n_2/n_1$ and $K=K_2$ if there is no imaginary component to medium 1:

$$TE = \frac{\cos\theta - \sqrt{\left(n^2 - K^2 - \sin^2\theta\right) + i(2nK)}}{\cos\theta + \sqrt{\left(n^2 - K^2 - \sin^2\theta\right) + i(2nK)}} \qquad (35)$$

$$TM = \frac{\left[n^2 - K^2 + i(2nK)\right]\cos\theta - \sqrt{\left(n^2 - K^2 - \sin^2\theta\right) + i(2nK)}}{\left[n^2 - K^2 + i(2nK)\right]\cos\theta + \sqrt{\left(n^2 - K^2 - \sin^2\theta\right) + i(2nK)}} \qquad (36)$$

Note that when the n and K variables are replaced by the dielectric function

$$\varepsilon(\omega) = \eta(\omega)^2 = \left(n(\omega) + iK(\omega)\right)^2 \qquad (37)$$

the Fresnel coefficients become

$$TE = \frac{\cos\theta - \sqrt{\varepsilon - \sin^2\theta}}{\cos\theta + \sqrt{\varepsilon - \sin^2\theta}} \qquad (38)$$

$$TM = \frac{\varepsilon\cos\theta - \sqrt{\varepsilon - \sin^2\theta}}{\varepsilon\cos\theta + \sqrt{\varepsilon - \sin^2\theta}} \qquad (39)$$

---

[34] Jeffreys, H.; Jeffreys, B. S. *Methods of Mathematical Physics*, 2nd Ed., Cambridge University Press, 1950, pp. 333-335.

Figures 2.9 and 2.10 demonstrate external and internal Reflectivity curves, respectively, in which the light goes from either a "hi-lo" or a "lo-hi" refractive index situation. These Reflectivity curves are equal to the square of the Fresnel coefficients, since the light intensity is actually measured, and not the field amplitude. Note that the Reflectivity will approach 100% at certain angles in the case of light incident from the high refractive index side of an interface. This happens when the critical point, in this case a critical *angle*, θ_c, is exceeded according to:

$$\theta_c = \sin^{-1}\left(\frac{n_2}{n_1}\right) \qquad (40)$$

This is termed Total Internal Reflection (TIR), and (though it may be obvious) it occurs only when the light is incident on the interface from the high refractive index side, since $\sin^{-1}$ must be less than 1.

However, as stated above, Maxwell's equation require the field amplitudes of the light be continuous across an interface: this means that even if no propagation vector exists on the transmitted side of the interface, the electric field will still penetrate across the interface to some extent. This may be intuitively thought of as a consequence of the finite cross-section of the plane wave. Figure 2.11 shows this situation.

Such a wave is called an evanescent wave, because it can be seen that, when averaged over time, there is no flow of energy into the medium beyond the interface. This is because the Poynting vector $\boldsymbol{S \approx E \times H}$ *(~k)*, which quantifies the propagation of energy in the electromagnetic wave, is oriented along the interface. However, if the

sample absorbs some of that energy, then it will be converted into heat or some other form (perhaps even re-emitted as light) and a net loss will be seen. Furthermore, since no interface is infinitely long, there will be some light "leakage" out of the end of the boundary regardless of absorption losses in the interfacial media. In either of these cases the Reflectivity will be seen to dip below 100%. Figures 2.12 and 2.13 show how dramatically the Reflectivity changes in this TIR situation relative to a similar absorption loss in an external reflection situation. Note for the external reflection situation in figure 2.12 that the values of K are more than an order of magnitude greater than for the internal reflection case in figure 2.13, but the response for the internal reflection is still much greater – as shown in figures 2.14 and 2.15. This indicates that monitoring of this "critical point" in the Reflectivity curve should prove to be a useful way of determining both components of the complex refractive index of a sample. This is exactly what GLRS does – except that it uses a diffraction grating to allow the Reflectivity to be viewed versus wavelength, instead of as a function of incident angle.

In general, the sensitivity of this critical point can be expressed in two ways: penetration depth (d_p) and effective thickness (d_e). Penetration depth is a measure of the distance beyond the interface at which the evanescent wave's electric field falls to e^{-1} of its incident value. Note from the equations below and Figure 2.16 that this increases dramatically as the critical condition is more exactly matched, and theoretically can become infinite in the absence of absorption losses:

$$E = E_0 e^{-z/d_p} \qquad (41)$$

$$d_p = \frac{\lambda}{2\pi\left(\sin^2\theta - n_{21}^2\right)^{1/2}} \qquad (42)$$

Here it is seen that in the limit of infinite penetration depth the electric field will remain virtually constant for infinite distance z normal to the interface. Figure 2.16 also illustrates the importance of matching the critical condition as closely as possible for maximum sensitivity: the penetration depth decreases by an order of magnitude only a few degrees above the critical angle. However, this parameter does not fully express the strength of the interaction between the evanescent wave and the sample medium. A second criterion is needed to establish the effectiveness of the coupling between the evanescent wave and the sample. This is called the effective thickness, d_e: it represents the thickness or pathlength of sample needed in a transmission-based absorbance measurement to yield an Absorbance equal to a reflection measurement performed on the same sample:

$$d_{eTM} = \lambda \frac{n_{21}\cos\theta\left(2\sin^2\theta - n_{21}^2\right)}{\pi\left(1 - n_{21}^2\right)\left[\left(1 + n_{21}^2\right)\sin^2\theta - n_{21}^2\right]\left(\sin^2\theta - n_{21}^2\right)^{1/2}} \qquad (43)$$

$$d_{eTE} = \lambda \frac{n_{21}\cos\theta}{\pi\left(1 - n_{21}^2\right)\left(\sin^2\theta - n_{21}^2\right)^{1/2}} \qquad (44)$$

Figure 2.17 shows some effective thicknesses for different hypothetical interfaces with TM light. As expected, the effective thickness is always greater for TM polarization (see

figure 2.18), since the electric vector of the resulting evanescent wave will project normal to the interface, and it is this vector that interacts most strongly with the bound electrons of the sample medium. Figure 2.17 also shows that the effective thickness increases as the refractive index contrast of the interface gets closer to 1:1. Finally, note that the effective thickness can become very great as the critical point condition is more closely matched, and that it falls off rapidly as the coupling condition is less well matched. Therefore, a technique such as GLRS, which ensures that the exact critical point coupling condition is always matched over the course of a measurement, will exhibit optimum sensitivity to the optical properties of the sample.

2.7 Grating Light Reflection Spectroscopy

The rigorous theory that defines the basic spectral response of GLRS to sample optical properties has been discussed in detail in several different publications,[35] so I will not replicate it here. However, I will provide a qualitative description of the most

---

[35] In order of significance, these are:

1) Anderson, B. B.; Brodsky, A. M.; Burgess, L. W. *Physical Review E*, **1996**, vol. 54, no. 1, pp. 912-923.

2) Anderson, B. B.; Brodsky, A. M.; Burgess, L. W. *Analytical Chemistry*, **1996**, vol. 68, no. 7, pp. 1081-1088.

3) Brodsky, A. M.; Burgess, L. W.; Smith, S. A. *Applied Spectroscopy*, **1998**, vol. 52, no. 9, pp. 332A-343A.

significance results of these theoretical derivations, so that someone attempting to learn about GLRS may form a more intuitive picture of the theoretical aspects of the technique. In addition, despite the lack of a fully rigorous treatment, the results presented below do include the two relationships (equations 47 and 58) that are required to quantitate sample properties from GLRS reflection spectra. Therefore, someone who desires to implement the GLRS technique should have all of the information necessary to construct an apparatus, conduct experiments, and extract relevant information from the data collected.

Usually, when light encounters a homogenous boundary between two media with refractive indeces n_1 and n_2, it behaves according to Snell's Law:

$$n_1 \sin\theta_i = n_2 \sin\theta_t \left(= n_1 \sin\theta_r\right) \qquad (45)$$

where the term in parentheses is added to show that, since the incident and reflected beams travel within the same medium, their angles of propagation relative to the interface are equal.

However, if a regularly periodic disturbance is placed across that boundary, in the form of a permittivity (i.e. refractive index) modulation, an addition term must be inserted into Snell's Law to account for the fact that some of the incident wave front will experience a different boundary condition:

$$n_1 \sin\theta_i + m\frac{\lambda}{\Lambda} = n_2 \sin\theta_t \qquad (46)$$

where m can be a positive or negative integer (these integers are called *diffraction orders*), Λ is the distance between individual refractive index "barriers", and λ is the

wavelength of light in the incident wave front. First of all, note that in the limit of infinitely small distances between these barriers, such as between the individual atoms of an organized crystalline solid (most liquids approximate a regularly organized crystal-like structure as well), where Λ is much less than the wavelength, no transmission across the interface is possible, except in the case of $m = 0$ (because otherwise the sine term is greater than 1 or less than 0). Likewise, if Λ becomes extremely large relative to the wavelength, such as the distance between individual boards of a picket fence, again only the $m = 0$ case exists, because the m-containing term is virtually 0 for all other values of m anyway. Thus, one sees that this "regularly periodic permittivity boundary", commonly known as a diffraction grating, does not really give rise to a new phenomenon, but instead represents an intermediate condition within the overall spectrum of refractive index differences at a boundary between two media.

This condition arises when the interface breaks up the incident wave front into discrete units on a distance comparable to the wavelength of that wave front, so that they may re-combine at common phase boundaries formed between the individual wave fronts as they radiate outward from the boundary. This can be intuitively expressed by drawing concentric half-circles (i.e. spherical waves) originating from each transparent component of the interface, with radii increasing by λ for each circle, and then drawing straight lines along these "in-phase" fronts to join the circles of different transmitting sections of the interface. Figure 2.19 shows only 3 such combinations, though in general as many of these "diffraction orders" will exist as are allowed by equation (46) above. In addition,

note that reflected orders exist as well, though not with the same spatial orientation as the transmitted orders since the refractive index of the medium these travel through will in general be different from that of the transmission medium. As an example of this, Figure 2.20 shows all of the possible diffraction orders that occur in a typical GLRS experiment.

As can be seen from this figure, Grating Light Reflection Spectroscopy uses this property of diffraction gratings to generate, at a particular wavelength, a transmitted diffraction order that is oriented along the surface of the grating / sample interface. This is analogous to creating a transition from external to internal reflection at this wavelength. In addition to the order undergoing the critical point transition and the zeroth order reflection that is collected, however, there are four additional orders supported by this grating at the critical wavelength. This "wasted" energy results in a modest signal-to-noise decrease.

The general scheme of GLRS is presented in figure 2.21. When the optical plane is oriented perpendicular to the grating lines, the critical points or thresholds described in the Introduction are defined by

$$\delta \equiv \mathrm{Re}[\varepsilon_2(\omega) - (\sin\theta_i + \frac{m_{cr}\lambda}{\Lambda})^2] = 0 \qquad (47)$$

where Λ is the grating spacing, $\varepsilon_2(\omega)$ is the dielectric permittivity of the studied sample, θ_i is the incident angle on the grating/sample interface, m_{cr} is the transmitted diffraction order containing the critical wavelength, and λ is the critical wavelength. This equation is simply a convenient way of expressing the condition at which the wave-vector transmitted by the grating transitions from a propagating harmonic wave in the sample to an evanescent wave along the grating / sample interface. Therefore, we see that δ is the

normal component of this wave-vector, since it equals zero at the critical point, and becomes negative (i.e. pointing into the grating substrate) for higher wavelengths. Figures 2.22 and 2.23 illustrate the values of δ within m_{cr} that span the critical condition for the two gratings (Λ's) used in the GLRS experiments discussed in this work: one has a period of ~500 nanometers, the other has a period of ~830 nanometers. One of the significant features of these figures is the increased rate of change of δ for the larger grating period: this means that a coarser grating will provide more sensitivity to refractive index changes.

Notice that equation (47) may be simplified by the use of Snell's Law. This is because, even though we now have a three layer interface, where the grating substrate has interposed itself between the grating / sample interface and the incident beam, this can be reduced to a two-layer interface by considering that:

$$n_0 \sin\theta_0 = n_1 \sin\theta_t \qquad (48)$$

where the 0 terms refer to air (the incident beam medium) and the 1 terms refer to the grating substrate. Since the refractive index of air is 1, and the incident angle at the air/substrate interface is more convenient to measure than the incident angle of the substrate/grating interface, we may simply use $n_0 \sin\theta_0 = \sin\theta_i$ in the equation for δ above.

A significant feature of these figures is that, for refractive index sensing purposes, it is favorable to use a grating with as large a period as possible, since this results in the greatest refractive index dispersion or $\partial\lambda/\partial n$ (one may think of this as the sensitivity of the measurement with respect to refractive index). Note, however, that this is opposite to the situation with regard to the use of gratings in spectrometers, in which greater *wavelength* dispersion (and thus greater spectroscopic resolution) is achieved with gratings of smaller periods. This non-intuitive situation becomes clearer when one considers that GLRS is in effect measuring Snell's Law for the particular case where θ_t is equal to 90°, and that this is dependent on n_2, the refractive index of the sample. Thus:

$$n_i \sin\theta_i = n_t \sin\theta_t, \sin\theta_t = 1 \qquad (49)$$

Where the term $n_i \sin\theta_i$, instead of defining the wave-vector incident on a planar homogenous interface, now defines the wave-vector created by the grating that is, in effect, "incident" on the sample:

$$n_i \sin\theta_i = \sin\theta + \left[m\frac{\lambda}{\Lambda} \right] = n_t \qquad (50)$$

Re-arranging the right-hand equation in order to express λ as a function of n:

$$\lambda = \left(\frac{\Lambda}{m} \right) n_t - \sin\theta \qquad (51)$$

Now that the equation is in the linear form of y = mx +b, we can take the derivative of λ with respect to n to determine the sensitivity of the wavelength-dependent refractive index response (i.e. the slope of the line that expresses the relationship between λ and n):

$$\frac{\partial\lambda}{\partial n_t} = \frac{\Lambda}{m} \qquad (52)$$

So it is seen that refractive index sensitivity is directly proportional to the spacing between grating lines, and that it is preferable to create the critical condition within the 1st diffraction order.

Continuing with the derivation of the GLRS response, it is helpful to notice the similarities of this derivation to that of the Fresnel reflection coefficients in the previous section. We saw in previous section on Fresnel's coefficients that we may re-phrase the parallel components of the interfacial wave-vectors $\vec{k}_x$ in terms of refractive indeces as:

$$\vec{k}_x = n_x \sin\theta_x \qquad (53)$$

This means that the transmitted wave-vector at $\delta = 0$ is merely n_t, while the incident wave-vector is $\left(\sin\theta_i + m\frac{\lambda}{\Lambda} \right)$. Therefore, we see that the critical condition (equation x) is simply the case for which the *squares* of the parallel components of the incident and transmitted wave-vectors are equal to each other. At this point they cancel each other out,

and so all of the light energy must go into the reflected wave-vector: in other words, Total Internal Reflection occurs.

As stated above, Equation (47) has been formulated in terms of the squares of the wave-vectors. This means that since the Poynting vector, or intensity, of the reflected light is proportional to the reflected wave-vector, then it must also be proportional to the square-root of δ. That is:

$$I \approx \sqrt{\delta} \qquad (54)$$

This is mathematically similar to the relationship between the dielectric constant ε and the refractive index n:

$$n^2 = \varepsilon \Leftrightarrow \sqrt{\varepsilon} = n \qquad (55)$$

Since we know that the real and imaginary parts of these quantities can be calculated by:

$$n = \sqrt{\frac{\sqrt{\varepsilon_R^2 + \varepsilon_I^2} + \varepsilon_R}{2}} \qquad (56)$$

$$K = \sqrt{\frac{\sqrt{\varepsilon_R^2 + \varepsilon_I^2} - \varepsilon_R}{2}} \qquad (57)$$

then the real and imaginary (mathematically speaking) parts of the intensity and the critical wave-vector must be expressible in this same way. Furthermore, having defined δ as the real part of the transmitted wave-vector, which is dependent on the refractive index of the sample, then the imaginary part of this wave-vector must depend on the imaginary refractive index of the sample. Therefore we can express the reflection spectrum ($R \approx I$) in the region where δ transitions from a traveling wave to an evanescent wave as the sum of a real and imaginary intensity contribution:

$$R = C_1 + C_2\sqrt{\frac{\sqrt{\delta^2 + \mathrm{Im}(\varepsilon_2)^2} - \delta}{2}} + C_3\sqrt{\frac{\sqrt{\delta^2 + \mathrm{Im}(\varepsilon_2)^2} + \delta}{2}} \qquad (58)$$

which can be broken up into two spectral regions corresponding to externally and internally reflected wavelengths (i.e. those on the transmitted side and those on the evanescent side of the critical wavelength at $\delta = 0$):

$$R = C_1 + C_2\sqrt{\frac{\sqrt{\delta^2 + \mathrm{Im}(\varepsilon_2)^2} - \delta}{2}} \quad \text{for } \delta \le 0 \qquad (59)$$

$$R = C_1 + C_3\sqrt{\frac{\sqrt{\delta^2 + \mathrm{Im}(\varepsilon_2)^2} + \delta}{2}} \quad \text{for } \delta > 0 \qquad (60)$$

The term under the square root in the equations above is proportional to the normal component of the Poynting vector of the critical beam. The three constants C_1, C_2, and C_3 are included to account for all of the contributions of the dielectric properties of the materials making up the interface, as well as the state of polarization of the incident beam. These properties have been subsumed under constants in order to make the equation for R as general as possible, so that it may be fit to actual data to extract sample properties without having to know the exact consequences of the interfacial dielectric properties on a particular GLRS implementation. Notice that at $\delta \sim 0$ the characteristics of the critical beam become very sensitive to the values of $\mathrm{Im}\varepsilon_{eff}$ (which includes the effects of coherence loss due to scattering by non-uniformities) even when $\mathrm{Im}\varepsilon_{eff} << \mathrm{Re}\varepsilon_{eff}$. This is especially true for wavelengths at which $\delta \le 0$, since in this region the positive and negative values of δ under the square root term compensate for each other. Again, this is exactly analogous to the situation of Total Internal Reflection (TIR) discussed above for the Fresnel coefficients with respect to absorbance ($\mathrm{Im}(\varepsilon)$) sensitivity.

Due to the law of conservation of energy, the total amount of energy incident on the interface must equal the total energy going out of the interface; therefore, the change of energy flow in the critical order becomes redistributed into all the other diffracted orders originated at the grating. Furthermore, since the critical order contains evanescent waves, and these waves do not transport energy away from the interface (in the absence of absorption by any of the media that compose the interface), it is expected that the behavior of this particular order will dominate the intensity contributions to the other orders. So if we choose to monitor the zeroth order reflection, the square root term in the equations above will form the most prominent feature of this spectrum. As stated above, the three constant terms depend upon the dielectric properties of the materials making up the interface (the grating, its substrate, and the sample) and also the polarization state of the incident light beam. The first constant is merely the overall intensity of the reflection, and so usually drops out upon intensity normalization of the data. The two other constants will assume either positive or negative values depending on the polarization state of the incident light, and their magnitudes will depend on the magnitude and sign of the refractive index difference between the grating material and the substrate, and between the substrate and the sample. Figure 2.24 shows the spectral forms of the four possible combinations of these two constants.[36] These show the overall shape of the

---

[36] for a more detailed derivation of these equations, see Anderson, B. B.; Brodsky, A. M.; Burgess, L. W. *Physical Review E*, **1996**, vol. 54, no. 1, pp. 912-923.

spectra due to the signs of the constants; the relative magnitudes of the two halves of the spectra will change according to the magnitudes of the two constants. Usually it is most efficient to determine these constants by simply taking a relative reflection coefficient of the zeroth order spectrum: R_{samp}/R_{ref}, where R_{ref} is the zeroth order reflection spectrum of the interface with no critical wavelength present (e.g. with air in contact with the grating / substrate surface). Then the constants can be determined by fitting this relative coefficient to a theoretically ideal form. For all of the work presented in this thesis, TM polarized light was used, so spectra of the form ($-C_2$-C_3) are expected. However, due to the particular dielectric properties of the fused silica/chrome/aqueous interface, the lobe on the evanescent side of the critical point is "weighted" less than the transmitted side: figure 2.25 illustrates this effect for different "weights" of C_2.

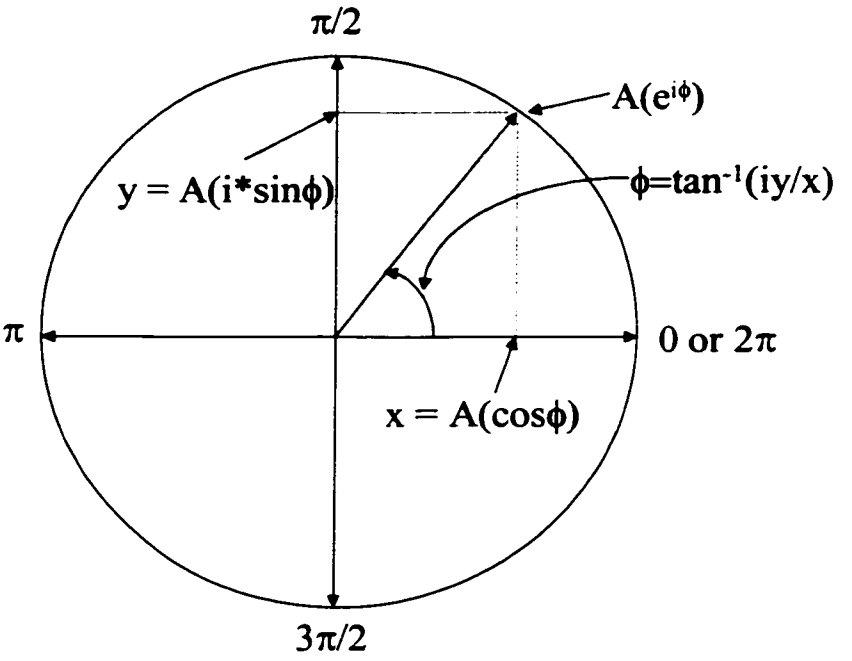

Figure 2.1 Argand Diagram for the graphical depiction of sine waves in the complex plane as vectors of length A that are rotated ϕ degrees relative to the real or x-axis.

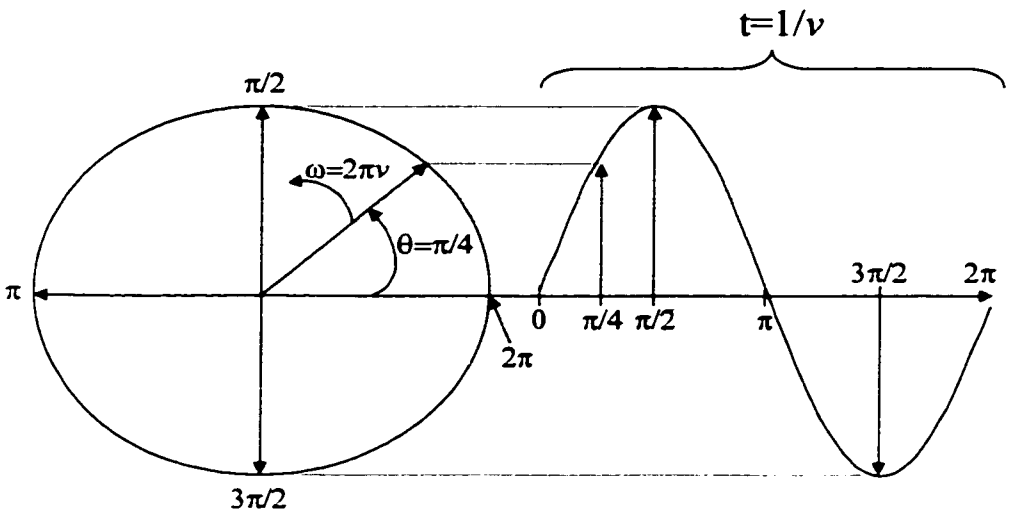

Figure 2.2 Relation of the components of the complex vector notation relate to their counterparts in the sinusoidal notation for a plane wave.

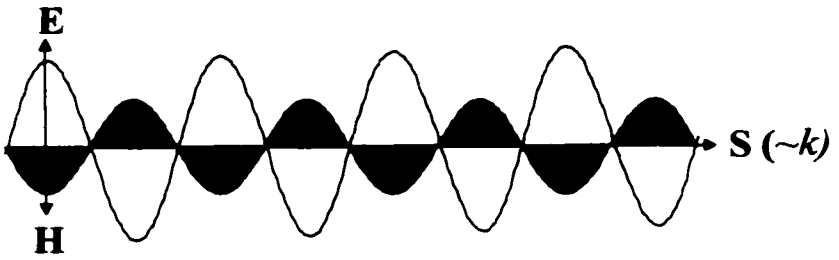

Figure 2.3 Electromagnetic wave propogating with a direction and wavelength given by ***k*** and with an energy defined through Poynting's vector $\mathbf{S} \approx \mathbf{E} \times \mathbf{H}$.

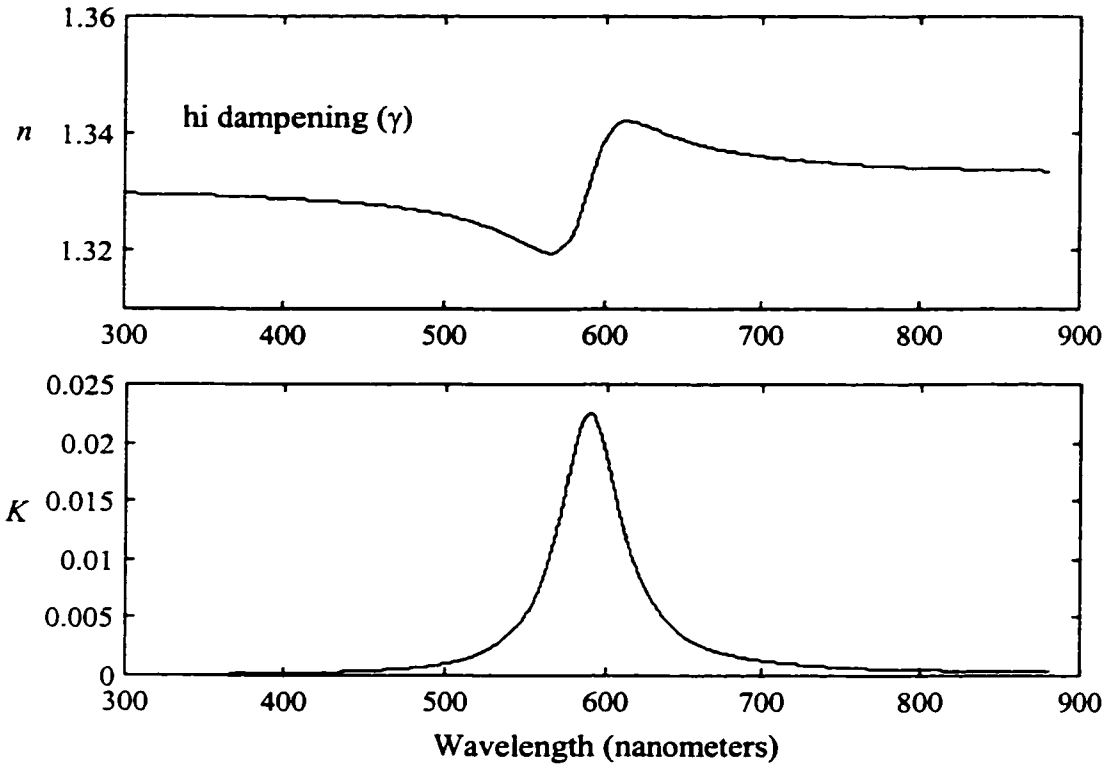

Figure 2.4 Anomalous dispersion caused by the presence of a "strong" absorption band.

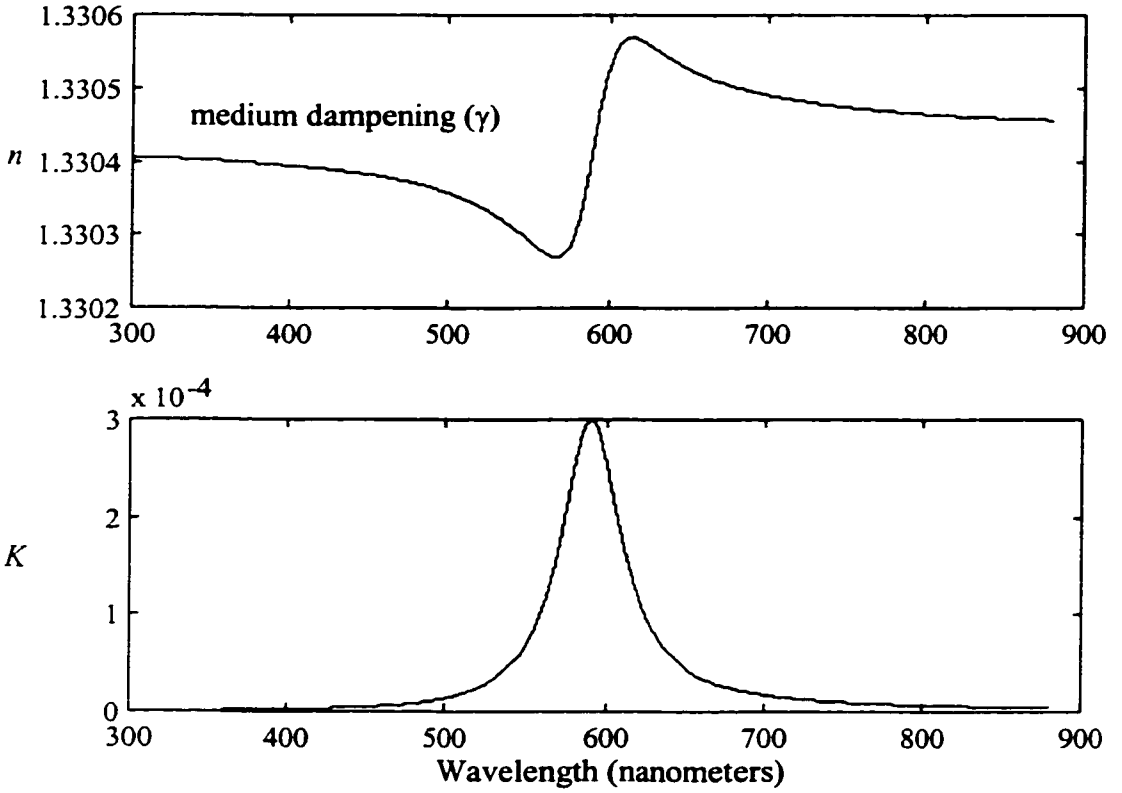

Figure 2.5 Anomalous dispersion caused by the presence of a "medium" absorption band.

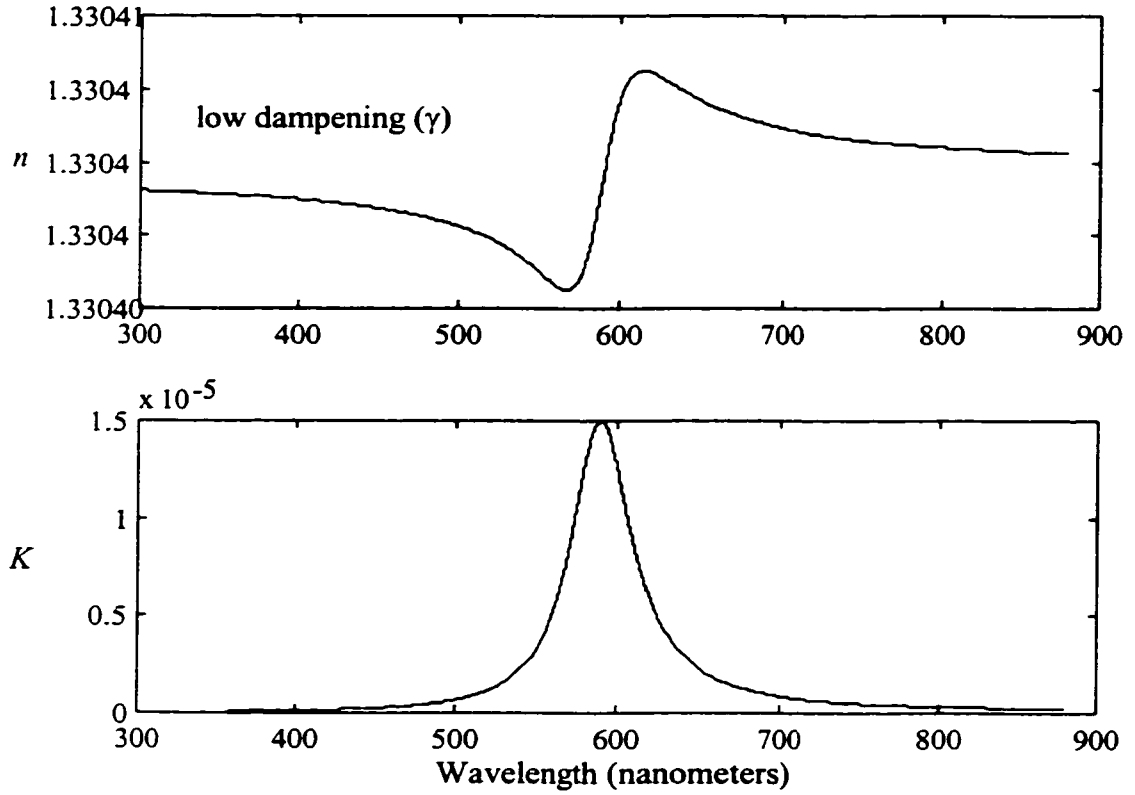

Figure 2.6 Anamolous dispersion caused by the presence of a "weak" absorption band.

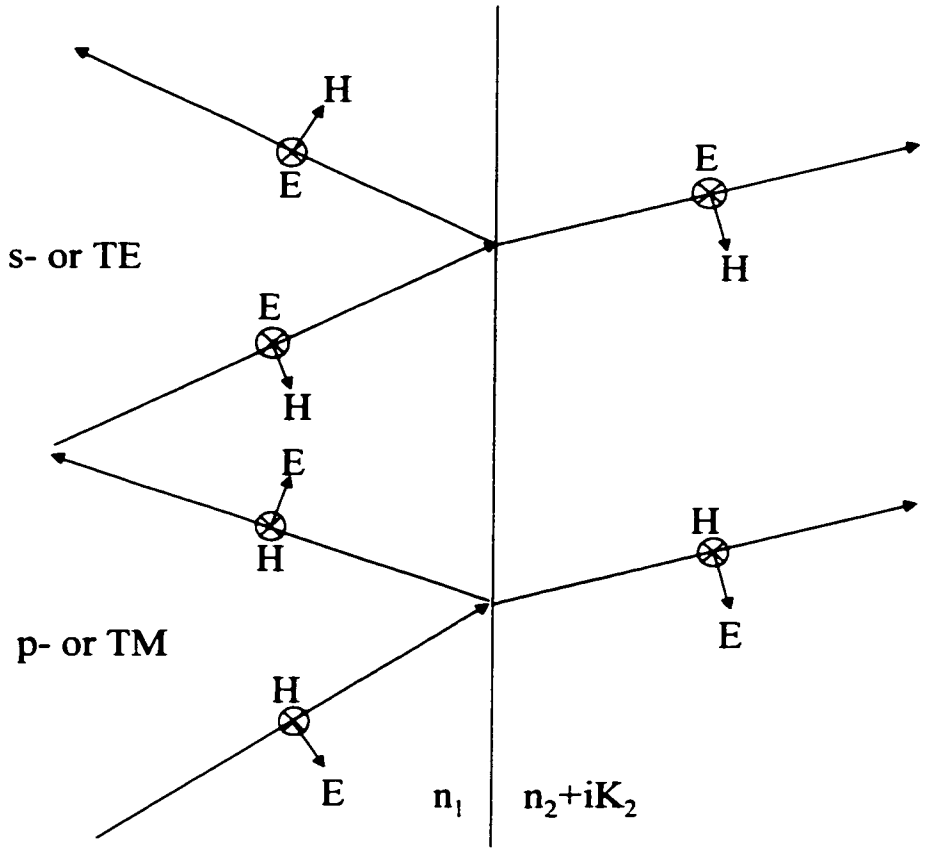

Figure 2.7 Illustration of TE and TM light polarization with respect to a reflection interface.

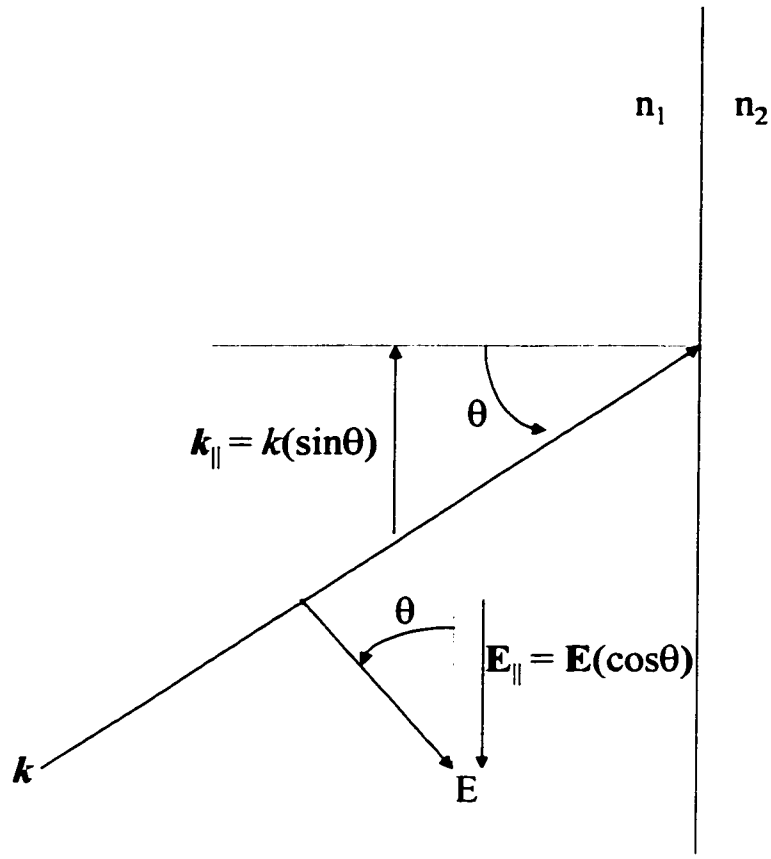

Figure 2.8 Trigonometric relationships for the ***k*** and **E** vectors of TM light incident on a reflection interface.

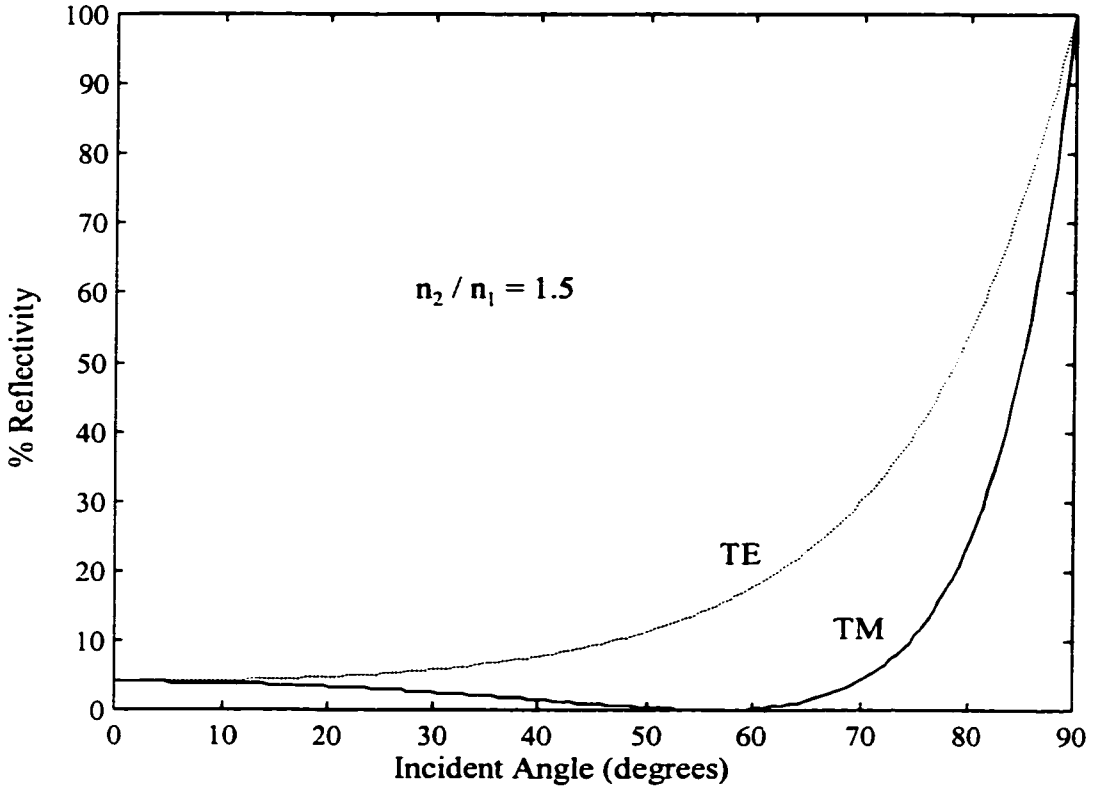

Figure 2.9 Typical Reflectivity curve for the case of external reflection at an interface.

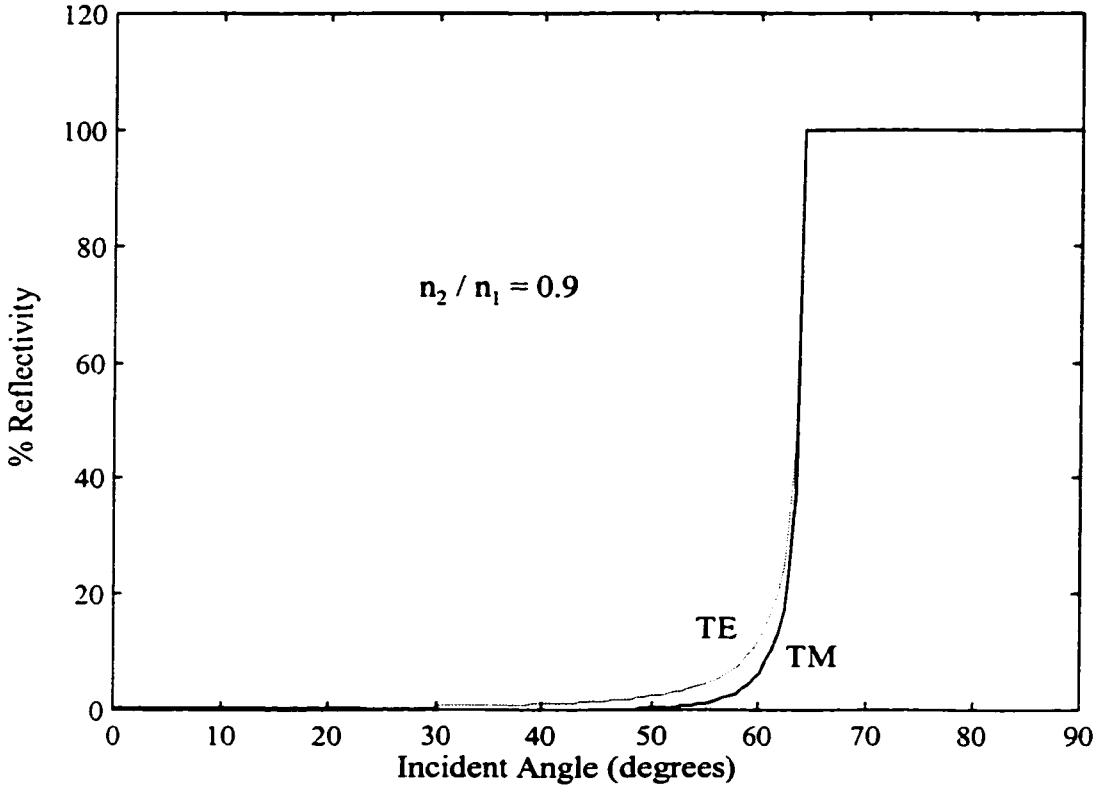

Figure 2.10 Typical Reflectivity curve for the case of internal reflection at an interface.

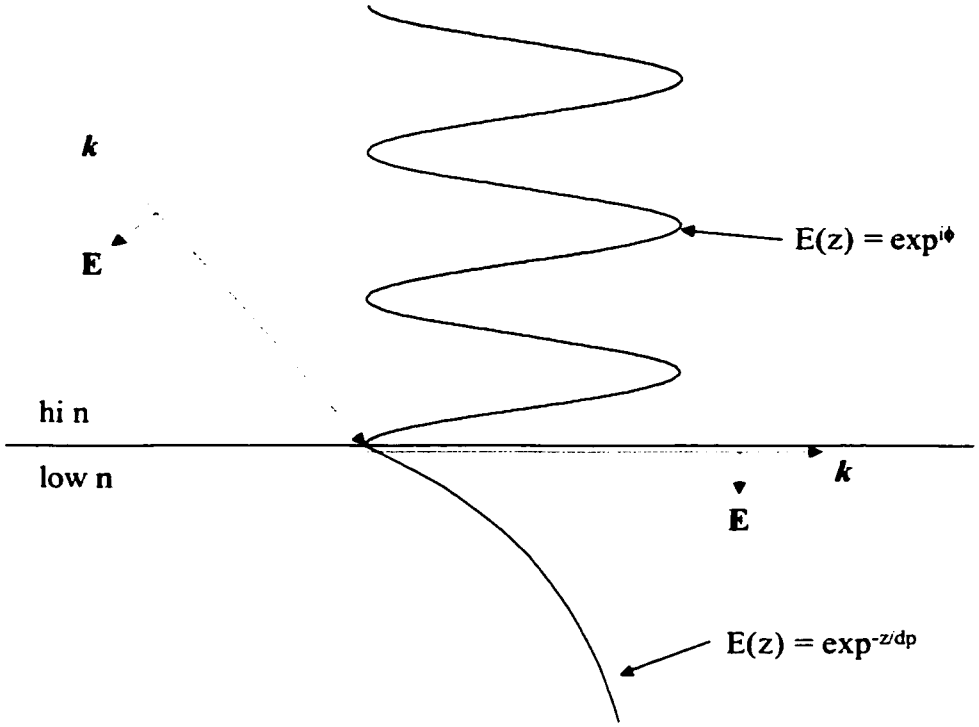

Figure 2.11 Characteristics of an evanescent wave at the critical angle.

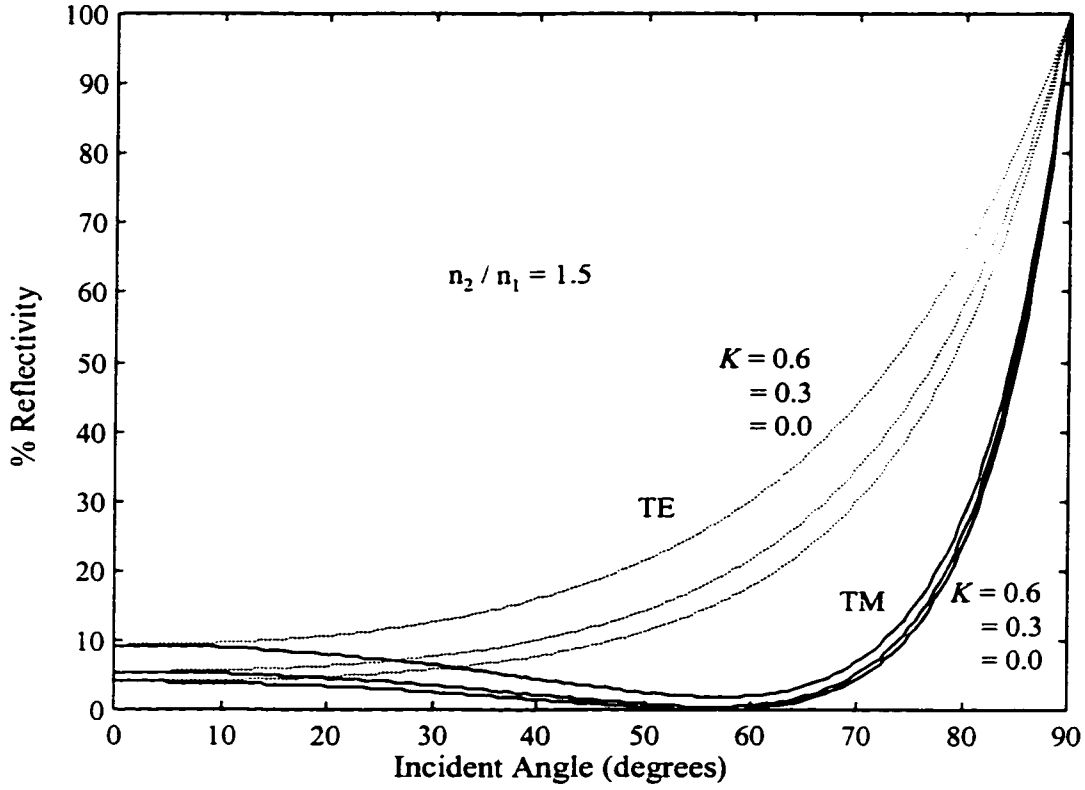

Figure 2.12 Changes of Reflectivity for external reflection as a function of increasing "sample" absorption.

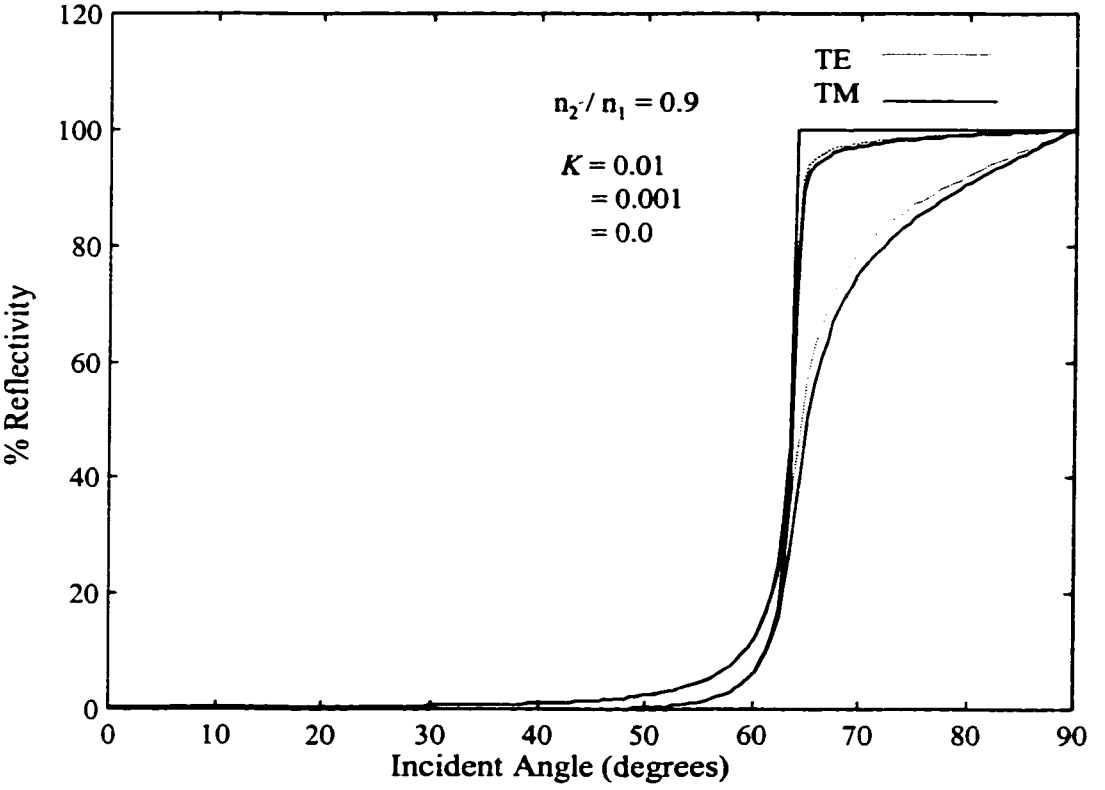

Figure 2.13 Changes of Reflectivity for internal reflection as a function of increasing "sample" absorption.

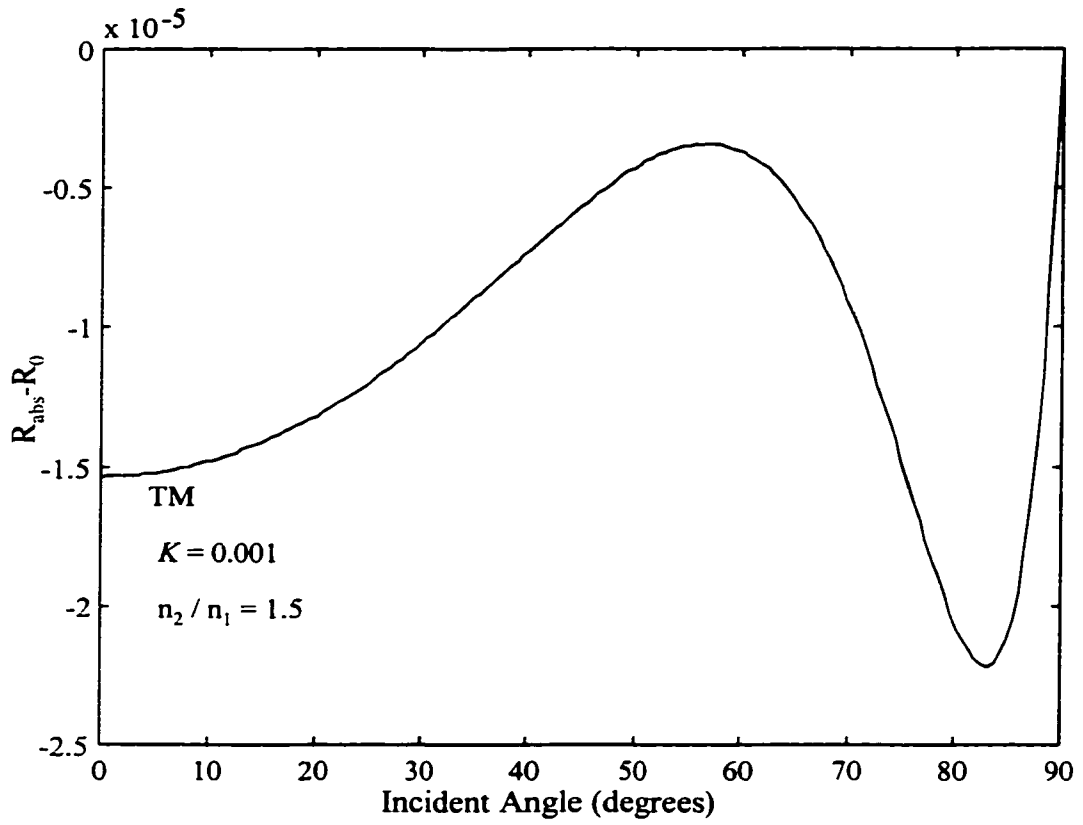

Figure 2.14 Reflectivity difference for external reflection between an absorbing "sample" and a non-absorbing one.

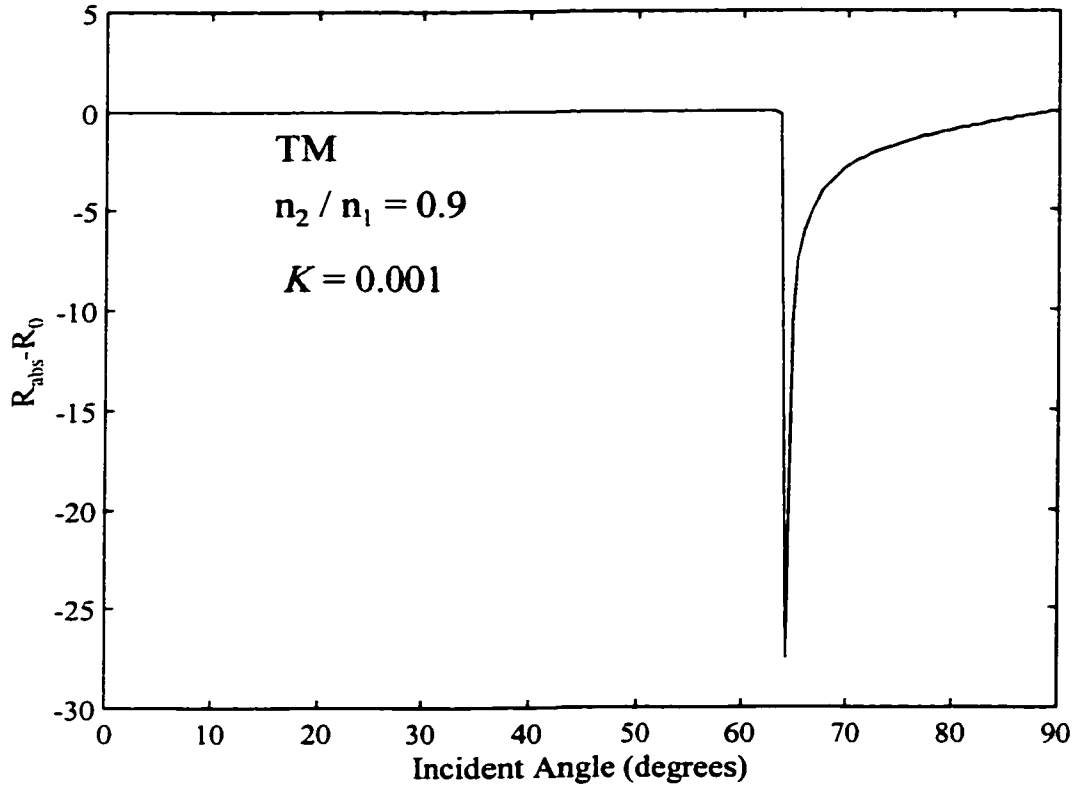

Figure 2.15 Reflectivity difference of internal reflection between an absorbing "sample" and a non-absorbing one.

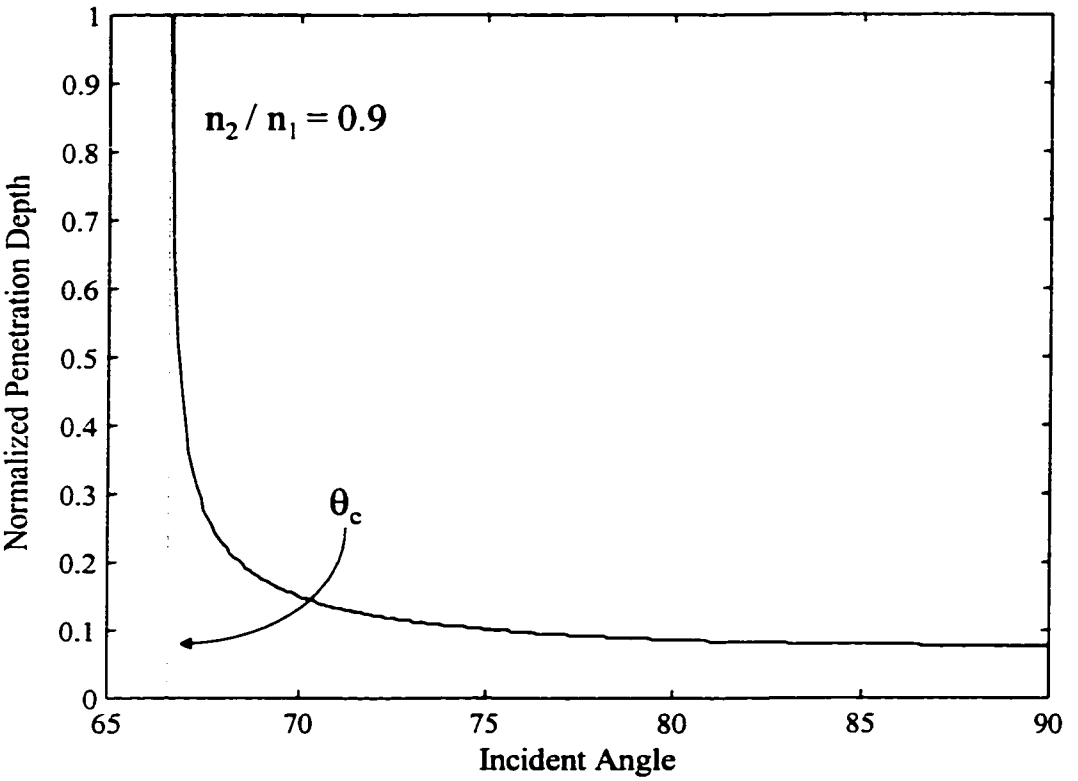

Figure 2.16 Decrease in penetration depth of an evanescent wave as a function of deviation from the critical angle.

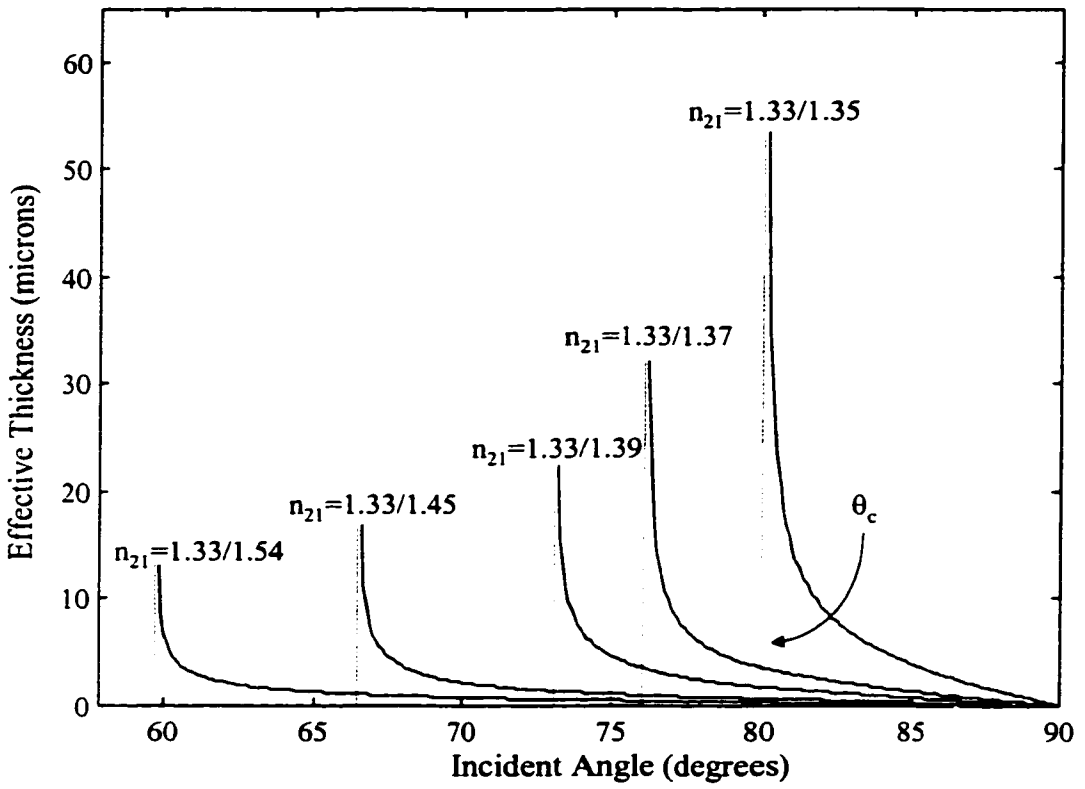

Figure 2.17 Change in effective thickness as a function of index matching of the reflection interface.

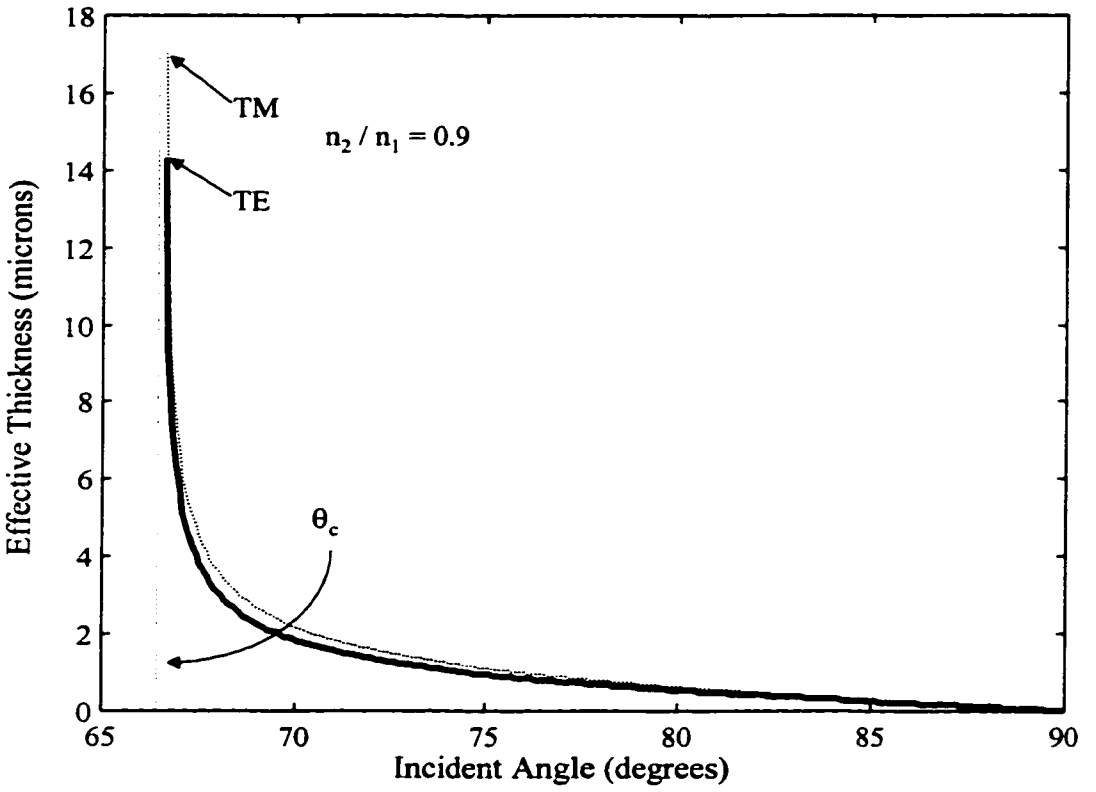

Figure 2.18 Illustration of the greater penetration depth for a TM-polarized evanescent wave relative to a TE-polarized one.

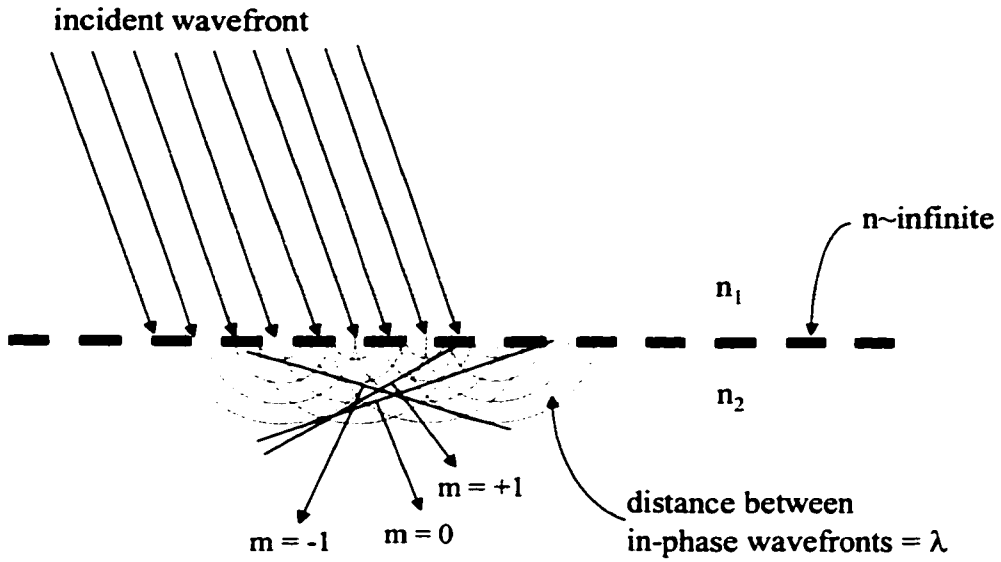

Figure 2.19 Generation of diffraction orders at a reflection interface due to the insertion of a regular permittivity modulation.

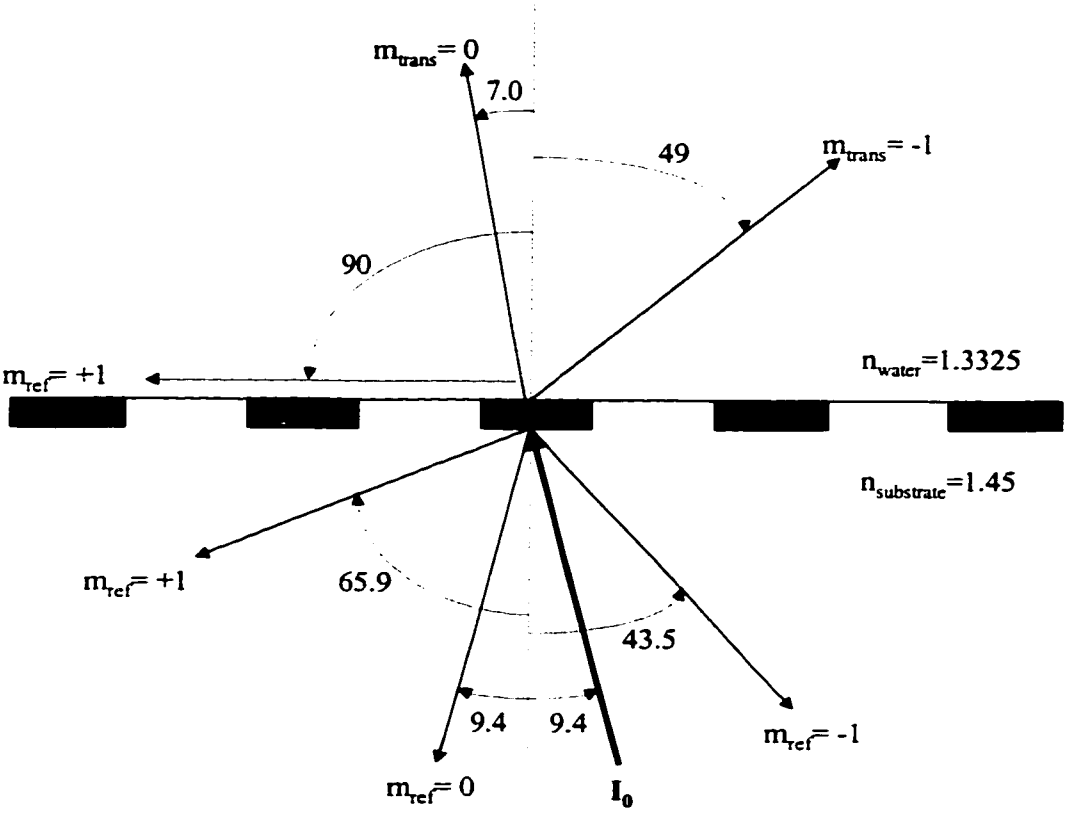

Figure 2.20 The spatial orientation of the critical wavelength in all diffracted orders existing for a 503.6 nanometer period grating when the +1 transmitted order undergoes the critical condition at a sample refractive index of 1.3325.

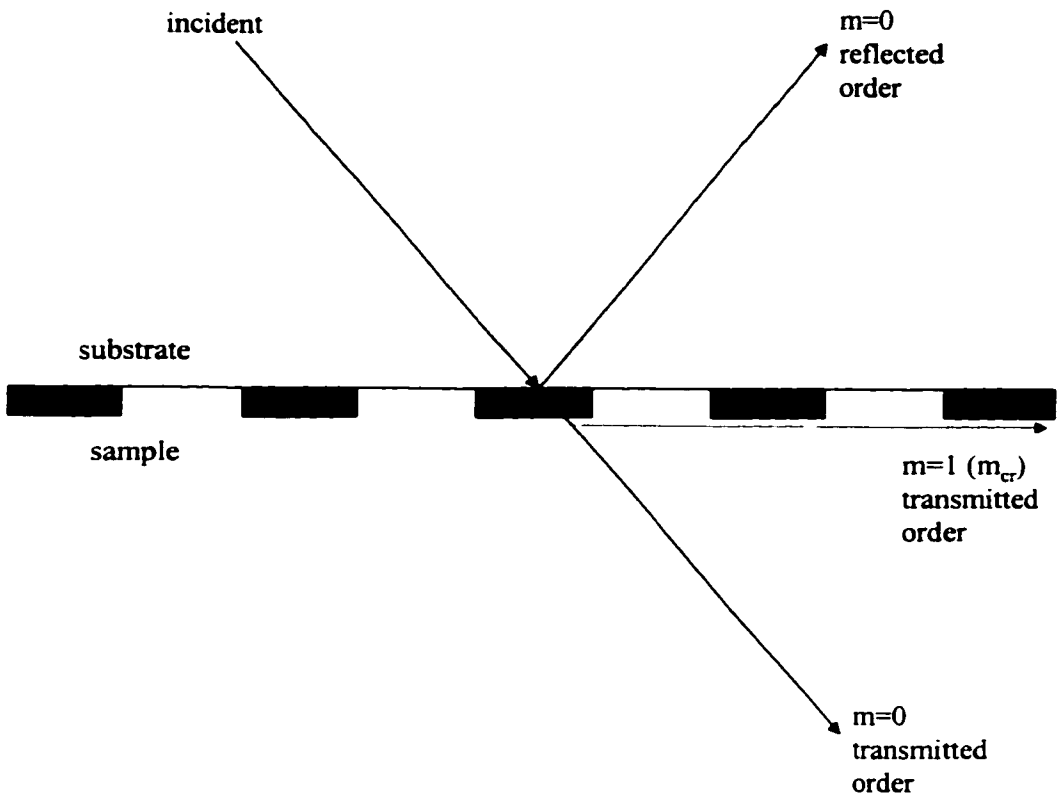

Figure 2.21 Basic schematic of the GLRS critical condition.

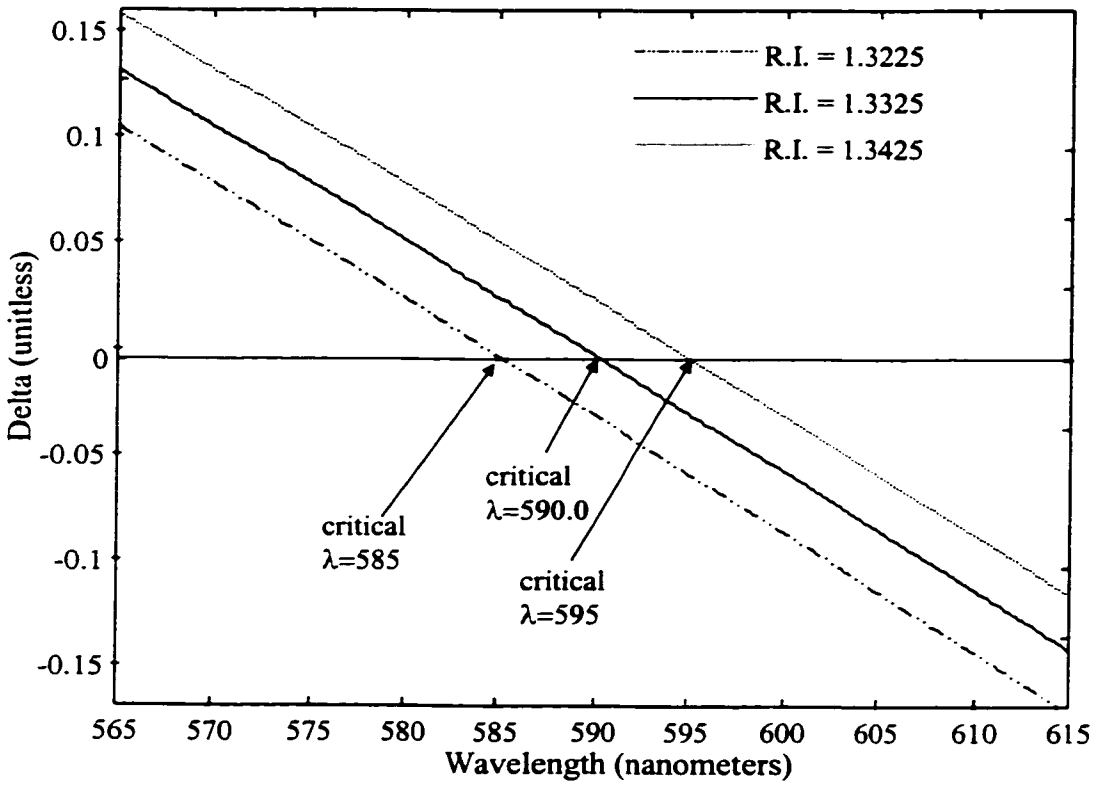

Figure 2.22 Change in δ as a function of refractive index using a grating period of ~830 nanometers.

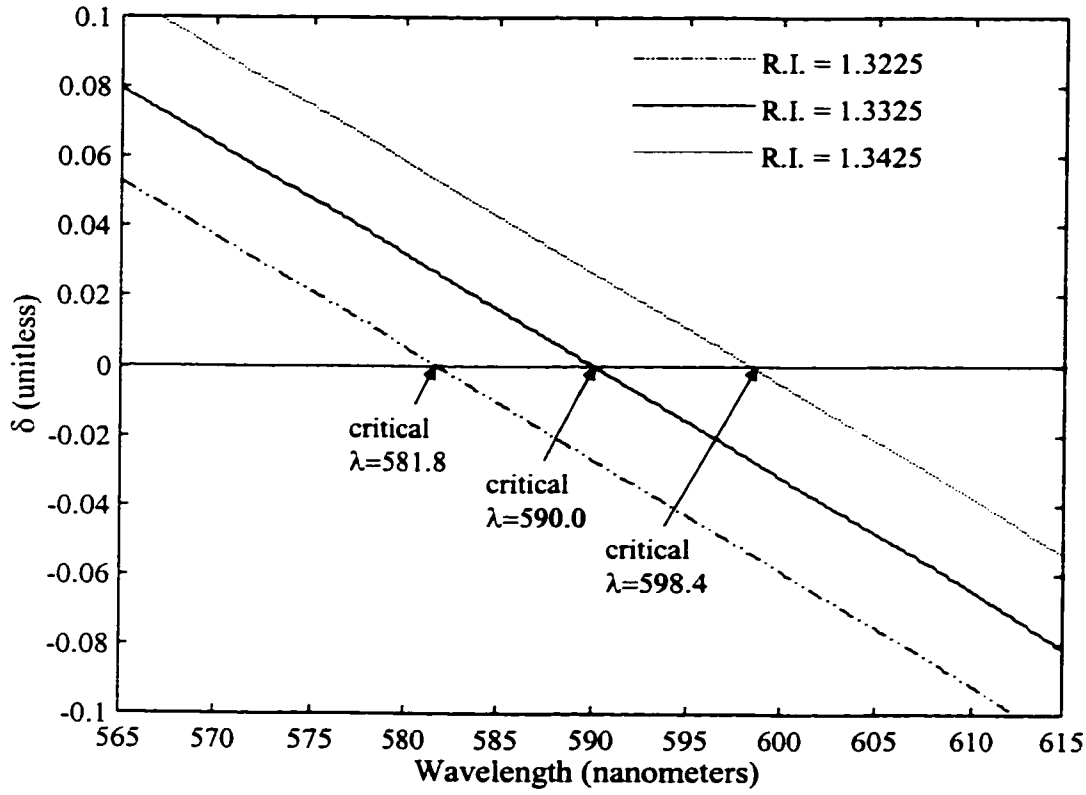

Figure 2.23 Change in δ as a function of refractive index using a grating period of ~500 nanometers.

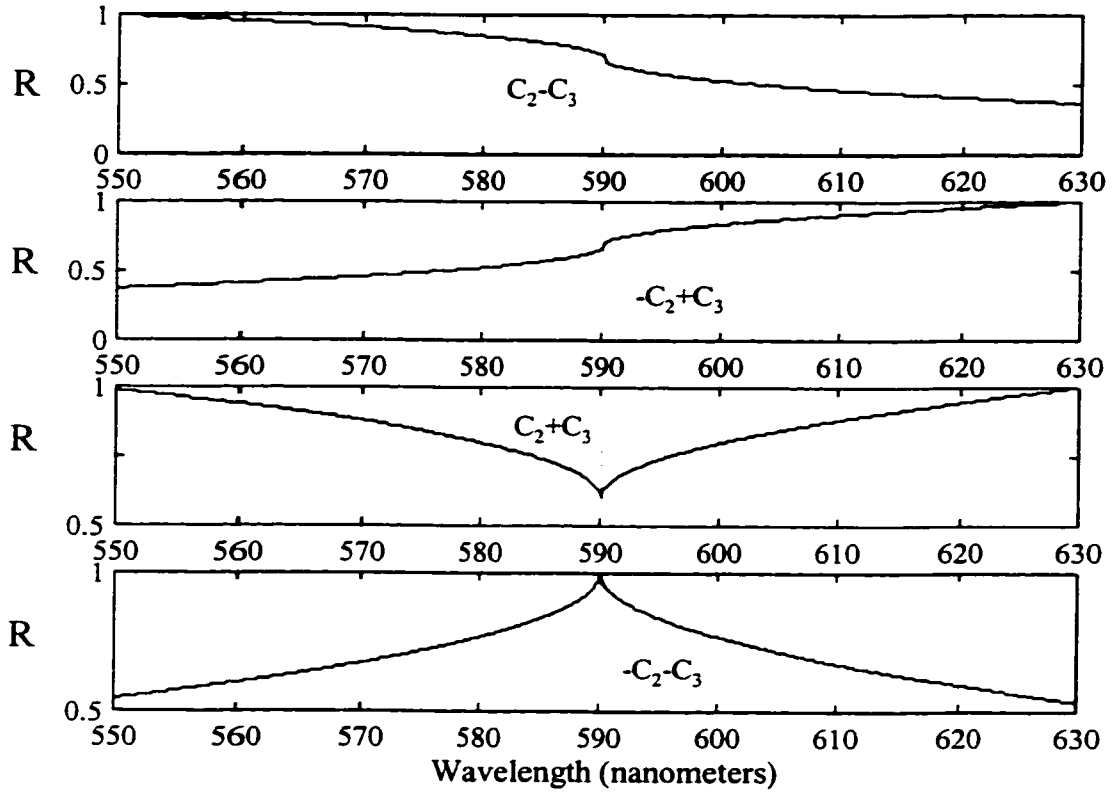

Figure 2.24 Spectral forms of the four possible combinations of grating / sample interface constants.

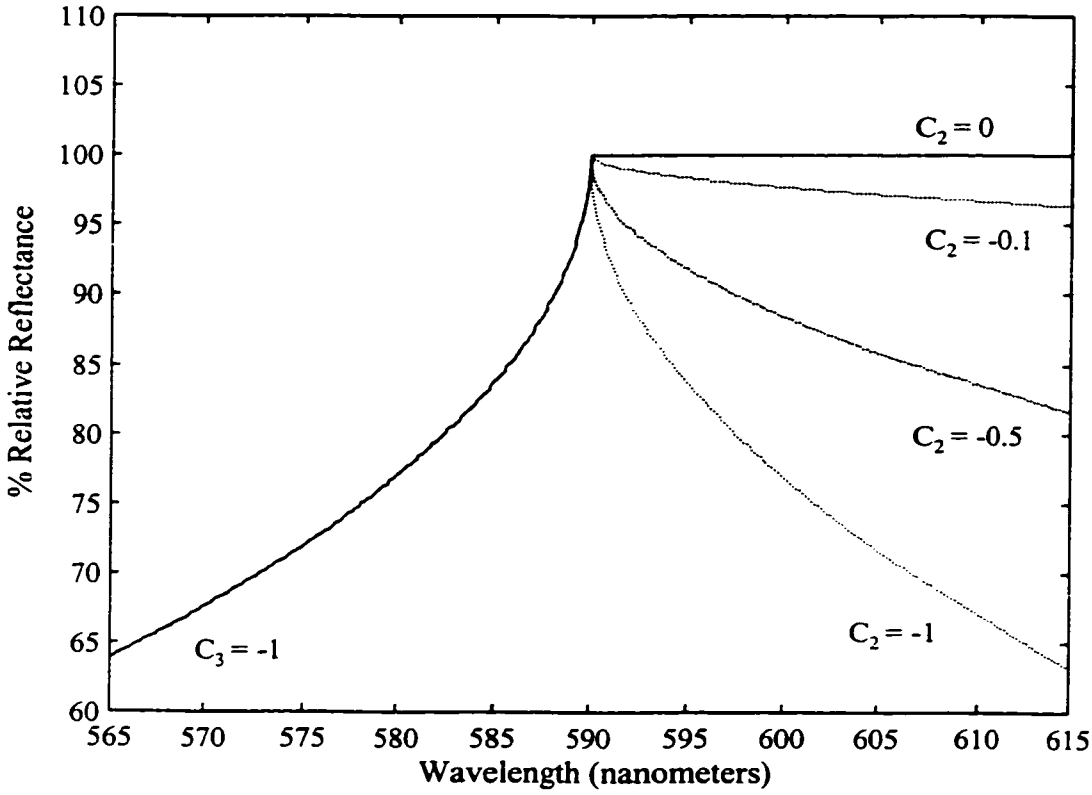

Figure 2.25 Effect of varying the magnitude of the second interface constant. This simulates different dielectric contrasts between the materials of the interface.

Chapter 3

Experimental Apparatus & Procedures

3.1 Introduction

The preliminary GLRS characterization work[37] necessarily focused on establishing a proof of principle for the technique, and so the experiments done therein were performed in the most basic and efficient manner possible. The initial apparatus design represented a compromise between optimum optical performance and expedient data collection, and the data analysis techniques were of a mainly qualitative nature, because the theory had not yet developed to the extent that it could be routinely used to quantify the GLRS data. Therefore, much of the effort detailed in this thesis involved optimizing the benchtop GLRS apparatus, especially the optical train and sampling interface, to allow for more accurate and precise measurements to be made in order to test the quantitative limits of the technique. In addition, this work took advantage of new advances in the GLRS theory that allowed for the raw spectral data to be fit to an ideal response, so that sample properties could be quantified without resorting to empirical fits

---

[37] Anderson, B. B. *Grating Light Reflection Spectroscopy*, Thesis (Ph.D.), University of Washington, **1996**.

or arbitrary calibrations. The following sections of this chapter will critique in detail these advancements of the practice of GLRS.

3.2 GLRS Benchtop Apparatus

3.2.1 Broadband Light System

Figure 3.1 shows the experimental apparatus used to quantify GLRS phenomena based on intensity redistributions in light reflected from a grating that contains a transmitted diffraction order undergoing a singularity event. This particular geometric arrangement was designed for potential use in process monitoring applications (for example, it anticipated the use of an automated dynamic sampling system, as described in section 3.2.2 below).

An optical fiber coupled a broadband light source (tungsten lamp or LED) to a collimator consisting of an achromatic focusing lens and an iris. The 100 micron fiber shown in the figure gives the best compromise between the resulting degree of collimation (which is inversely proportional to the size of the point source: so a smaller fiber will yield better collimation) and the light intensity available after reflection of the incident beam from the grating / sample interface. This was important because better incident beam collimation results in sharper and more intense singularity features in GLRS reflection spectra. However, if the incident beam intensity reduced too much, the amount of detector integration time required to yield a suitable spectrum increased

beyond the limits of efficient data collection (e.g. at most a few seconds per spectrum), especially for large sample sets.

A half-inch diameter, 30 millimeter positive focal length achromatic lens chosen to match the numerical aperture of the fiber provided the best possible collimation of the broadband light. However, this resulted in a collimated beam with a half-inch diameter, whereas the gratings used in these experiments were only a quarter of an inch wide; therefore, this beam was apertured down to one millimeter in diameter. This ensured that only the optimally collimated, on-axis light reached the sampling interface. The physical dimensions of the sampling interface also limited the maximum beam diameter (see section 3.2.2 below).

This resultant beam passed through a linear polarizer with a high extinction ratio (10000 : 1) before striking the front surface of the grating / sample interface. Due to the complexity of this dynamic sampling interface, it is presented separately in section 3.2.2 below. For all of the experiments presented in this thesis, only p- polarized light was used, since this produced the strongest sample / evanescent field interaction (see Chapter 2) and also yielded the most intense zeroth-order grating reflection. This is because the front surface of the grating substrate reflects s- polarized light more strongly than it does p- polarized light, so that more p- polarized is available at the grating / sample interface.

The grating / sample interface was mounted on a rotation stage with a 0.16° angular resolution. Note that this resolution is rather poor relative to the other parameters that determine the position of the singularity in wavelength space. For example, an

uncertainty of 0.16° in an angle scanning singularity determination made with the gratings used in these experiments (500 and 830 nanometer periods) is equivalent to a ~2 nanometer uncertainty in the singularity position in a wavelength scanning measurement (while the resolution of the current detection system - at 0.2 nanometers - is an order of magnitude better than that). However, as long as the angle is held constant, it imposes only an offset in the calculated position of the singularity and does not degrade the precision of sample determinations made with this GLRS apparatus.

Upon reflection from the grating / sample interface, the zeroth order grating reflection was collected by a 10x microscope objective for focusing into a 200 micron fiber, which then fed into a McPherson 218 diffraction grating monochromator with a Princeton Instruments 576e CCD detector for spectral intensity measurements. The microscope objective and 200 micron fiber collection optics were chosen to get as much light as possible from the zeroth order reflection to the detector. The size of the fiber input to the monochromator ultimately limits the spot size or resolution of its spectral components in the detector plane. However, with a 100 micron input slit on the front of the monochromator, the full-width-at-half-maximum of atomic emission lines used to calibrate the detector / monochromator pair was only 0.2 nanometers, or two CCD pixels. This performance is acceptable, considering that the physical limit of the obtainable resolution with this particular monochromator-camera pairing is 0.12 nanometers (600 lines per millimeter diffraction grating and 0.3 meter focal length, with 22 micron pixel size on the CCD). The resolution is slightly worse in practice due to minor misalignments

within the fiber optic input coupling system, and the 100 micron input slit width required to achieve reasonably fast integration times. This system enabled half-well capacity CCD spectra to be collected at less than 1 second per spectrum, so that a fair amount data averaging could be done within a short sample cycle time (less than two minutes, see 3.2.2 below). The dynamic range of spectra collected with this detection system was approximately 57 nanometers, at 0.1 nanometers per horizontal (wavelength axis) pixel on the CCD detector. Furthermore, long-term collection of atomic emission spectra showed that the wavelength reproducibility held constant at 0.1 nanometers.

3.2.2 Dynamic Sampling Interface

The dynamic, micro-channel sampling interface shown in figure 3.2 resulted from the desire to limit the consumption of expensive and hard to prepare samples, to decrease the amount of time required to collect data on large sample sets, and finally to increase the precision of GLRS measurements. The previous sampling interface consisted merely of an open tub sandwiched to the grating, through which samples were manually transferred. This required too much time, too much sample (several milliliters), and made reproducible sampling impossible. Therefore, in order to approach the quantitation limits of the GLRS technique itself, and not merely the limits of a particular implementation, it was necessary to optimize this interface.

The incident beam first passes through a cylindrical lens of 2.5 millimeter back focal length in order to focus the light into the sample channel while maintaining collimation in the optical plane. The lens, incident angle, and grating substrate thickness were chosen such that the focal point of the lens occurs at the grating/channel interface. Therefore, the full intensity of the incident light focuses within the "window" defined by the micro-channel height of 400 microns. In addition, due to the focusing limits imposed by the quality of the lens and the construction of the substrate (which consisted of several microscope slide cover slips sandwiched together with optically clear epoxy), the incident beam had to be at most 1 millimeter in diameter. Otherwise the spot size of the focused beam was larger than the height of the channel, and the excess intensity merely contributed a background to the reflection spectrum. The channel depth of 45 microns made the sampling volume 1 x 0.4 x 0.045 cubic millimeters or 180 nanoliters. The zeroth-order grating reflection was re-collimated by passing back through the cylindrical lens.

This square channel of dimensions was fabricated in PDMS using soft-lithography, a rapid and low cost prototyping method for micro-fabrication developed by Whitesides.[38] The masters for the micro-channels were designed on a computer using high-quality drafting software. Images were printed on a transparency using a high-

---

[38] Duffy, D. C.; McDonald, J. C.; Schueller, O. J. A.; Whitesides G.M. *Analytical Chemistry*, **1998**, vol. 70, no. 23, pp. 4974-4984.

resolution, 2560 dpi, printer. Negative photoresist was spin-coated onto 3 inch silicon wafers to a thickness of 45 ± 4 microns, measured using a profilometer. The channel patterns were then transferred into the photoresist using collimated UV light, and excess photoresist was removed using a developer. This procedure resulted in a "channel master": a template from which flow channels could be imprinted onto other materials.

The material of choice was polydimethylsiloxane (PDMS), brand name Sylgard 184 from Dow Corning. To form a micro-channel into this, the liquid polymer was mixed, degassed, and poured over the channel master. After curing for 1 hour at 65 °C, the PDMS was removed from the channel master, plasma treated to activate surface groups, and joined with the chrome-on-glass grating substrate, which was also activated in the same plasma. The channels were oriented perpendicular to the grating lines. Adhesion between the chrome substrate and PDMS was improved using a thin layer of Sylgard Prime Coat from Dow Corning prior to plasma treatment, being careful not to apply the Prime Coat to that portion of the substrate occupied by the grating.

Liquid reached the microfabricated channels through interconnects created in the PDMS by affixing glass posts to the master before pouring the elastomer. The posts were ground to an outer diameter slightly of less than 1/16 inch. Once channels were formed by joining PDMS to the glass slide, PTFE tubing, 0.010 inch i.d. x 1/16 inch o.d. was then epoxied into the holes left by the glass posts.

This flow channel was coupled to an HPLC pump, which delivered 10 microliter sample injections at a rate of 30 microliters per minute. Thus the injection plugs were 20 seconds long. Reflection spectra of aqueous sample were integrated over 0.8 seconds to achieve half-well intensity on the CCD , such that approximately 25 spectra were recorded of each sample plug profile. This arrangement resulted in a sample cycle time of two to three minutes.

Figure 3.3 shows a typical injection profile, where the singularity wavelength shifts in position for each reflection spectrum according to the refractive index of the sample in contact with the grating. Here, a plug of 7% NaCl in water was injected (refractive index = 1.356) using the flow parameters described above. Fifty consecutive spectra were then taken at 0.8 seconds per spectrum while the plug eluted past the grating / sample interface in a carrier solvent of pure water (refractive index = 1.3325). The critical wavelength for each 0.8 second integrated reflection spectrum was then calculated and plotted versus its run (i.e. spectrum) number. This wavelength shift plateaus over the course of several spectra, because the flow system is intentionally "overloaded" to produce flat injection peaks. This is opposed to a chromatographic system, where sharp peaks are required in order to accurately calibrate their appearance versus run time and to resolve any potentially interfering samples that may co-elute. For the present application, however, the micro-channel was used only as an automated sampler, with no consideration given to its chromatographic performance. The flat injections were desired

so that the spectra corresponding to the plateau resemble a steady-state measurement and could thus be averaged together.

The gratings consisted of holographically patterned chromium metal lines on fused silica substrates with a square groove profile, a 50% duty cycle, and a period of either ~1200 or ~2000 lines per millimeter (i.e. one metal strip every 830.4 or 503.6 nanometers, respectively). The gratings were formed on a chrome coated substrate holographically by exposing the interference pattern of an Argon ion laser beam to a layer of photoresistive material on the substrate, and then the chrome metal was wet chemically etched. The use of one grating period or the other was determined by the incident angle required to place a singlarity within a given wavelength range. For example, when measuring the absorption of aqueous methylene blue samples – which have an absorbance peak above 600 nanometers – the 1200 lines per millimeter grating was necessary to place the incident angle at ~35°. For the 2000 lines per millimeter grating, a 4° incident angle would have been required; this would have resulted in virtual overlap of the incident and reflected beams, such that the physical orientation of the optical train would have been impossible to implement. The physical limit of the optical train with the 2000 lines per millimeter grating was a 9° incident angle, sufficient to yield a singularity at 590 nanometers in aqueous samples.

3.2.3 Phase-Sensitive Experimental Setup

To conduct phase-based GLRS measurements, a HeNe laser replaced the broadband light source, see figure 3.4. This expanded and collimated beam again passed through a polarizer before striking the bare 830 nanometer grating substrate. For these experiments, a thermoelectric temperature control unit "sandwiched" onto the grating substrate proved necessary to control the temperature of the sample, due to the enhanced sensitivity of the phase response to such changes. The front substrate reflection overlapped with the grating interface reflection to form an interference fringe pattern that falls on a diode array. The relative phase angle response at the grating / sample interface was measured by monitoring how the alternating light-and-dark fringes of this pattern shift across the array.

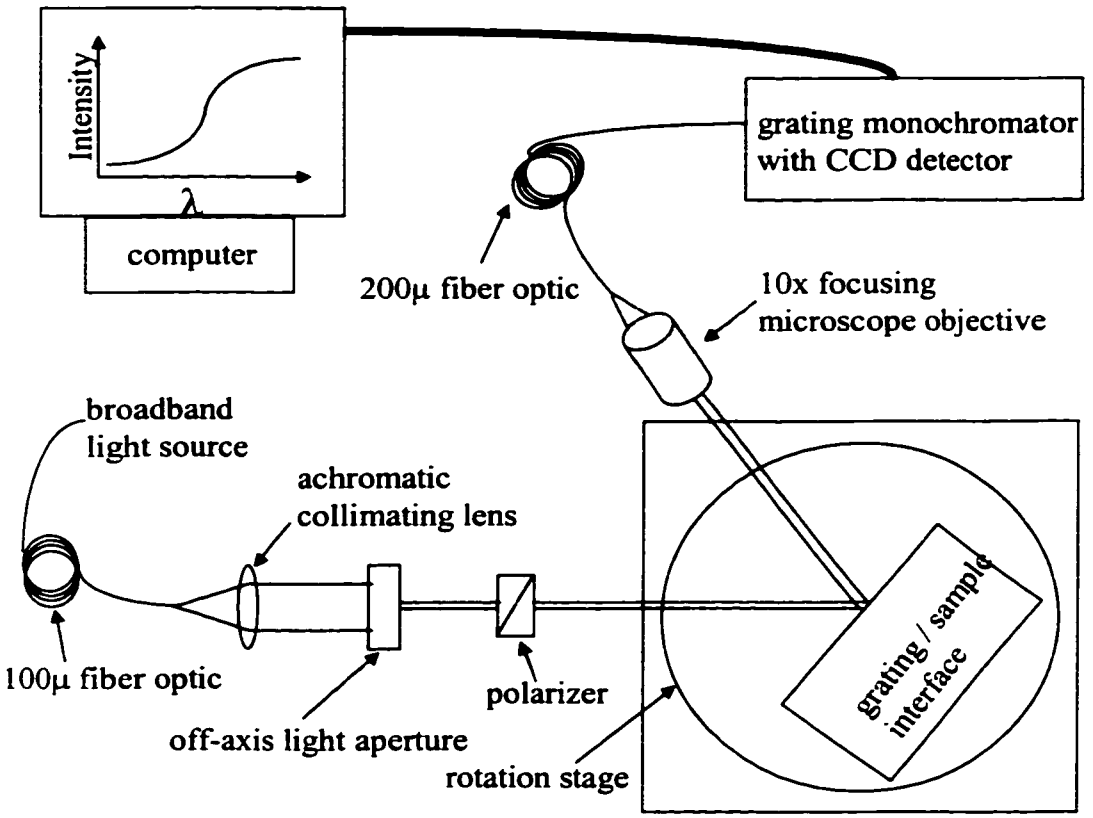

Figure 3.1 GLRS optical bench apparatus

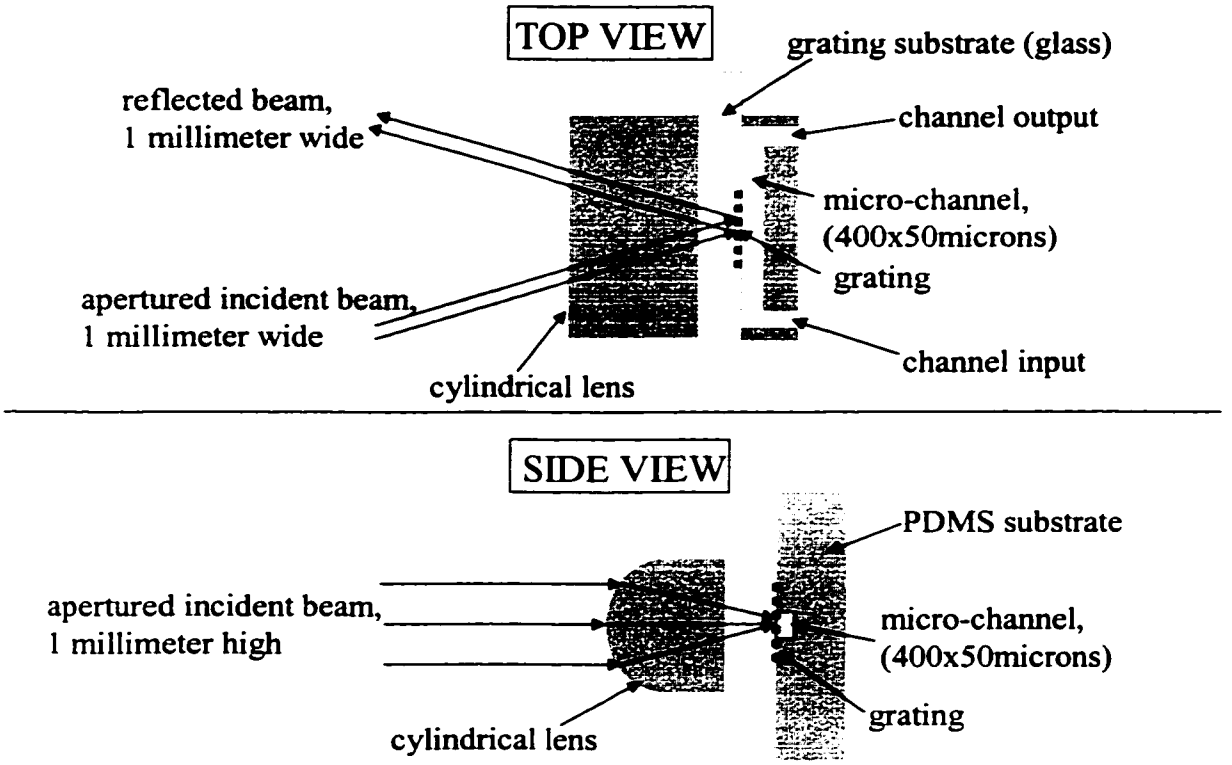

Figure 3.2 Optical coupling at the grating / sample interface of the micro-channel flow cell.

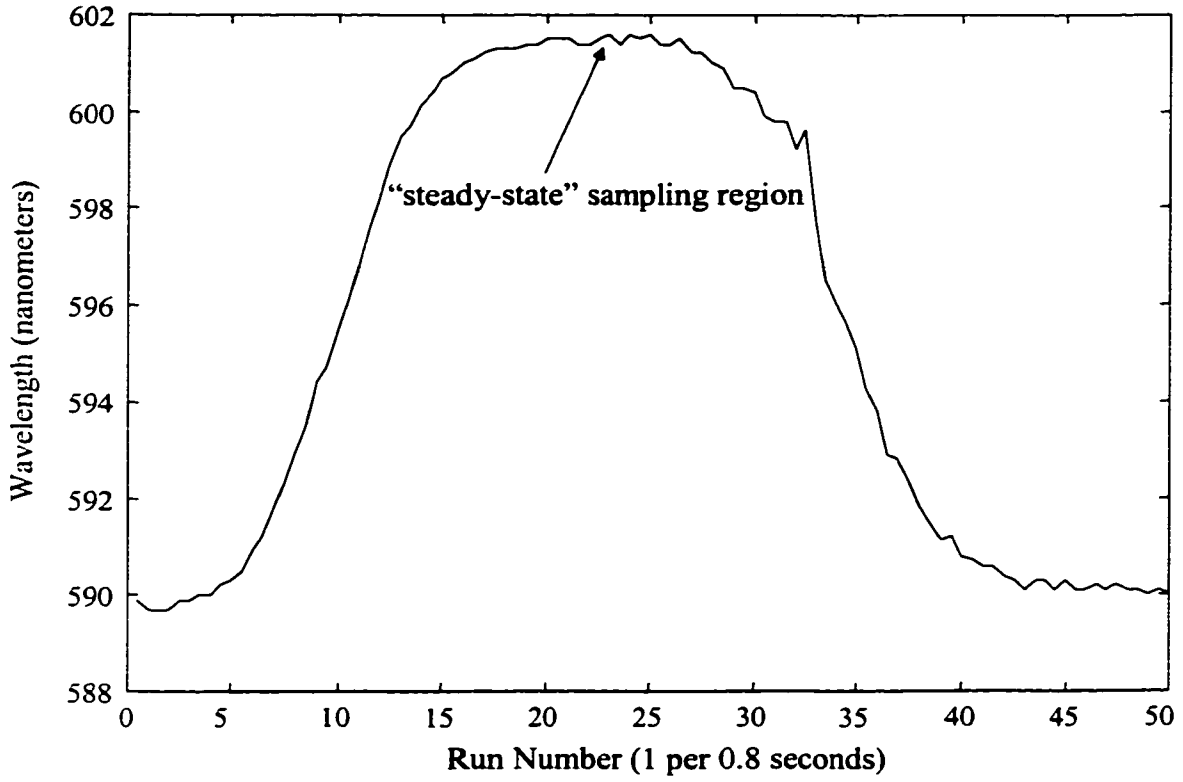

Figure 3.3 Typical injection profile, shown as the shift in the critical wavelength as the sample flows past the grating interface.

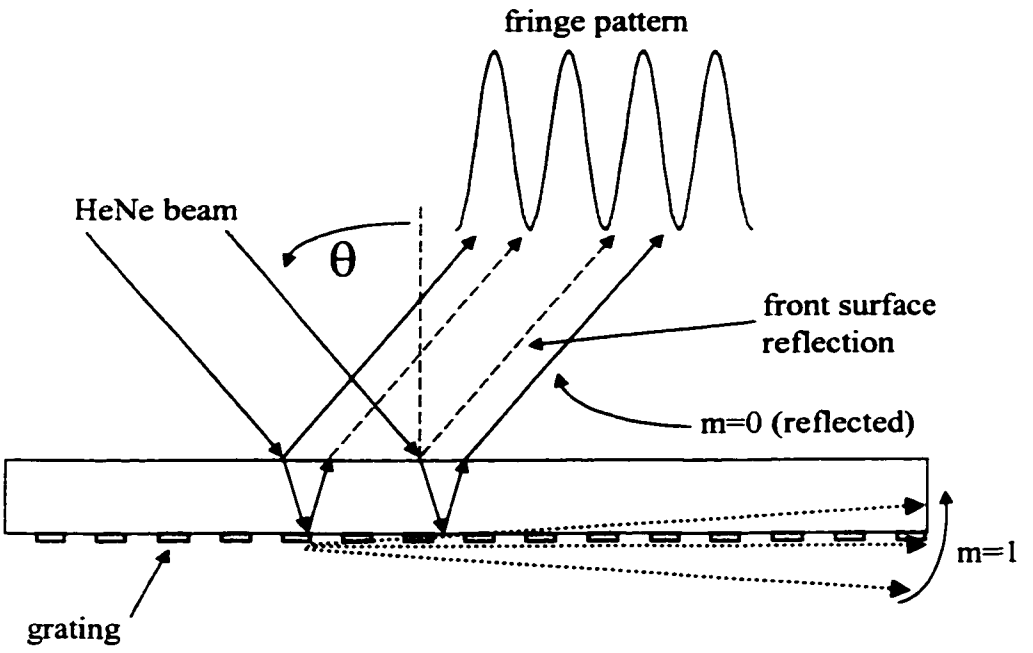

Figure 3.4 Schematic of the principle of the critical point phase measurement.

Chapter 4

Analysis of GLRS Data

4.1 Introduction

GLRS reflection spectra are expected to follow the same trends exhibited by the Fresnel coefficients discussed in the Theory section. A change in sample dielectric properties should induce a sharp change in the position and reflectivity of the critical point, and a less intense change in the reflectivity at wavelengths outside the critical region. The real part of a sample's refractive index (n) determines the wavelength position of the critical point, while its imaginary refractive index (K) affects the sharpness of the critical point due to absorption-induced coherence losses in the evanescent wave. In addition, the sample's real refractive index will cause reflectivity changes predominately in wavelengths to the transmitted side of the critical point. In contrast, the sample's imaginary refractive index will cause these changes to occur mainly in wavelengths to the evanescent side of the critical point. Figure 4.1 shows theoretically calculated difference spectra for n and K changes on the order of those typically encountered in GLRS experiments. These spectral response features set GLRS apart from other spectroscopic methods: there is no absorbance "peak" in the raw data, and overall reflectivity changes are an integral part of the response, and not merely a subtractable

baseline shift. This presents a challenge with respect to quantitating these reflectivity changes.

Furthermore, the use of a diffraction grating superimposes a high-frequency "baseline" on the reflectivity spectrum. This response depends on the groove profile of the grating and the number and scale of imperfections in the grating periodicity. Because a grating can be thought of as the Fourier transform of its diffracted spectra, the magnitude and frequency of these fluctuations are inversely proportional to the number and distance scale of the imperfections. For example, a dust mote entrapped in the photoresist of a holographic grating substrate prior to exposure will superimpose a "crater" of concentric circles onto the grating periodicity within a certain radial distance of the particle. A number of such particles, randomly positioned throughout the area of the substrate, will induce numerous such patterns in the final grating, each with a periodicity inversely proportional to the size of its "seed" particle. In the final grating structure, these will act as randomly overlapping diffraction gratings with respect to an incident beam, and will thus superimpose their own "diffraction orders" onto that of the actual grating orders. Spectroscopists commonly refer to these features as "ghosts" in the diffracted spectral intensity (though there are other types of "ghosts", arising from other sources of periodicity error).[39]

---

[39] A detailed discussion of these phenomena is found in: M.C. Hutley, Diffraction Gratings, London, Acamedic Press, 1982.

However, the reflectivity theory derived for GLRS assumes a perfect grating that has absolutely no erroneous spectral structure. In addition, since a change in the dielectric contrast of the grating / sample interface alters the amount of energy propagated into the transmitted and reflected diffraction orders, we expect the magnitude of these "ghosts" to change from sample to sample. This, in addition to the quasi-random frequency structure of the fluctuations, means that this response cannot be subtracted or otherwise filtered from the data without significantly altering the form of the reflection spectrum. However, while this affects the appearance of the spectra, it does not necessarily degrade their signal-to-noise ratio, as will be demonstrated below.

Finally, the GLRS theory also assumes the use an infinitely long grating. This means that the diffracted wavelengths are infinitely resolved from each other, so that the critical point contains only "one" wavelength (in the absence of absorption-induced coherence losses). Thus the sharpness of the critical points will be reduced as a lower number of grating grooves are illuminated, so that there will be some coherence loss in the evanescent wave even in the absence of sample absorption. However, as opposed to the fluctuations described above, this feature does not depend on the properties of the sample, and so it can in fact be regarded as a baseline response that the data can be referenced against.

4.2 GLRS Refractive Index Response

Figure 4.2 shows the corrected reflection spectra for a series of aqueous NaCl refractive index standards, the properties of which are listed in table 4.1. For this experiment, the 503.6 nanometer period grating was used at an incident angle of 9.4°. The refractive index of each sample was determined using an Abbe refractometer with a resolution of $10^{-4}n$. Each spectrum is the mean of four separate injections performed using the dynamic flow system described in the Experimental section, with five spectra extracted from each steady-state injection peak (so that each sample was effectively an average of twenty spectra). The spectra were corrected by first normalizing them to have equal intensities on pixel #1, in order to remove any overall intensity fluctuations caused by source drift. Then they were divided by a "flatfield" reference consisting of a reflection spectrum with air in contact with the grating. For air, no critical point occurs in the wavelength region of the water critical point, so that this reference serves to correct for wavelength-dependent variations in the optical system. Finally, the referenced spectra were smoothed with a seven-point Savitsky-Golay 3rd order polynomial filter. This filter width was chosen because, when applied to theoretically ideal reflection spectra, it fit the critical point (i.e. an extremely sharp feature) to a tolerance two orders of magnitude lower than the ~0.04% random noise level in the intensity of the actual data. This noise level is the mean relative standard deviation of the spectral intensity differences for a group of five separate corrected and 5x-averaged injections of a given sample (calculated

from the five water sampling shown in figure 4.9). Therefore, any filter-induced reflectivity changes would not be analytically significant.

The theory predicts that the critical wavelength will shift as the refractive index of the sample changes. Because of this, we had previously taken the 1st derivative of the data and determined the critical wavelength from the peak of this derivative spectrum. However, the process of calculating a derivative necessarily lowers the signal-to-noise ratio of the data. In addition, when the data contains high-frequency structure, the shape of the derivative will change drastically depending on the spectral width over which the derivative is taken, and on the degree of overlap of the incidental structure with the feature of interest (i.e. the critical point). Figure 4.3 illustrates these phenomena for the set of NaCl standard derivative spectra. The main peaks become distorted as the critical point "rides over" the high-frequency grating structure, so that a determination of the true center of the peak becomes impossible. Furthermore, a 71-point derivative filter width was required to produce even these spectra; smaller widths result in successively less well-resolved main peaks.

A much more efficient method for calculating the optical properties of a sample is to simply subtract a reference reflectivity from the sample's reflection spectrum. This produces data of the form of figure 4.1, from which the optical properties of the sample can be calculated based on the peak reflectivity difference that occurs at the critical wavelength. Figure 4.4 shows the difference spectra calculated for the refractive index standards, and the last column of table 4.1 contains the critical point reflectivity

difference for each salt sample relative to water. Notice that subtracting the water "baseline" response has not eliminated the high-frequency structure due to grating inhomogeneities. As described in section 4.1 above, the magnitude of these features increases as the dielectric difference between the sample and the reference increases. Regressing these reflectivity differences against the measured refractive index of the standards obtains a linear calibration of 0.0013 n / R, which is in very close agreement with the theoretically calculated value of 0.0012 n / λ in terms of wavelength shifts. To obtain a detection limit for this particular experiment, the random error in the reflectivity was determined from the average magnitude of the reflectivity differences of four water measurements taken between each of the salt injections relative to the initial water "baseline" response. As indicated in table 4.1 and figure 4.4, this value was 0.03% R. Taking the detection limit as three times the noise yields a value of $\sim 10^{-4} n$. This is reasonable, given the limit of the Abbe refractometer reference values and the resolution limits of the GLRS experiment itself: theoretically, a 10^{-4} shift in n would shift the position of the critical wavelength by 0.05 nanometers ($\partial\lambda/\partial n = \Lambda$). As discussed in the Experimental section, the detection system resolution is only 0.2 nanometers. However, the theoretical data shows that the reflectivity actually changes over the entire spectral range, so that the main reflectivity dip is significantly wider than the magnitude of the reflectivity shift. Therefore, in this case the limit of detection is not limited by the performance of the optical system, or by the resolution of the GLRS grating, which for the 1 millimeter incident beam width used in this experiment was ~0.3 nanometers. This

number was calculated as follows. Grating resolution is directly proportional to the number of grating periods illuminated, calculated by: 1/.0005 millimeters per groove = 2000 grooves per millimeter x 1 millimeter = 2000 grooves. So at lambda = 590 nanometers in the first diffraction order the resolution is 590/(2000x1) = 0.295 nanometers. Note that in some cases the resolution of the GLRS grating *can* be the bottleneck to the limit of detection: see Chapter 6. This situation occurs when the resolution of the grating is larger than the width of the reflectivity dip.

4.3 GLRS Absorption Response

To model the GLRS absorption response, a set of aqueous methylene blue dye standards was formed. Table 4.2 lists the concentration, Beer's Law absorbance, and imaginary refractive index values for each of these. The spectra were generated using the same procedure described above for the refractive index standards. For these runs, however, the 830.4 nanometer period grating was used at an incident angle of 34.8°, with a 2 millimeter wide incident beam. Figure 4.5 shows the resulting reflection spectra. First of all, it is interesting to note that in this case the GLRS grating has a resolution of ~0.26 nanometers, but that the wavelength-dependent rate of change of the critical order wave-vector is significantly greater than for the refractive index experiment. To illustrate this, the water baseline spectra of each sample series are shown on the same axis in figure 4.6. The critical point is significantly sharper for the larger grating period, even though

the resolutions of the two experiments are virtually the same. In addition, the high-frequency structure in these spectra is different: this is obviously because these spectra were obtained using two different gratings.

Figure 4.7 shows the difference spectra for the samples of the four highest dye concentrations. As expected, the reflectivity dips are much sharper than those for the refractive index standards. The high-frequency "ghost" structure is present in all the spectra, even though its amplitude decreases significantly as the dye concentration decreases. Also, the theory predicts that the magnitude of the dip for a change in the imaginary refractive index will be significantly less than that for a real refractive index change of equal magnitude. This is evidenced by the difference spectra of the two smallest dye concentrations, shown in figure 4.8 together with the average difference spectrum (i.e. the noise spectrum) of five water runs performed between the dye injections. As a visual illustration of the magnitude of the reflectivity changes involved, the five water spectra are shown together in figure 4.9.

If the magnitudes of the reflectivity dips were used to determine the GLRS limit of detection with respect to sample absorption, as was done for refractive index, one would conclude that concentrations below ~ 4 A.U. ($K \sim 0.0001$) could not be quantified. The reflectivity dip associate with absorption is associated with a loss of coherence in the evanescent wave, so once the absorption of a sample goes below a threshold value, the *difference* in coherence between it and the reference reflectivity spectrum at the critical point will be too small to resolve. It must be remembered, though, that reflectivity

changes occur throughout the region of the critical point, so that the reflection spectra will be offset from the baseline reference regardless of the magnitude of the dip at the critical point. To prove this, the entire set of difference spectra for the six dyes and five water spectra were mean-centered and a principal component analysis was performed on them. As shown in figure 4.10, all of the dye difference spectra are well-separated from the five water difference spectra. The extreme separation of the 5e-3 M dye sample is due to the fact that the GLRS absorbance to it is so much greater than the response to the other dyes. Figure 4.11 shows that the first variable loading was formed solely to fit this sample, since the principle component formed by the projection of the score for this sample onto the 1^{st} loading recreates the mean-centered difference sample for 5e-3 M dye almost exactly. Figure 4.12 shows how the second loading incorporates much more of the offset in the residual reflectivity differences. Specifically, note that it models the way in which the high-frequency grating structure "rides on top of" these reflectivity changes. Therefore, once the large variation due to the 5e-3 M sample is accounted for via the first principle component, the second principle component clearly correlates the remaining absorber concentrations to changes in reflectivity.

This result demonstrates the significant increases in sensitivity to absorption that occur with a reflection technique when the measurement is conducted not merely *near* the critical point (as with ATR), but in the region bounding the critical point. The limit of detection with respect to absorbance (between .01 and 0.1 A.U.) can approach within two orders magnitude of a transmission-based measurement done at the same wavelength.

This is expected though, based on the evanescent wave penetration depth determinations illustrated in the Theory section. These predicted a value in excess of 20 microns for an evanescent wave generated *at the critical angle* on a water / fused silica interface. This value is within 2 orders of magnitude of the 1 centimeter pathlength of a conventional transmission-based UV-vis spectrophotometer. For this to be realized, however, a multivariate analysis method should be used in order to utilize all of the reflectivity information contained in the wavelength region of the critical point.

4.4 GLRS Phase Response

We performed phase angle measurements using the arrangement shown in figure 3.4 to demonstrate that singularities exist in the phase response to a singularity, and not just in the intensity response. The data presented in figure 4.13 shows this occurrence with methylene blue in water at 10^{-4}M. Notice that the thermoelectric temperature control element could not prevent an enormous temperature component from appearing in the phase response upon sample introduction. However, after allowing the sample to equilibrate, a stable phase angle was reached. Since we used a monochromatic light source for these experiments, we manually rotated the grating over a sequence of incident angles that bounded the singularity condition for the sample refractive index (n = 1.331 at 633 nm and 22° C). As the right hand portion of figure 4.13 shows, a singularity does indeed appear in the region of the expected incident angle for this experiment. Note that

none of the points in the graph represents the actual singularity; we can only say that this data bounds the singularity, as evidenced by the derivative peak. This confirms the possibility of performing phase-based measurements, as expected by GLRS theory. Therefore, this preliminary result is very important in that it confirms the accuracy of the theory and establishes the possibility of taking advantage of this effect in the future, to either harness the extreme sensitivity inherent in phase measurements or to use the determine the presence of anisotropic (i.e. "optically active") analytes. However, the experimental method requires improvement to make such measurements practical.

Table 4.1 **Refractive index standards, with the critical point reflectivity difference for each salt sample relative to water.**

Sodium Chloride Concentration, %w/w	Refractive Index	Peak Reflectivity Difference, %
0	1.3325	0.03
1.1	1.3362	-2.986
2.2	1.3400	-5.974
3.3	1.3440	-9.048
4.4	1.3475	-11.89
5	1.3501	-13.88

Table 4.2 Properties of the methylene blue absorption standards.

Methylene Blue Concentration, M	Absorbance At 631nm	Imaginary Refractive Index (K)
0.000001	.08	0.0000009
0.00001	0.4	0.000005
0.0001	~3.8	0.00004
0.0005	~16	0.0002
0.001	~28	0.0003
0.005	~135	0.002

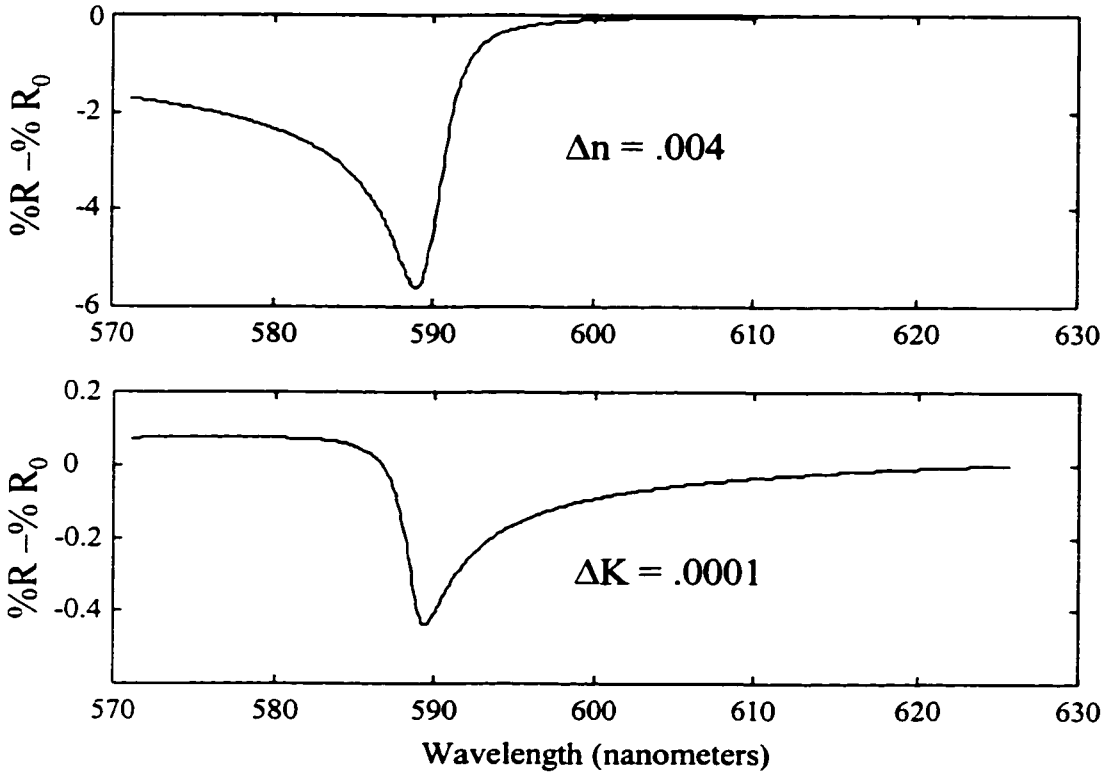

Figure 4.1 Hypothetical Reflectivity difference spectra for typical *n* and *K* changes.

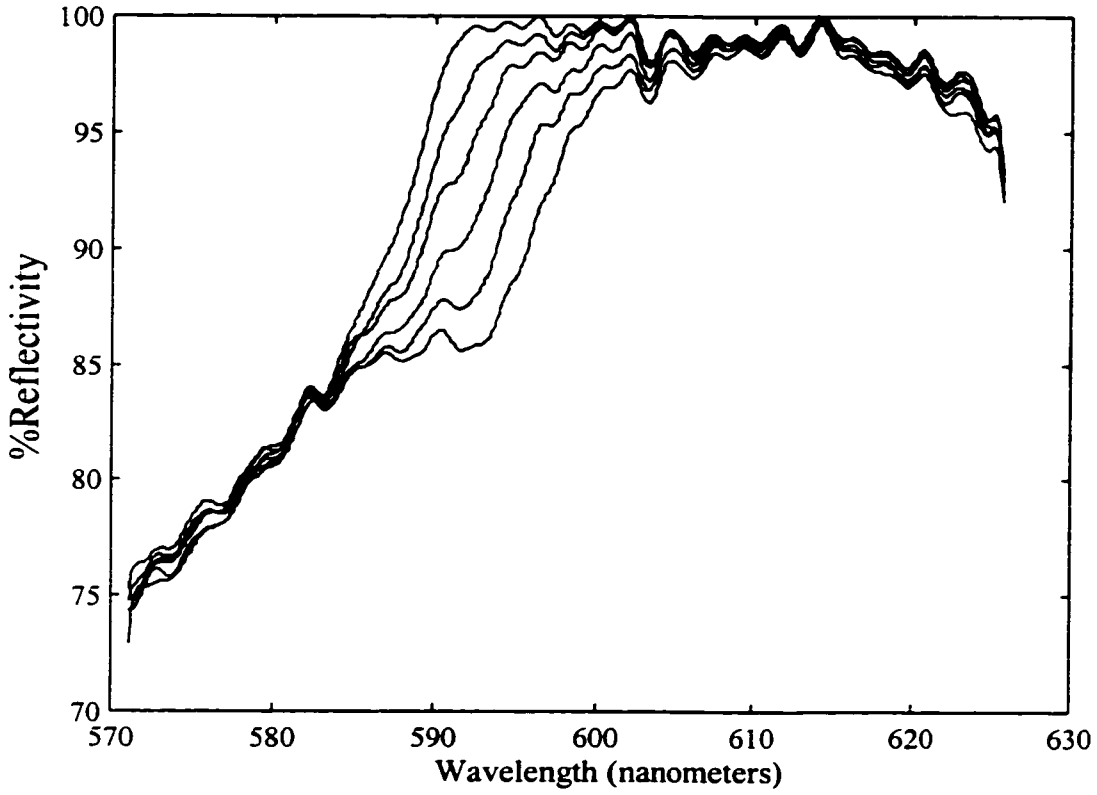

Figure 4.2 Corrected reflectivity spectra of the refractive index standards.

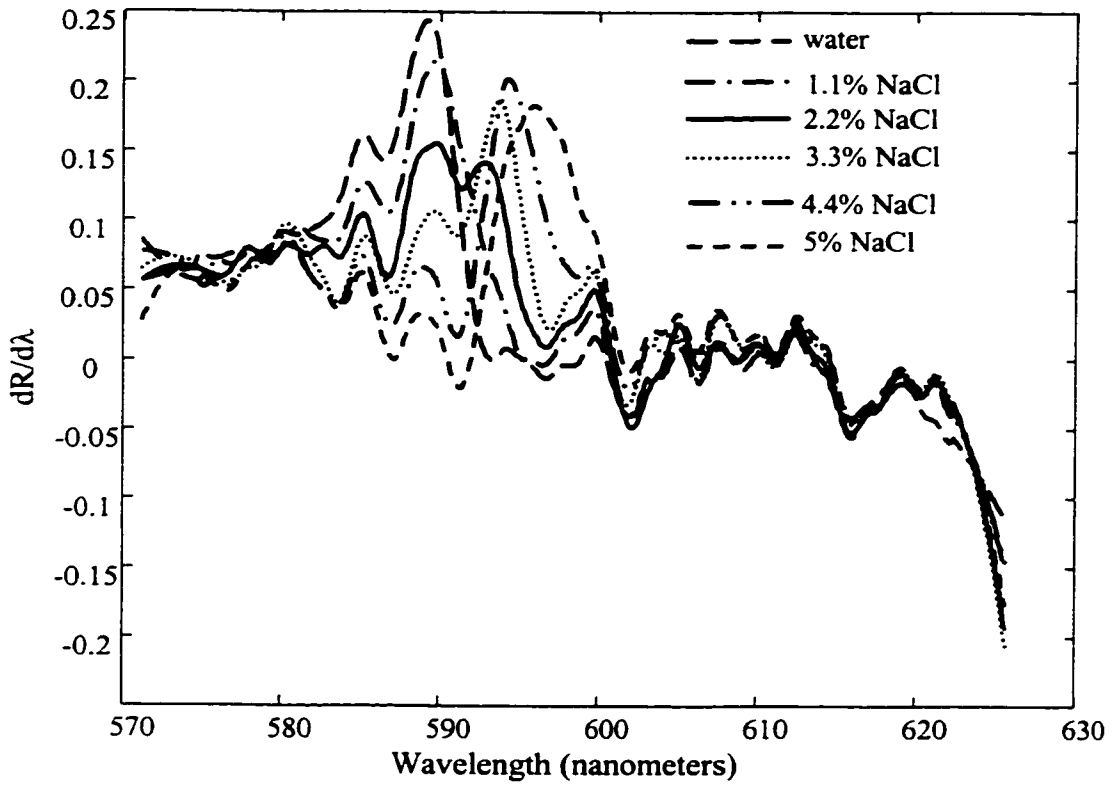

Figure 4.3 71-point window derivative spectra of the refractive index standards.

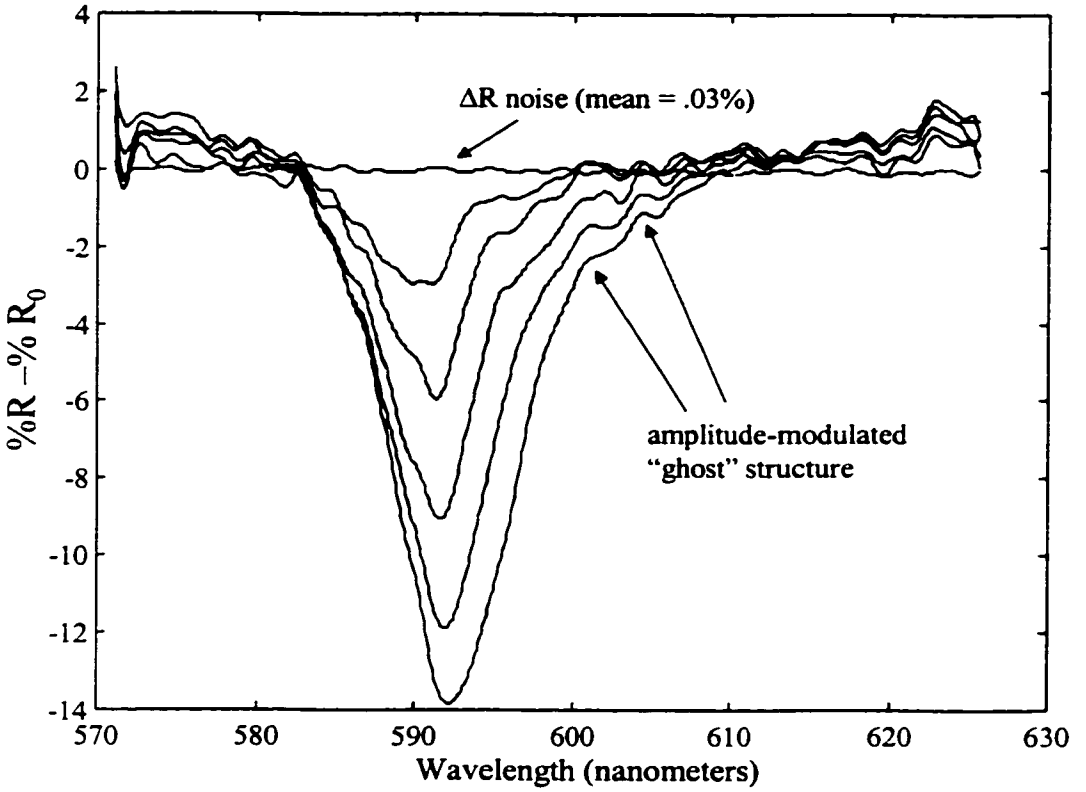

Figure 4.4 Difference spectra calculated for the refractive index standards.

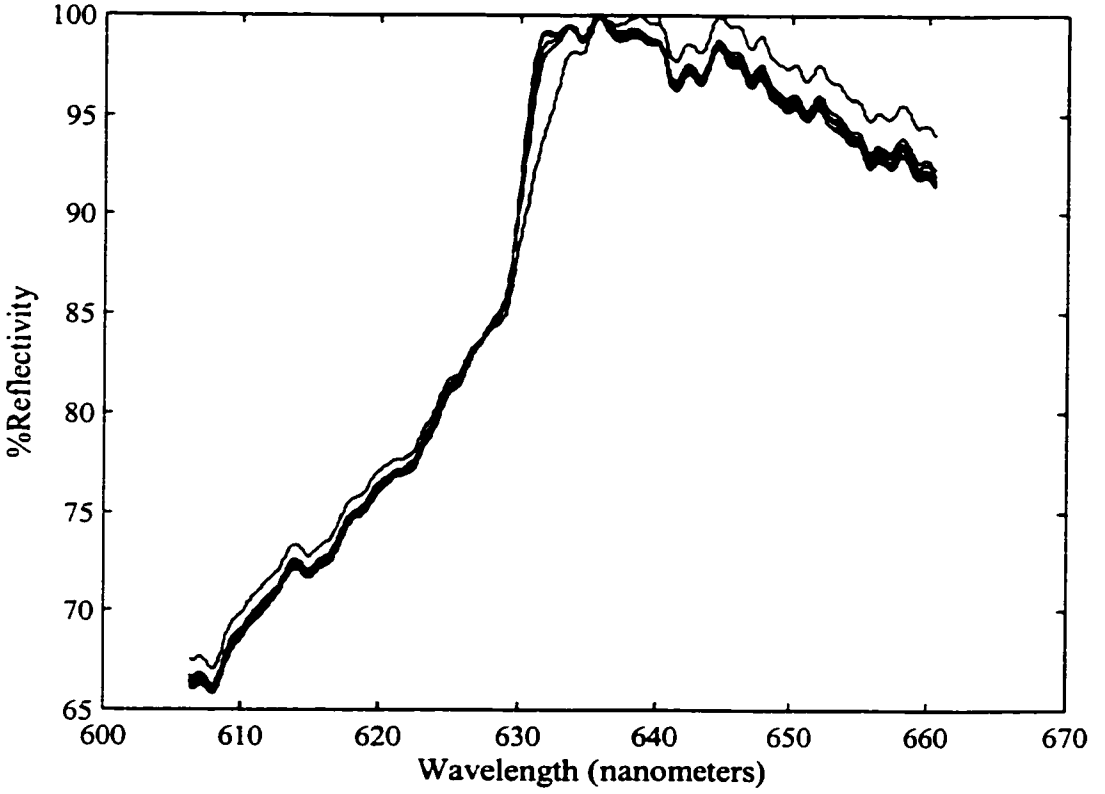

Figure 4.5 Corrected reflectivity spectra of the absorption standards.

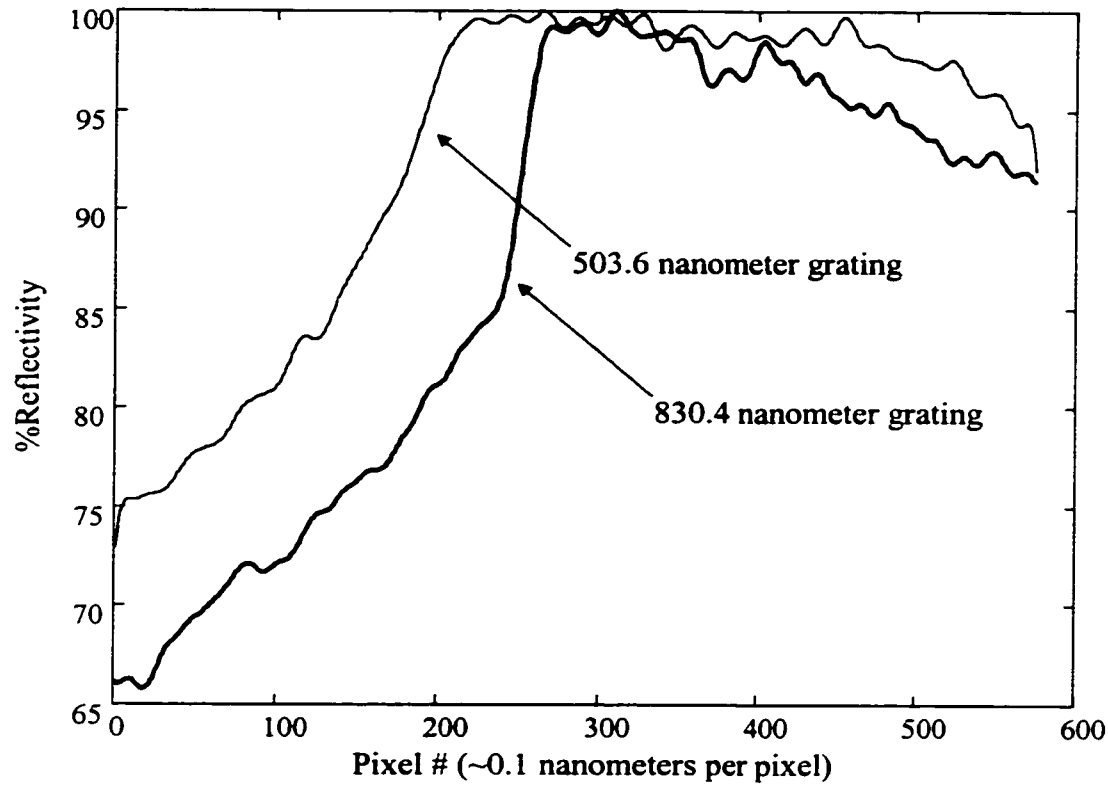

Figure 4.6 Overlay of the "baseline" water spectra taken with the 503.6 and 830.4 nanometer gratings.

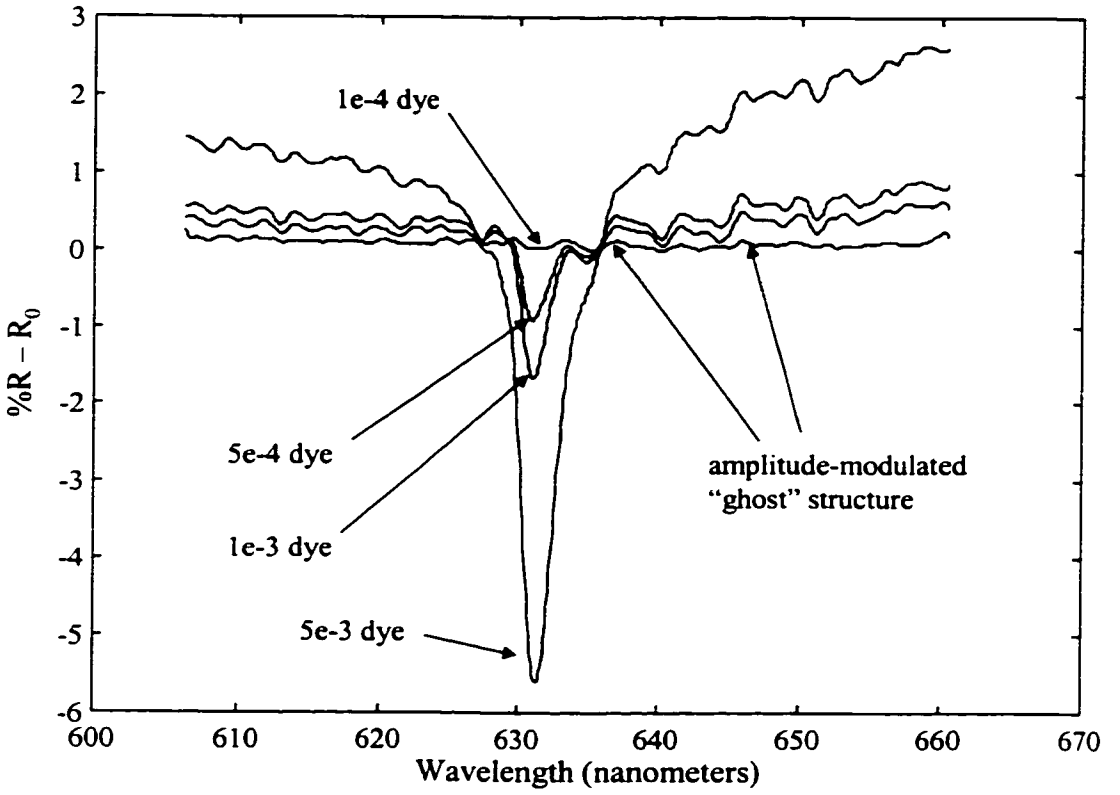

Figure 4.7 Difference spectra for the samples of the four highest dye concentrations.

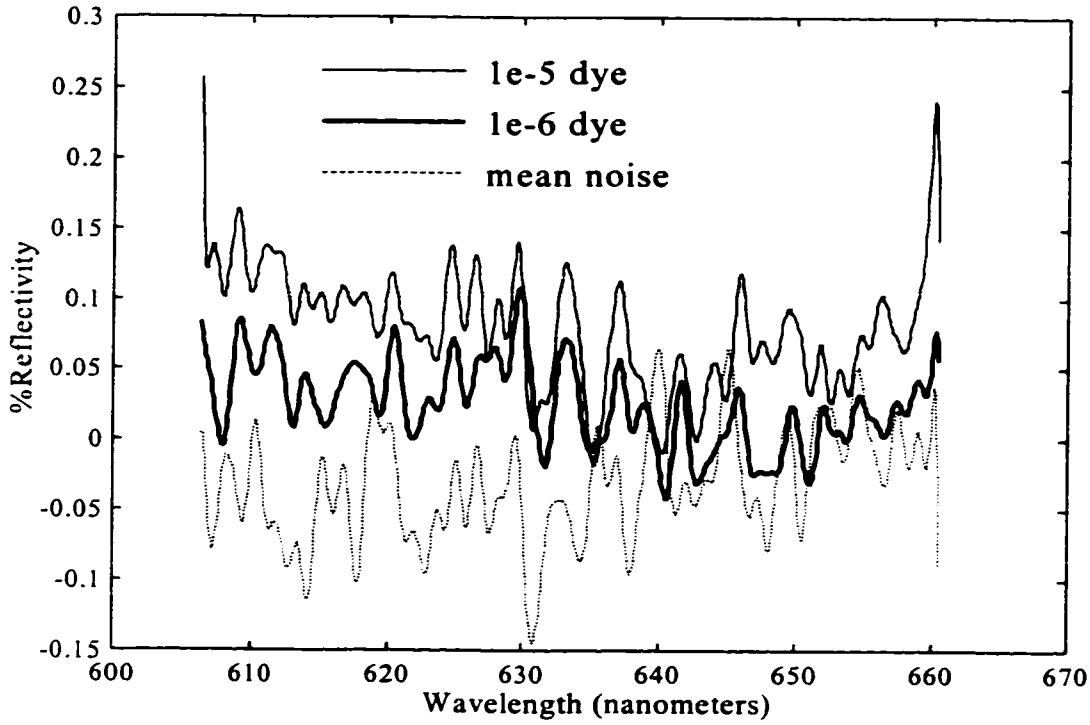

Figure 4.8 Difference spectra of the two smallest dye concentrations, together with the average difference spectrum (i.e. the noise spectrum) of five water runs performed between the dye injections.

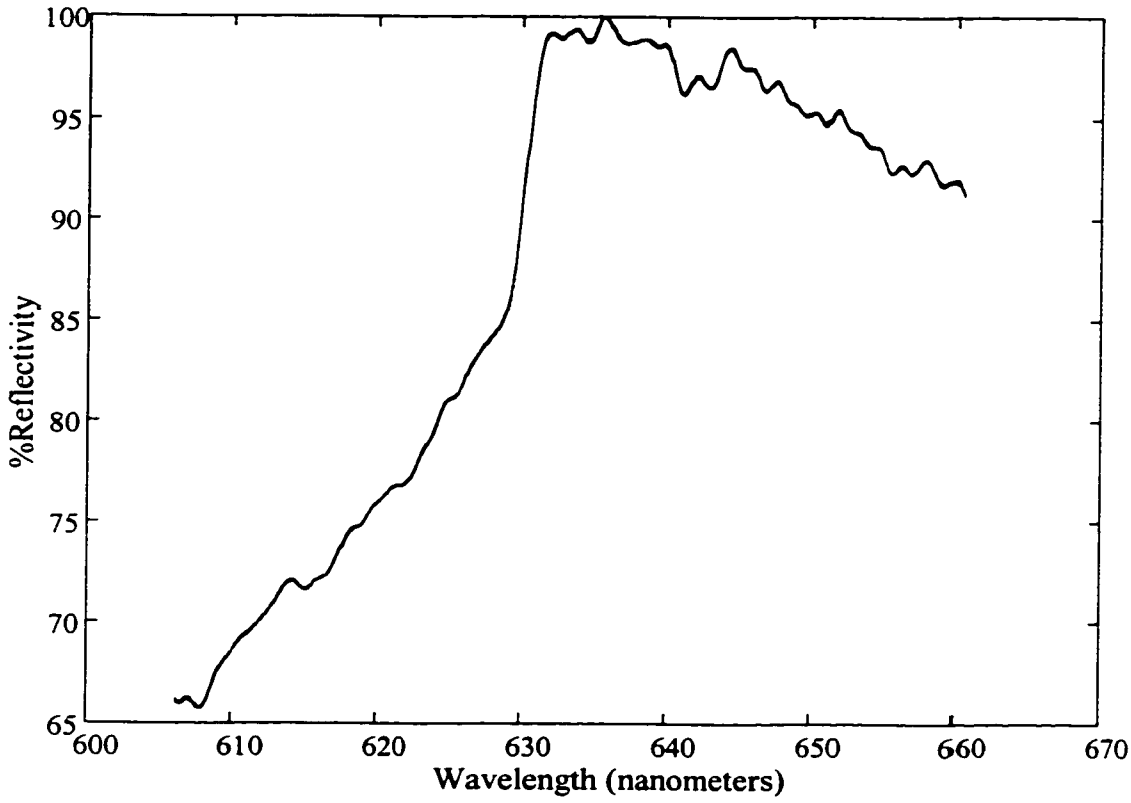

Figure 4.9 Corrected Reflectivity spectra of the five water samples.

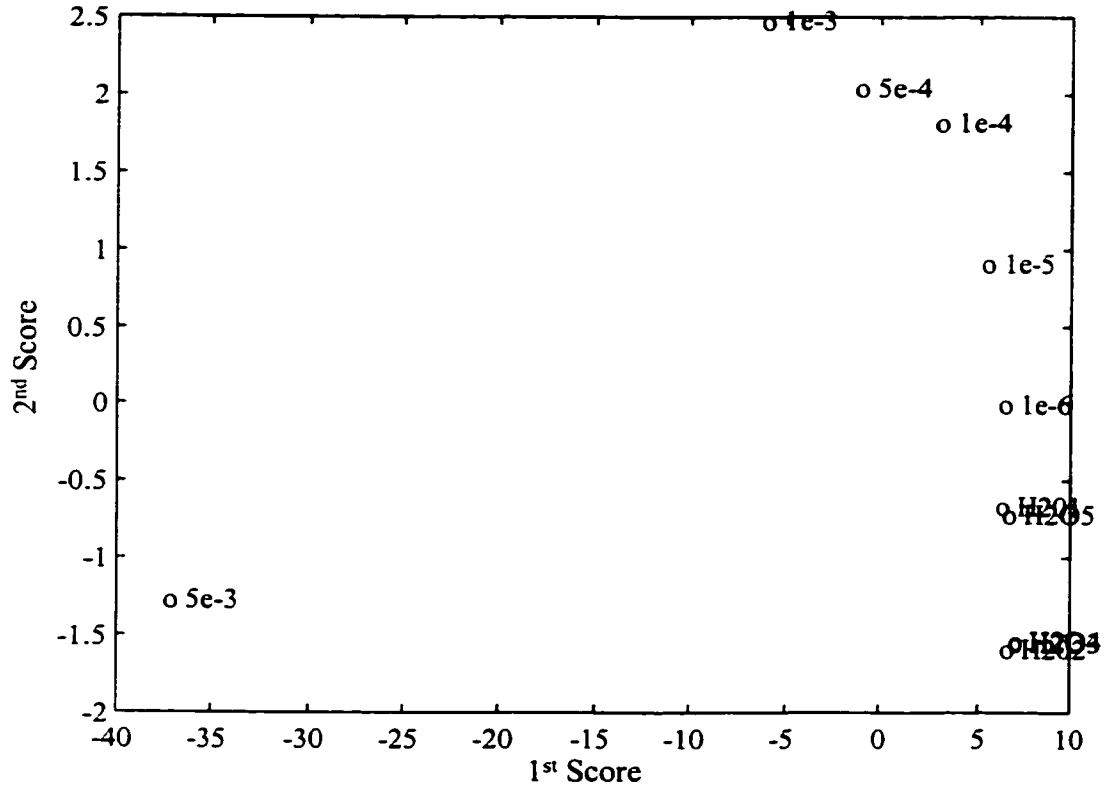

Figure 4.10 First two sample scores obtained from PCA of the mean-centered difference spectra of the absorption sample data set.

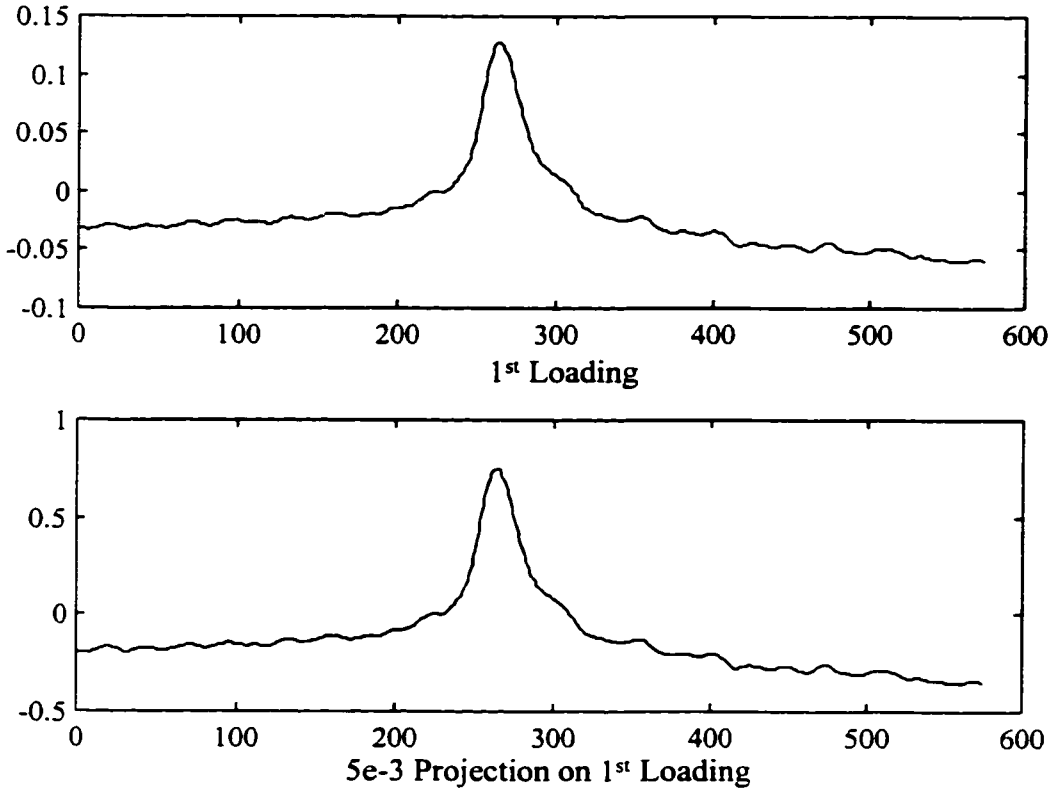

Figure 4.11 Projection of the highest concentration absorption sample onto the first PCA variable loading.

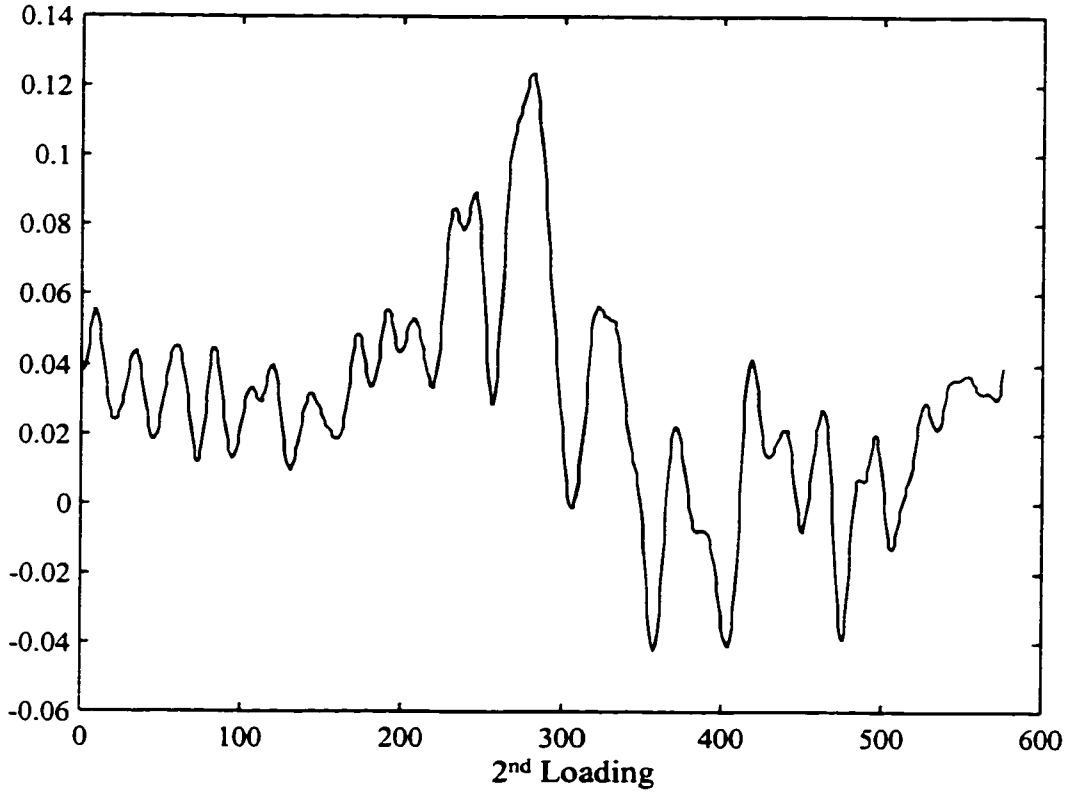

Figure 4.12 Second PCA loading, that correlates with high-frequency Reflectivity changes.

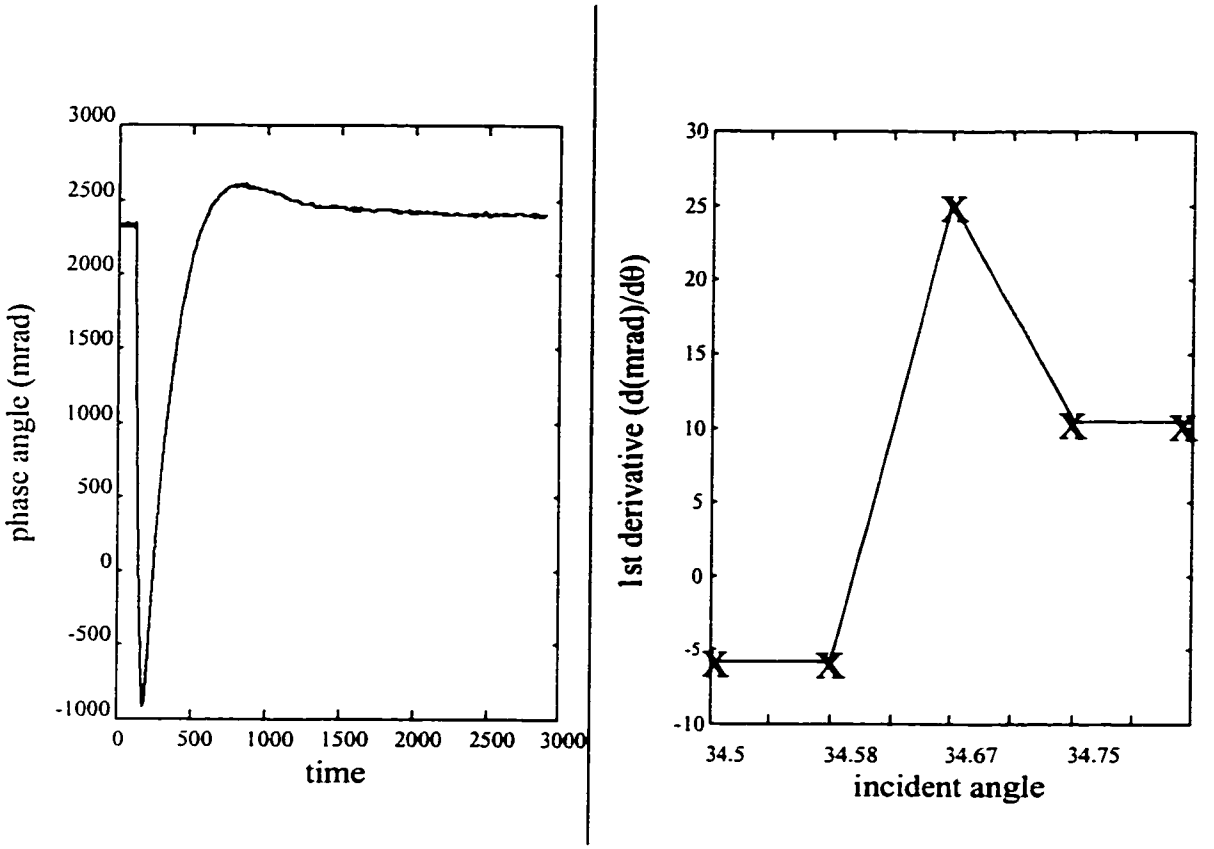

Figure 4.13 Proof of principle GLRS phase measurement data.

Chapter 5

Characterization of Nanoparticles

5.1 Introduction

This chapter presents both theoretical and experimental results demonstrating that GLRS can provide information about the concentration and average size of particles of nanometer dimensions distributed in liquid phase media. To model the GLRS response for very small particles, we chose to look at various volume fractions of dendrimer molecules suspended in water. Dendrimers were chosen because they have an approximately spherical symmetry and are available in nanometer-scale diameters. Dendrimers are polymers that grow radially outward from a common "seed" or core element. They are produced with various functional groups, but we used the Starburst© brand of polyamidoamine (PAMAM) dendrimers produced by Dendritech, Inc. The PAMAM dendrimers are constructed by repeatedly attaching amine/amide structural units to the original ethylenediamine (EDA) core.[40]

---

[40] for general information regarding the structure, production, and potential uses of dendrimers visit: **http:/www.mmi.org/mmi/dendritech**

As discussed in the previous chapter, a multivariate approach should be used to take full advantage of all of the reflectivity information in the wavelength region around the critical point. However, recent advances in the GLRS theory have shown that it should be possible to extract sample optical properties by fitting the corrected data to a theoretically ideal reflection spectrum. Because of the multitude of variables that contribute to the reflection spectrum over a broad wavelength range, this approach should work best in the region very close to the critical point. Once the best theoretical fits in this region have been determined, the fitting parameters can be used to calculate the optical properties of interest. In particular, we were interested in determining the limits of the GLRS with respect to particle size determination, since theoretically the technique should perform very well in the very small particle (i.e. Rayleigh scattering) light scattering regime. This is because GLRS reflectivity differences at the critical point, and also very close to it on the evanescent side, are caused by a loss of coherence of the evanescent wave as it penetrates the solution. This coherence loss may be due to absorption or by non-forward scattering. Therefore, GLRS is essentially an optical coherence measurement.

In order to relate changes in $Re\varepsilon_2(\omega)$ and $Im\varepsilon_2(\omega)$ with the properties of particles distributed in a sample medium we can use the following expression:

$$\varepsilon_2 \cong \varepsilon_m + 4\pi\left(\frac{c}{\omega}\right)^2 \sum_{\alpha} N_\alpha A_\alpha(0) \qquad (1)$$

where ε_m is the permittivity of the suspending medium, N_α is the mean concentration of particles of type α, and $A_\alpha(0)$ is the complex forward scattering amplitude of those particles. This approximation holds in the case of not-very-high volume concentrations of particles and not very large optical contrasts between the particles and the suspending medium. For particles with dimensions less than the critical wavelength we can express $A_\alpha(0)$ using the Rayleigh-Gans approximation that states:[41]

$$\mathrm{Re}\left(4\pi\left(\frac{c}{\omega}\right)^2\sum_\alpha N_\alpha A_\alpha(0)\right)=3\rho\frac{\varepsilon_p-\varepsilon_m}{\varepsilon_p+2\varepsilon_m}\varepsilon_m \qquad (2)$$

$$\mathrm{Im}_{eff}\left(4\pi\left(\frac{c}{\omega}\right)^2\frac{1}{\sqrt{\varepsilon_m}}\sum_\alpha N_\alpha A_\alpha(0)\right)=\frac{3}{8}\rho\left(\frac{\omega}{c}\right)\overline{R}(\varepsilon_m)^{3/2}(\varepsilon_p-\varepsilon_m)^2 \qquad (3)$$

where $\overline{R}$ is the mean particle radius, ρ is the volume fraction of the particles and ε_p is their permittivity. This value of ε_p is considered to be an averaged dendrimer characteristic parameter. We have supposed in equations (2) and (3) that we can disregard the imaginary component of ε_p and ε_m; that is, we assume that the solvent and the particles do not have an appreciable absorption in the considered light frequency range. Thus, by fitting equations (47) and (58) from the Theory section to the position and intensity of the critical point region of the reflection spectra, we can determine the real and *effective* imaginary dielectric functions described above. Then, using the known

---

[41] Newton, R. *Scattering Theory of Waves and Particles*, McGraw-Hill, New York, **1966**.

values for the dielectric constants of the particle material and the solvent, the volume fraction is calculated first, and this value is then used to help calculate the particle radius.

5.2 Description of the Experiment

The flow channel discussed in the Experimental section was used along with the 503.6 nanometer period grating at an incident angle of 9.4° to collect reflection spectra of the dendrimers according to an averaging procedure described below.

Five "generations" or sizes of Starburst© PAMAM dendrimers in water were purchased from Dendritech and diluted to concentrations ranging from 2% to 10% by weight in 2% increments, resulting in a set of twenty-five dendrimer samples. The concentrations of these samples were confirmed by measuring their refractive indices to within 0.0001 at 22° C using an Abbe refractometer. However, rheological studies on these molecules show that the density of the lowest generations increases significantly with increasing size, before leveling off somewhat at generation 5.[42] Since these samples were all injected at equal weight fractions, this means that the bigger sizes are actually present at a lower volume fraction than the smaller particles. Table 5.1 shows the volume fraction calculated from this information for each sample, along with the refractive index

of each dendrimer and the effective sizes and molecular weights of the dendrimers used in this study. There are question marks on the G7 series volume fractions, because density information on that size is not available at this time; however, the trend from the rheological studies indicates that the dendrimer densities level off above the G3 series.

5.3 Discussion of the Results

Figure 5.1 shows the final set of spectra from which the dendrimer sizes and volume fractions were calculated. Each of the twenty-five dendrimer samples was injected five times, resulting in a complete sample set of 125 injections, and the reflection spectrum corresponding to the peak of each injection was taken and averaged with the other four such peaks for each sample, resulting in a final set of twenty-five spectra. The spectra are organized as follows: sample numbers 1 to 5 correspond to the G0, G1, G3, G5, and G7 sizes within the 10% w/w subset, 6 to 10 are the equivalent sizes in the 8% w/w subset, and the other groups of five are the 6%, 4%, and 2% w/w subsets, respectively. These smoothed (see below) and averaged spectra were fitted to theoretically ideal reflection curves using a MATLAB function that constructed a matrix of ideal responses from equations (47) and (58) of the Theory section and then compared

---

[42] Uppuluri, S.; Keinath, S. E.; Tomalia, D. A.; Dvornic, P. R. *Macromolecules*, **1998**, vol. 31, no. 14, pp. 4498-4509.

each of these with a particular averaged spectrum. The δ and $Im\varepsilon_{eff}$ values of the ideal spectrum that had the lowest sum-of-square residuals with respect to the averaged spectrum were then used to calculate the volume fraction and particle radius of the dendrimers from equations (2) and (3), respectively.

The equations describing the GLRS response are only predicted to hold in the threshold region where the value of δ is near zero, and thus where $Im\varepsilon_{eff}$ of the sample becomes significant relative to $Re\varepsilon$. Therefore, a suitable spectral "window" had to be determined over which to perform the fits. Upon looking at synthetic, theoretically ideal spectra with the same volume fraction and size parameters as those expected in this experiment (figure 5.2), it became obvious that changes in $Im\varepsilon_{eff}$ dominate the spectral response only on the evanescent side of the critical wavelength, and that differences in slope between spectra with increasing $Im\varepsilon_{eff}$ became minimal further than 6 nanometers from the critical wavelength. Therefore, the first 6 nanometers to the high wavelength side of each sample's critical wavelength was chosen over which to perform the fits with theory. Given the spectral data density of 0.1 nanometers per pixel, this range provided 60 data points per spectrum over which to calculate the fit residuals.

While the averaged spectra exhibited very little noise, as demonstrated by the average relative standard deviation of 0.2% per pixel within a set of five water spectra taken at a rate of one per hour (their collection was evenly distributed throughout the course of the entire dendrimer data collection procedure), imperfections in the GLRS grating contributed significant structure to these reflection spectra (figure 5.3).

Note that the noise level of this data is an order of magnitude larger than that shown in sections 4.2 and 4.3. This is because this experiment was conducted over a much longer period of time, so that random (esp. temperature-dependent) fluctuations between two spectra collected at widely different times increased dramatically. The experiments of sections 4.2 and 4.3 took less than an hour each to sample the complete data sets, while the present set of 125 samples required ~ 10 hours to perform all of the injections. Therefore, this 0.2% noise level is intended to show the long-term stability of the system, and does not represent the variance for a single sample. For all of those individual sample spectra, composed of the mean of five injections taken sequentially (i.e over a time of ~ 10 minutes), the noise level approximated that of the data in sections 4.2 and 4.3. Finally, remember that the theory allows us to calculate the concentration and size of the particle absolutely, without relying on a reference. This means that fluctuations such as temperature will have no effect on the precision of the calculated values, unless such fluctuations occur on the time scale of the five sequential injections.

The high-frequency grating structure affected the performance of the iterative fitting function by causing wide fluctuations in the sum-of-squares residual between successive iterations of the fitting routine, so that often the routine stopped after finding only a local residual minimum. Therefore, in order that the fitting function should more consistently approach the sum-of-squares minimum residual, a Savitsky-Golay 7 point, 3^{rd} order polynomial smoothing filter was applied to each sample spectrum. This served to reduce the high-frequency variations in intensity. Fits performed on five such water

spectra (figure 5.4), one taken between every twenty-fifth sample injection, exhibited fitting errors with a standard deviation of 0.00036 delta and 0.00034 $Im\varepsilon_{eff}$; these are equivalent to 95% confidence intervals of 0.045% volume fraction concentration and 0.36 nanometers particle radius. Thus the experiment exhibits extremely good precision with respect to these quantities when samples are composed of the average of five individual spectra.

In addition to the structure imparted to the spectra by the imperfections and square profile of the grating, the grating also exhibits wavelength-dependent changes in reflectivity. Furthermore, due to limits of detector resolution, incident beam collimation, and residual scattering from dust particles, substrate imperfections, and dissolved gases and turbulence in the water carrier solvent, the critical wavelength will not exhibit the ideal behavior shown by theoretical reflectivity curves generated by equations (47) and (58) of the Theory section. The combination of these effects means that a transparent sample will exhibit a non-zero $Im\varepsilon_{eff}$ when fitted to an ideal response. This value constitutes a baseline offset that must be applied to the fit results of scattering or absorbing samples before dielectric properties can be deduced from them. Furthermore, this offset will be different for samples with different critical wavelengths, and so it must be determined at every critical wavelength in the sample set. This correction was performed by recording the spectra of three aqueous sodium chloride solutions that spanned the range of critical wavelengths in this experiment (figure 5.5). When compared with pure water, these solutions showed a significant change in apparent $Im\varepsilon_{eff}$ value

when fitted, due to their differing critical wavelengths. However, they were extremely consistent within themselves, showing a difference in fitted $Im\varepsilon_{eff}$ value of only 0.0001 over the roughly 4 nanometer span of critical wavelengths in this experiment. Thus, a single baseline offset of 0.0053 was applied to all of the samples when calculating their properties. Figure 5.6 shows an example of these fits done on the G0 and G7 dendrimer samples within the 10%w/w concentration subset. Note that they had different critical wavelengths, and so they are plotted on an axis of "relative pixel number", with zero being the pixel corresponding to each spectrum's critical wavelength.

Table 5.2 summarizes the calculated values of particle radius and volume fraction concentration for each of the twenty-five dendrimer samples tested, and Table 5.3 lists the residuals for each sample with respect to its reference size. The samples are arranged into the concentration subsets described in the Experimental section. Four significant figures are retained in the calculated values since the experimental quantities required in the calculations (sine of incident angle, refractive index, grating period, critical wavelength, and mean of "baseline" $Im\varepsilon_{eff}$) are known to that degree of precision.

From this table, it can be seen that the samples were diluted somewhat during their passage through the channel to the detection interface, because the fitted volume fractions within each concentration subset are approximately one-half of the original injected concentrations. Furthermore, within each concentration subset, the larger dendrimer sizes were diluted more than the smaller sizes. This is due to differences in the rates of diffusion between the particle sizes: larger particles tend to clump in the middle

of the channel, and so they are less concentrated at the grating/channel interface than an equal volume fraction of smaller-sized particles.

When comparing the particle size residuals of the samples, it is clear that the larger particles at higher concentrations yield the closest agreement to the reference values. This results from the increase in sample scattering with increasing volume fraction: the number of scatterers contributing to the GLRS response in the highest concentration subset in this experiment is nearly an order of magnitude greater than that for the lowest concentration subset. Refer to figure 5.7 to see how the volume fraction and calculated particle size vary within the five concentration subsets. As the sample volume fraction decreases, errors in measurement of $Im\varepsilon_{eff}$ value lead to relatively larger deviations in the particle size calculated from equation (3). The fitted size of the G3 dendrimer in the lowest volume fraction concentration subset does not track exactly with the rest of the size trends. This is because two of the five spectra that represented this sample contained cosmic rays within the 60-pixel fitting region. These intense and narrow intensity changes could not be adequately removed, so only the three undisturbed spectra were averaged and used in the fitting routine. The lower precision of this sample could thus account for its slight deviation from the rest of results of that particular data subset.

Other factors contributing to the better results for larger particles include the fact that the smaller dendrimers become increasingly aspheric, with long: short radii ratios approaching 2 to 1.[43] Also, note from table 5.1 that the molecular weights for the samples increase several orders of magnitude from the G0 subset to the G7 subset. These two factors describe the smaller dendrimers as loosely packed almost amorphous polymers, while the larger dendrimer more closely approximate a solid sphere.

The results demonstrate that it is possible to distinguish size differences in particles distributed in water whose radii varied by less than 1 nm. More generally, we have demonstrated that the analysis of GLRS experimental data allows us to get substantive information about structural characteristics of non-uniformities in a strongly scattering medium. This can be done even in the case where the characteristic length of these non-uniformities is substantially less than the scattered light wavelength, and can in fact be on the order of molecular dimensions Realistic possibilities exist for measuring such processes as cluster formation and polymerization reactions, crystal formation, and surface and bulk phase transitions.

This impressive size resolution has implications beyond straightforward particle size determination. We envision GLRS as a general chemical sensing technique that has many applications in areas occupied at the present by more complicated methods. For

---

[43] see again: Uppuluri, S.; Keinath, S. E.; Tomalia, D. A.; Dvornic, P. R. *Macromolecules*, **1998**, vol. 31, no. 14, pp. 4498-4509.

example, bioanalytical assay methods that rely on conformational changes in proteins upon binding to some target analyte could take advantage of the fine size resolution of GLRS to directly measure changes in protein structure.

Furthermore, the resolution demonstrated in this work could be improved upon by developing higher quality diffraction gratings with more regular periodicity, and by conducting measurements in the near UV frequency interval, where optical contrasts between organic materials and water (or air) increase dramatically.

Finally, the sensitivity of this method would greatly improve in certain types of gas phase sample matrices such as aerosols, where the optical contrast between the particles and the solvent (air) would be much greater than for the dendrimer samples presented here. This means that each scattering event occurring at these points of high dielectric contrast will result in much more incoherent scattering, and thus a stronger GLRS signal change, than would occur for particles of a similar size in a liquid matrix. Furthermore, the pathlength of such measurements would be far greater than in condensed phase matrices, which would compensate for the diminished number of scattering events per volume occurring in gas phase systems.

Table 5.1 Properties of the dendrimer samples used in this experiment.

Dendrimer Sample Information

Size Series	Radius	Molecular Weight	Refractive Index Water @ 25°C = 1.3325
G0 (stock 21.72% w/w)			
2% w/w	7.5A	517	1.3363
4% w/w			1.3400
6% w/w			1.3436
8% w/w			1.3477
10% w/w			1.3520
G1 (stock 23.67% w/w)			
2% w/w	11A	1430	1.3363
4% w/w			1.3403
6% w/w			1.3436
8% w/w			1.3473
10% w/w			1.3515
G3 (stock 32.21% w/w)			
2% w/w	18A	6909	1.3363
4% w/w			1.3402
6% w/w			1.3439
8% w/w			1.3479
10% w/w			1.3518
G5 (stock 14.89% w/w)			
2% w/w	27A	28826	1.3360
4% w/w			1.4303
6% w/w			1.3442
8% w/w			1.3477
10% w/w			1.3520
G7 (stock 11.6% w/w)			
2% w/w	40.5A	116493	1.3360
4% w/w			1.3399
6% w/w			1.3439
8% w/w			1.3476
10% w/w			1.3518

Table 5.2 Calculated particle size (radius) and volume fraction of the 5 dendrimer concentration subsets, arranged from smallest to largest size within each subset.

Fitted v/v & size of Dendrimer Samples

		Subset 1			
size	0	10.9406	23.4495	19.1139	25.4852
v/v	0.0086	0.0075	0.0069	0.0064	0.0064
		Subset 2			
size	9.8533	14.4908	11.4955	18.2533	28.6666
v/v	0.0258	0.0263	0.0258	0.0231	0.0220
		Subset 3			
size	17.0081	18.7443	20.5423	22.6775	35.4219
v/v	0.0306	0.0295	0.0290	0.0301	0.0263
		Subset 4			
size	11.2751	16.3423	18.2903	26.7570	40.7171
v/v	0.0424	0.0397	0.0403	0.0371	0.0371
		Subset 5			
size	4.9495	16.5852	22.4823	27.8247	40.6659
v/v	0.0538	0.0505	0.0489	0.0473	0.0451

Table 5.3 Particle radius residuals for each sample versus the reference values, arranged from smallest to largest size within each concentration subset.

Sample Particle Radius Residuals

Subset 1	-7.5000	-0.0594	5.4495	-7.8861	-15.0148	mean =	7.18195
Subset 2	2.3533	3.4908	-6.5045	-8.7467	-11.8334	mean =	6.5857
Subset 3	9.5081	7.7443	2.5423	-4.3225	-5.0781	mean =	5.8391
Subset 4	3.7751	5.3423	0.2903	-0.2430	0.2171	mean =	1.9736
Subset 5	-2.5505	5.5852	4.4823	0.8247	0.1659	mean =	2.7217

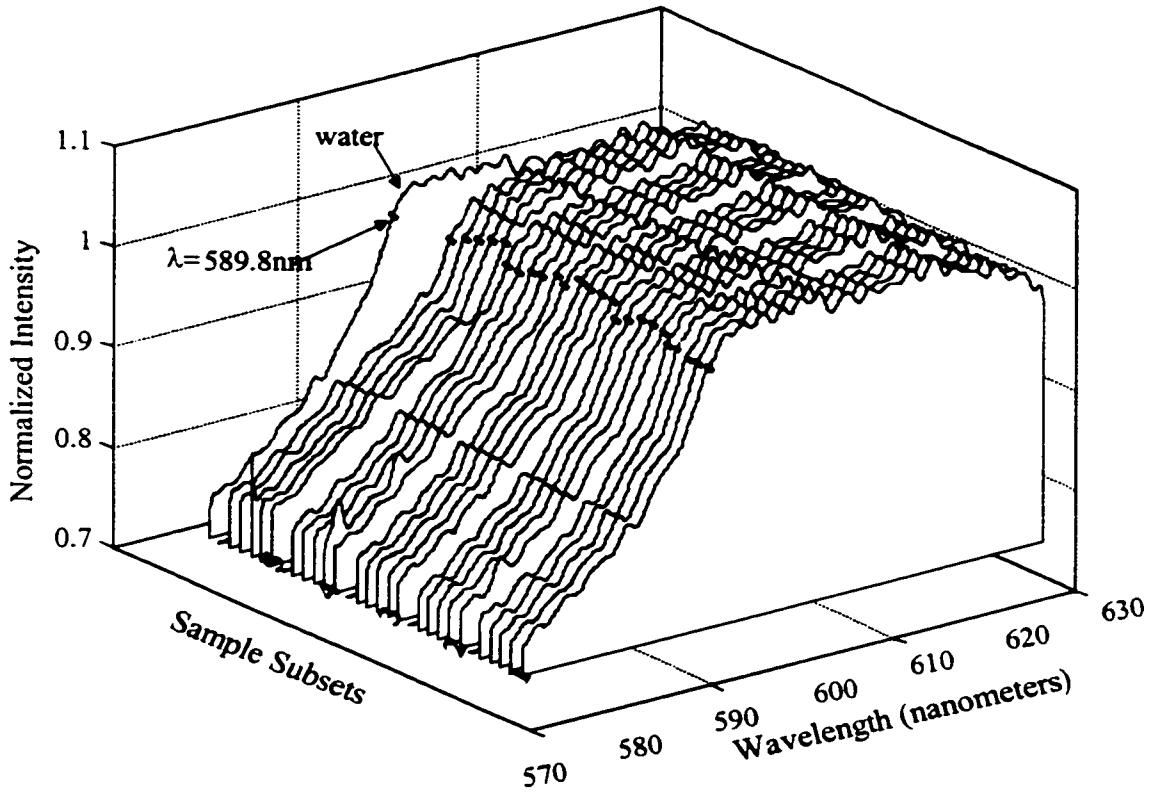

Figure 5.1 Complete set of dendrimer spectra, with water included as a reference. Black dashes near the top of each spectrum's transition slope indicate the calculated critical wavelengths based on the fit of the data to theory.

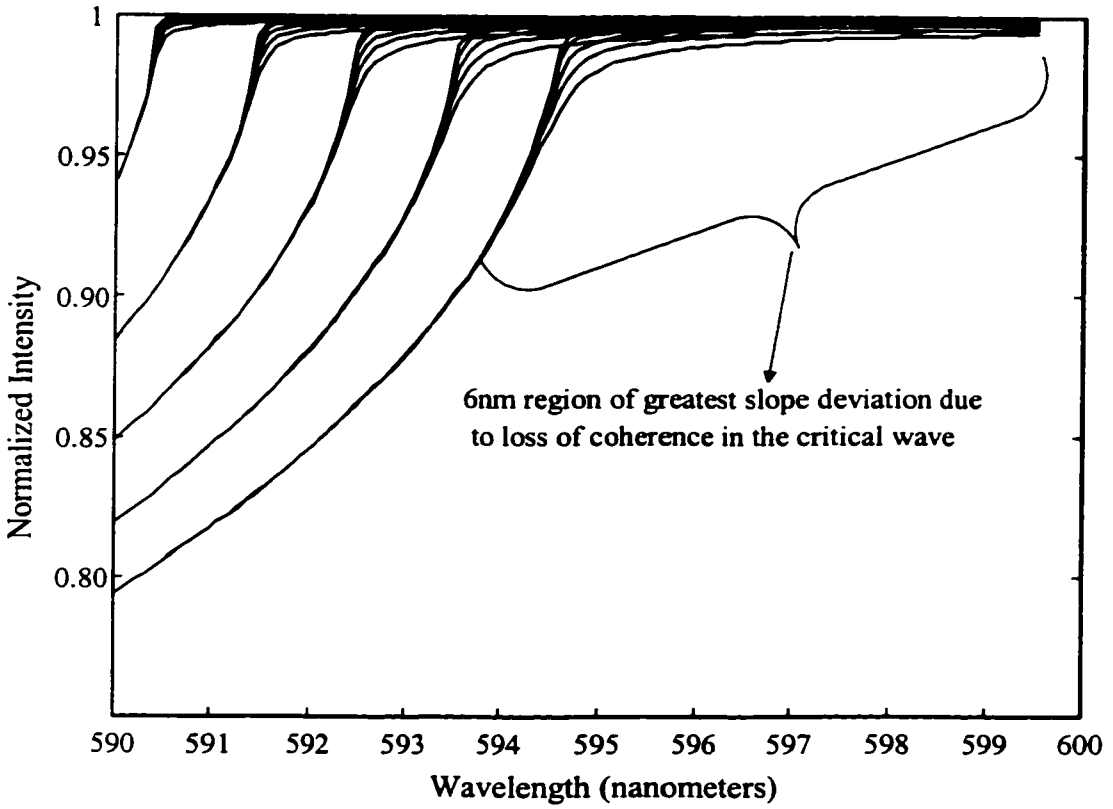

Figure 5.2 Set of 25 hypothetical spectra approximating the properties of the dendrimer samples. These show that the best region to fit is the first 6nm to the long wavelength side of the critical wavelength.

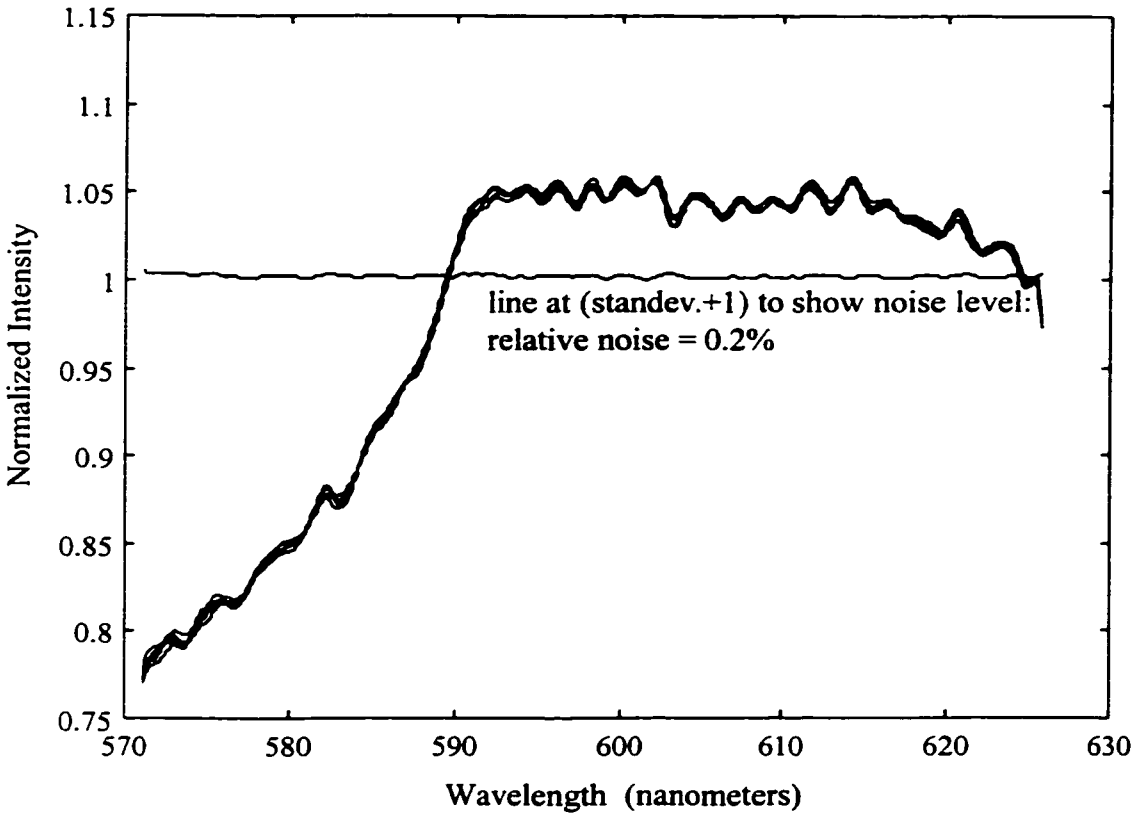

Figure 5.3 Five water spectra, taken at regular (approx. 1 hour) intervals over the course of the experiment to show the stability of the measurement.

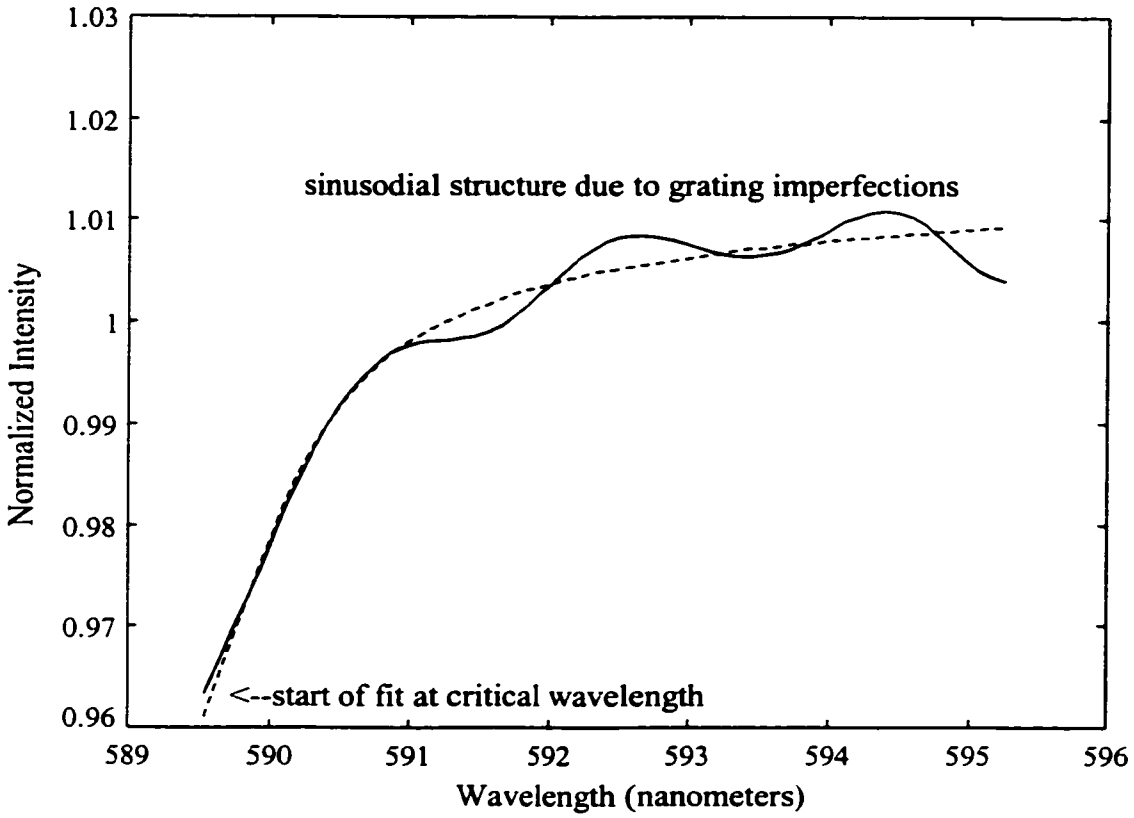

Figure 5.4 Fit of water spectrum to ideal GLRS response, showing only the region of interest comprising the first ~6nm (60 pixels) to the evanescent side of the critical wavelength.

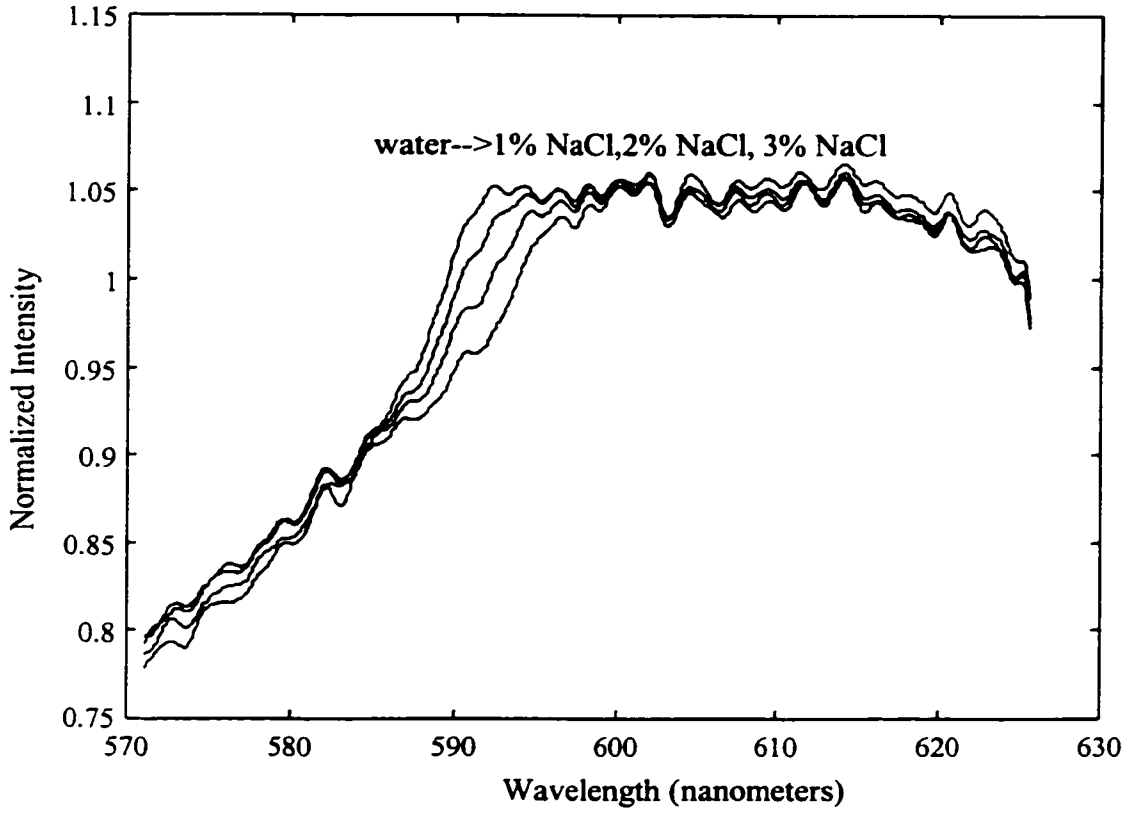

Figure 5.5 Sequence of salt standards used to establish the "baseline" GLRS response over the range of critical wavelengths encountered in these experiments.

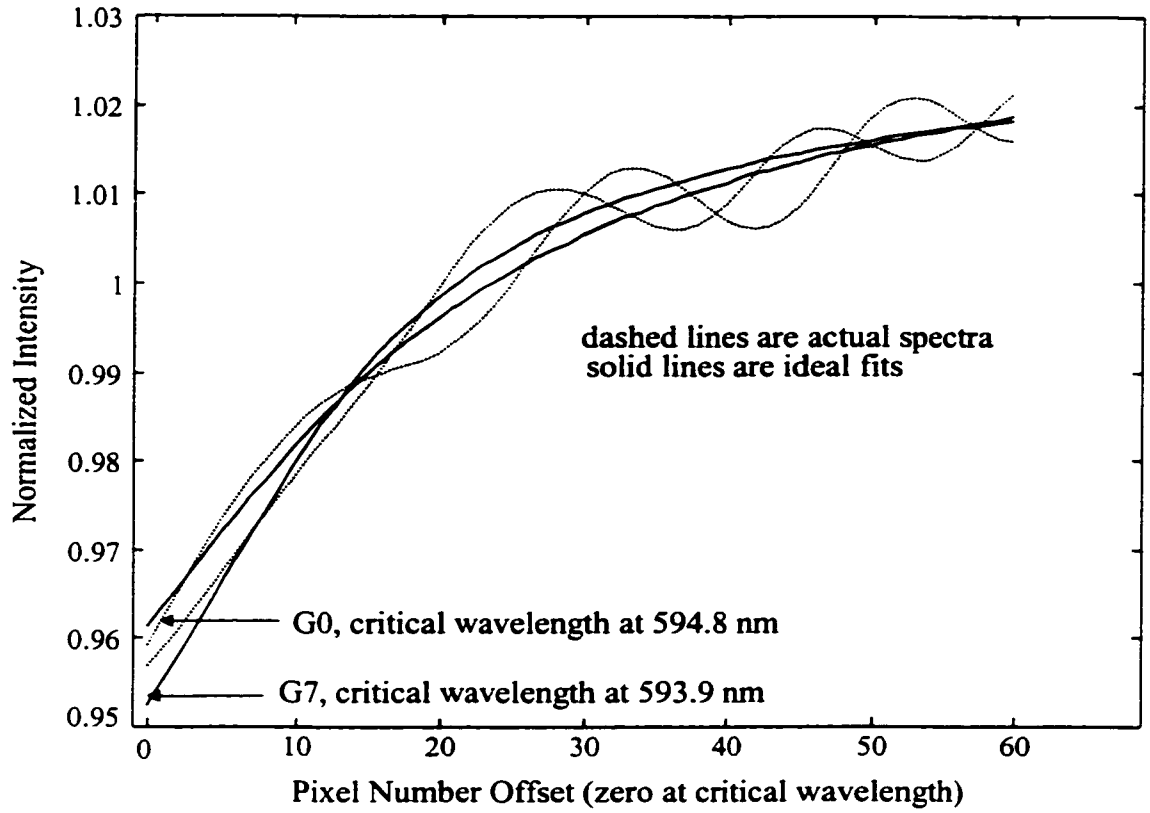

Figure 5.6 Comparison of ~10% w/w G0 and G7 dendrimer sample spectra fits. The spectra are placed on a common axis, with the origin at the fitted critical wavelengths.

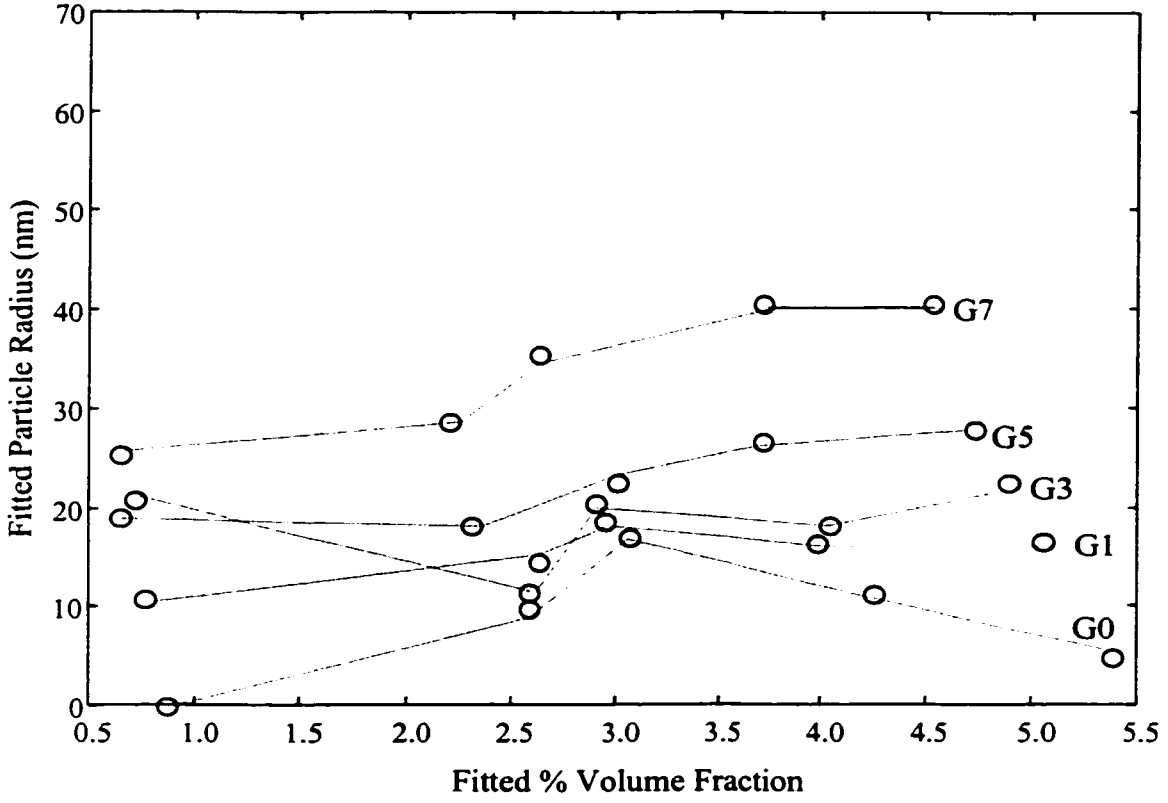

Figure 5.7 Trends of the fitted parameters for each dendrimer size.

Chapter 6

GLRS as a Chromatographic Detector

6.1 Introduction

GLRS should perform well as a chromatographic detector because of its ability to quantitate all changes in the optical properties of a sample. Thus, depending on the wavelength range selected, the method combines the features of currently available refractive index and UV absorbance liquid chromatographic detectors. As described in the Theory section, the grating interface is extremely simple and durable, and can be fashioned *into* – as opposed to on the end of - a liquid chromatograph column regardless of the materials out of which the column is made.

The implementation of GLRS as a liquid chromatographic detector resulted from the work done on constructing an improved sampling interface using micro-fabrication technology, as described in the Experimental section. Parallel with this development, Paul Vahey in Dr. Robert Synovec's research group at the University of Washington had initiated a characterization of the chromatographic properties of these same micron-scale PDMS flow channels. Since GLRS had already been interfaced to such a system, there was a natural progression from the using the technology merely as a sampling interface to

performing analyte separations with it. The only required steps were to reduce the size of the channels and the sampling volume for better resolution of elution peaks. Once this was done, GLRS proved capable not only of detecting separated analytes, but also of assigning those peaks to specific chemical species based upon the qualitative structure of the GLRS reflection spectra. Finally, the purpose of this chapter is to characterize the performance of GLRS as a detector, and not to quantify the chromatographic performance of the PDMS micro-channel. Therefore, even though the characteristics of the chromatographic system will be summarized in general, its chromatographic performance will not be analyzed beyond stating the fact that it was adequate for separating all of the analytes of a complex injection sample.

6.2 Summary of Experimental Apparatus

As mentioned above, the same flow system as used for the other analyte characterization work was employed here, with minor changes. All of these changes were made to improve the chromatographic performance of the system. Figure 6.1 shows a schematic of the resulting apparatus. The dimensions of the flow channel were reduced to 100 microns high by 10 microns deep, while the width of the GLRS interrogation beam was reduced from 1 millimeter to 150 microns. This resulted in a sampling volume of 150x100x10 microns = 1.5×10^{-13} cubic meters or 150 picoliters. Therefore, this system is extremely efficient with respect to sample consumption. Furthermore, the ability to

conduct a reflection-based optical measurement in such volumes demonstrates the versatility of GLRS as a sensing methodology.

The sample injections were performed using a crossed-flow, on-column design, as shown is figure 6.2. Samples were injected on the micro-column by closing the carrier stream output and simultaneously opening the injection output to the force of the pumps for a period long enough to fill the channel length between the injection input and output with analyte. Then the flows were re-directed, such that chromatographic separation of the components of that injection occurred over the 3 centimeter channel length between the injection site and the detection volume.

Due to the fragility of the extremely small channels, some difficulty was encountered in generating carrier flow rates low enough to prevent leaks from occurring at the channel connections. Since the resulting flow rates were below the calibration range of the micro-flow HPLC pump gauges, only an estimate can be given of the actual flow rate. For example, upon inspection of the data in figure 6.3, it is seen that a separated sample component took ~15 seconds to reach the GLRS detection interface 3 centimeters away from the injection site: this results in an estimated flow rate of:

$$\frac{100 microns \times 10 microns \times 3x10^{4} microns}{0.25 \min.} = 0.12 \, microliters/\min.$$

The separated components in figure 6.3 are from an injected sample of 10^{-4}M bromocresol green in an aqueous buffer of 0.125M phosphate. The extra components observed in the data are a result of the fact that the dye was purchased as an 85% pure

crystalline solution. Therefore, 15% of the sample is unknown. However, for purposes of characterizing the performance of GLRS as a chromatographic detector, these extra features merely provide more information to interpret.

The GLRS parameters were chosen to place the critical wavelength between 630 and 640 nanometers in this water-based carrier stream. This wavelength was chosen to overlap with the absorbance band of bromocresol green in neutral solution (600 to 650 nanometers, depending on pH). The GLRS grating used for this experiment had a period of 1100 nanometers. This meant that the resolution of this grating was:

$$635nm \div \left(\frac{909 grooves}{mm} \times 0.15mm \right) = 4.7nm$$

(Note that this is NOT the resolution of the detection optics: as described in the Experimental chapter, that is ~0.2 nanometers). This 4.7 nanometer resolution implies that even moderate changes in the position and form of the reflection spectrum at critical wavelength will not be immediately visible in the raw data, since the most prominent features of these changes will occur over a range of at most a few nanometers with the current sample.

6.3 Generation of the 3-Dimensional Chromatogram

As shown in figure 6.3, the buffered dye solution was separated into (at least) 4 different components, corresponding to each of the bands that appear along the wavelength axis of the chromatogram. The 3-dimensional data matrix is shown looking

straight down on the time-wavelength plane in order to show completely the qualitative features of the data. Due to the low critical point resolution described above, several data processing steps were required to generate this information. First, all of the 300 spectra collected over the span of the injection run were normalized to their individual mean intensities, in order to correct for random fluctuations in the overall reflection intensity. These spectra were then smoothed with an 11 point Savitsky-Golay polynomial fitting algorithm to reduce pixel-to-pixel intensity variations. This smooth serves to simulate signal averaging of the spectra. No actual averaging could be done due to the real-time nature of the data. Next, the matrix of spectra was smoothed along the time axis to reduce the effect of flow system fluctuations that occurred faster than the ~1/sec. sampling rate. These fluctuations caused a "grassy" appearance of the chromatogram along the time axis that could not be eliminated via the intensity normalization procedure described above, since they occurred independently of fluctuations in the optical train. Finally, to "magnify" visually the appearance of eluting analyte components, the mean of the first five corrected spectra in the data matrix (i.e. the "baseline" response) was subtracted from each of the spectra in the matrix. This resulted in the difference signal of figure 6.3, in which bluer colors indicate a negative differential and redder colors indicate a positive differential with respect to the baseline water response. A look ahead to figure 6.7 reveals the magnitude of this resulting difference signal. In this figure, the wavelength-dependent difference spectra corresponding to the tops of the two most prominent bands in the chromatogram are shown relative to the baseline response. The magnitudes of the most

intense features in these spectra are only twenty times the standard deviation of the intensity (.001). This means the data processing efforts have improved the signal-to-noise ratio to 20, given data with a signal-to-noise ratio of at most 3 (since it is generally accepted that a signal cannot be visually separated from its noise at this level).[44]

One surprising result of this procedure is the appearance of an interference pattern in the spectra on the transmitted side of the critical wavelength. However, the fringe pattern is a fortunate occurrence, because it yields more quantitative and qualitative information in the difference spectra. Because of the complexity of the detector interface, and the number of optical variables involved, the exact cause of these fringes cannot be determined without further experiments designed specifically to iterate through all the possible sources of fringes. However, section 6.5 will discuss these various interface components and optical variables in order to put forward some potential mechanisms through which the fringes could be generated.

6.4 Quantitative Analysis of the Chromatogram

To generate a time-dependent chromatogram with the highest possible signal-to-noise ratio, the sum of the squares of each of the pixels in the difference spectra were taken to form a single point determination of the GLRS response at each point in time.

---

[44] Skoog, D. A.; Leary, J. J. *Principles of Instrumental Analysis*, 4th edition, Saunders College Publishing, Fort Worth, 1992, p. 47.

Figure 6.4 shows the result of this operation. This plot makes the presence of four analyte components clear. There are two large, sharp peaks corresponding to each of the pure components in the solution, and there are two much smaller peaks revealing the presence of the 15% unknown constituents in the stock dye material. Because the flow system had not been stabilized enough to perform reproducible injections, no calibration set could be formed from which to determine the limits of detection for GLRS with respect to absorbance (bromocresol green concentration) or refractive index (phosphate concentration). However, it is apparent from the areas and sharpness of the two main peaks that concentrations of perhaps an order of magnitude less than these could be quantitated.

To determine at what wavelengths the quantitative information is coming from in the reflection spectra, this sum of squared differences procedure was performed along the time axis. Figure 6.5 reveals that, as expected, most of the quantitative ability of the spectra results from sharp changes in the critical condition in different sample types. The fringe pattern region also exhibits a good deal of sensitivity, although this declines as the critical wavelength is approached.

The greatest detractor to sensitivity in this particular application was the low resolution of the detection grating, which was a direct consequence of the small incident beam width necessary to achieve adequate time resolution of the analyte components. This could be greatly improved by using a longer separation column to generate better separation of the components, so that a wider detection volume could be used. In

addition, since GLRS resolution is directly proportional to the number of grating lines involved in generation of the critical point, a grating with a smaller period could be used in conjunction with a wider incident beam. A finer grating would also make the experimental setup easier by allowing the use of smaller incident angles, so that a more efficient optical train could be constructed. For example, using a 500 nanometer period grating with a 700 micron beam width would improve the resolution by a factor of ten, with a corresponding increase in the signal-to-noise ratio of the data. The use of the 1100 nanometer grating for these experiments was dictated by the fact that it had been deposited on the only available substrate that was appropriate for bonding to the PDMS micro-channel layer.

6.5 Qualitative Analysis of the Chromatogram

Perhaps the most prominent feature of the chromatogram, aside from the sheer *multitude* of features, is the fringe pattern formation highlighted in the square box of figure 6.3. As stated in section 6.3 above, there are several possible mechanisms through which these fringes could be generated. A few of these will be summarized below. However, due to the multitude of potential contributing factors, these explanations should not be considered as self-contained or mutually exclusive with respect to one another. The ultimate solution to this problem may indeed result from a combination of elements of each of the scenarios presented here.

First of all, one factor which makes this set of experiments different from other GLRS experiments is the presence of a thin dielectric coating over the grating. This coating, certainly less than 1 micron thick, and perhaps only a few molecular layers thick, was laid down to provide better adherence of the PDMS substrate to the chrome and glass interface. Since it consists of silane molecules (allyltrimethoxysilane), it certainly has a higher refractive index than the aqueous samples used in these experiments. Therefore, it could act as a thin film waveguide for any light transmitted across the grating interface that matches the coupling conditions for the waveguide. This could explain why the fringes disappear above a certain wavelength in the chromatogram of figure 6.3. Waves entering this waveguide would reflect back and forth between grating / film interface and the film / sample interface (similar to a Fabry-Perot cavity) and could generate an interference pattern that would be observed in the zeroth diffraction order arising from the grating. The exact waveguiding conditions would depend upon the thickness of the layer, the incident angle of the source light, the width and degree of collimation of the beam, and the period of the grating. Therefore, the mere presence of this layer is not necessarily sufficient to generate a fringe pattern. This required combination of parameters would explain why the fringe pattern was not observed in earlier experiments conducted with a similar micro-channel sampling system. One important consequence of this mechanism, if it is eventually proven to be responsible for the fringe pattern, is that it means the stationary phase of a micro- liquid chromatographic column could be used as an optical sensing interface. Therefore, it is important to pursue this possibility further.

Finally, the fringes may result from the fact that every wavelength to the blue side of the critical point (~635 nanometers) in the critical transmitted diffraction order exists as a traveling wave in the sampling volume. This interpretation is similar in mechanism to the waveguide scenario discussed above. With the back wall of the micro-channel only ten microns away, those waves do not have to travel very far (roughly 30 wavelengths) in order to reflect from the channel wall and re-combine with the zeroth order grating reflection. Upon re-combining, constructive and destructive interference will occur depending on the relative phases of the zeroth order wavelengths and the reflected first order wavelengths. Furthermore, the amount of wavelength-dependent overlap will decrease sharply for wavelengths near the critical point, since these are transmitted at near grazing angles relative to the grating / sample interface. These must travel many wavelengths in a lateral direction before reflecting off the back wall of the channel, and thus will fall outside of the beam diameter of the zeroth order reflection, so that no interference overlap will occur at these wavelengths. In contrast, those wavelengths farther from the critical wavelength will travel at much more acute angles, so that more of them will be available for overlap with the zeroth order; therefore, the interference fringes at these wavelengths will have a greater magnitude than those wavelengths closer to the critical one. Note that this mechanism relies on the back wall of the channel being fairly close to the grating interface. This is because the periodicity of the fringes will decrease with increasing pathlength difference between the transmitted and reflected waves, until ultimately the fringes would disappear. This would explain why, if this

mechanism is correct, the fringes were observed with the sampling interface presented in the experimental section, since the back wall of the channel in that case was 50 microns away from the grating interface. Furthermore, the exact periodicity and amplitude of the fringes generated by this mechanism also relies on the combination of incident angle, beam width and collimation, and grating period, just as the waveguiding mechanism discussed above. Thus, neither mechanism can be disproven – based on the existing data – until more experiments are conducted.

Regardless of which of the two mechanisms presented above (or any combination of the various parameters listed in each of them) proves to be responsible for the fringes, the peaks of the chromatogram in figure 6.3 can be assigned to specific components of the injected sample based upon the behavior of the difference spectra that compose those peaks. For example, figure 6.6 shows the spectra for the two main peaks relative to the baseline water response. The fringes in both analyte spectra decline in magnitude as they approach the critical wavelength, and in fact disappear within a few nanometers of it. This phenomenon is consistent with both of the scenarios presented above. The critical wavelengths then show up as large negative peaks in the spectra, due to the subtraction of the water spectrum from them. The component assignment of these two peaks follows from a consideration of the changes in reflectivity that occur at the grating / sample interface upon either a refractive index or absorbance change.

Figure 6.7 illustrates what happens to the reflectivity of the zeroth order reflection when the refractive index of the interface changes by 0, +.0005, and +.001, respectively. A "baseline" effective absorbance of .0005 Imε has been added to these spectra to more closely simulate actual GLRS reflection spectra. In figure 6.7, the zero offset refractive index spectrum was subtracted from the each of the two incremented refractive index spectra, to simulate the chromatogram procedure. As expected, there is a sharp dip in the difference spectra near the critical wavelength, similar to the real data in figure 6.6 and the sensitivity plot of figure 6.5. However, there is also a substantial decrease in the reflectivity at the wavelengths to the transmitted side of the critical wavelength. This is the key to the analyte assignments in figure 6.4 and figure 6.6.

The features of these spectra can be explained when one considers how the fringe patterns for each peak change as the analytes elute past the detector interface. Figure 6.10 shows this for the first main peak, centered at spectrum #90. The other two difference spectra in this figure are taken from the "half maximum" points on the rise and fall of the elution peak. When plotted together, these three spectra show that, as the analyte is eluting, the phase shift and the reflectivity at the grating / sample interface is changing dramatically, resulting in positive and negative offsets of the fringes relative to zero. This is explained by changes in the optical pathlength in the channel as the analyte flow through the sampling volume, and by significant changes in the reflectivity of the interface, such as occur for the hypothetical difference spectra in figure 6.8. Therefore, this analyte must be a refractive index perturber present at a fairly large concentration to

induce such a large response. The only component of the sample that satisfies this condition is the phosphate buffer.

Finally, notice that the behavior of the critical point "dip" is symmetric with analyte concentration; that is, the magnitude and shape of the dip is approximately the same at the half maximum points of the elution peaks. However, the fringes are very asymmetric: the offset and magnitude of the fringes are different for the two half maxima, even though one would expect the concentration and identity of the analyte to be the same at these two points. This is again indicative of a changing refractive index gradient, in which both the effective pathlength and reflectivity experienced by the transmitted wavelengths are changing over the course of the elution peak.

In contrast, the only case in which the resultant fringe patterns can be symmetric with the shape of the elution peak is one in which the magnitude but not the pathlength-dependent phase of the fringes is changing. Figure 6.10 shows how this can happen with GLRS data. Here, only the absorbance has incremented between the three hypothetical spectra; the refractive indices of each are the same. When the difference between the incremented absorbance spectra and the baseline spectrum is taken, as in figure 6.11, it is seen that there is still a dip near the critical wavelength, as with the incremented refractive index spectra of figure 6.8. However, now there is no significant change in the reflectivity to the transmitted side of the critical wavelength. This means that there is no increase or decrease in the energy transported into the critical diffraction order. Therefore, the fringe patterns resulting from the overlap of the transmitted wavelengths

with the zeroth order reflections in these cases will not show a variable intensity offset with respect to each other. However, because the bromocresol green molecule possesses a broad and strong absorbance band over all of the transmitted wavelengths (610 to 630 nanometers) contained in these difference spectra, the intensity of these wavelengths will be attenuated as they travel to the back wall of the flow channel before reflecting and overlapping with the zeroth order reflection. This means that the fringes of the dye spectrum would have less contrast than the water fringes. As seen in figure 6.12, the fringes in the difference spectra that span the elution peak centered at spectrum #124 exhibit this behavior. Furthermore, the spectra at the half-maximum points are almost exactly the same in appearance and magnitude: this means there is no refractive index gradient in the sampling volume. Therefore, spectrum number 124 in figure 6.6 must belong to bromocresol green, which is the only significant absorbing component present in the injected sample.

Finally, figure 6.13 shows the wavelength difference spectra corresponding to the two unknown impurity peaks shown in the chromatogram of figure 6.4. There are no sharp features in these spectra, except perhaps near the critical wavelength. Furthermore, the overall reflectivity of these spectra at all wavelengths show significant deviation from the water baseline, indicating that these two components are refractive index perturbers. In fact, these spectra show the same broad features (but with no prominent fringe pattern) as those of spectrum #80 in figure 6.9. The overall intensity is offset below zero on the

transmitted side of the critical point and is offset above zero on the evanescent side of the critical point.

This is expected, since the 15% impurities in the original bromocresol green stock are likely to be counter ions (salts) or leftover solvent from the crystallization process. For example, many dyes are re-crystallized in methanol, a common organic solvent with a lower refractive index than water. In addition, dyes are commonly available as a salt so that they will be soluble in water. The fact that these peaks elute at the start and end of the run, respectively, suggests that they are markedly different in chemical composition. Thus the impurities in the dye solution may consist of both an organic solvent and some inorganic salt.

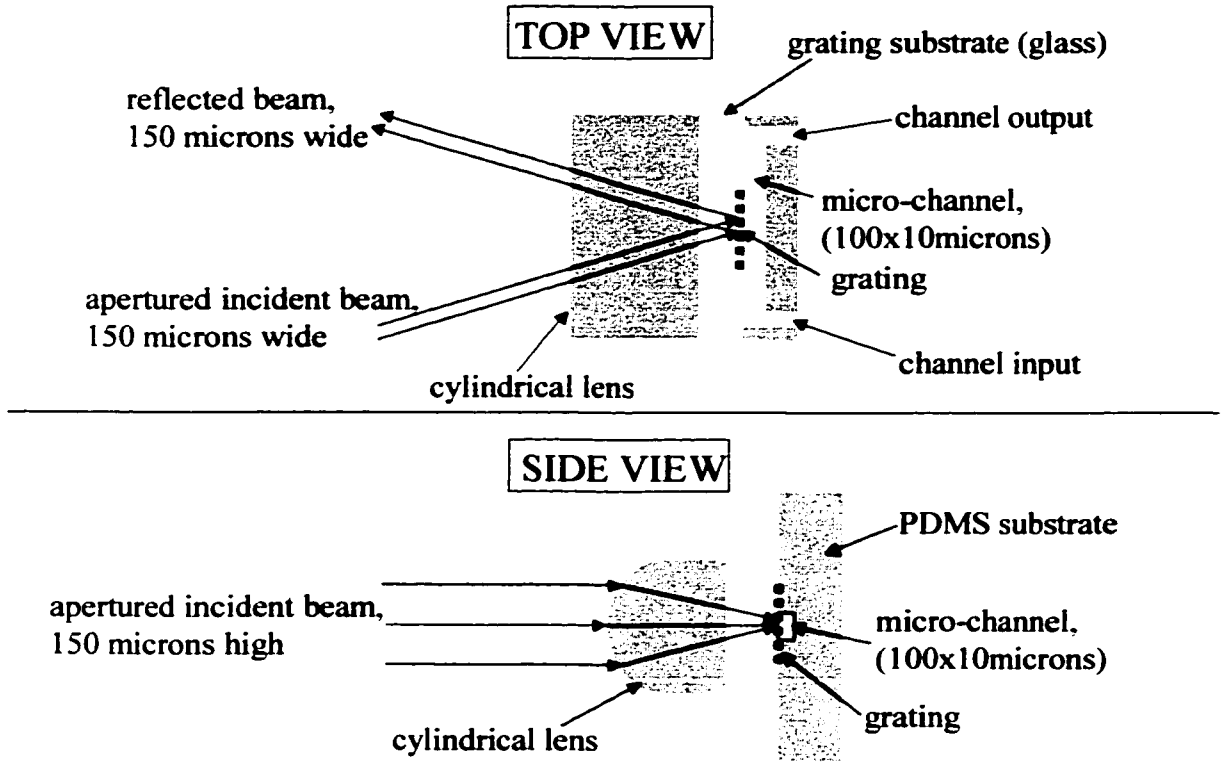

Figure 6.1 Optical coupling at the grating / sample interface of the micro-channel flow cell. Note the reduced scale relative to the dynamic sampling interface described in the section 3.2.

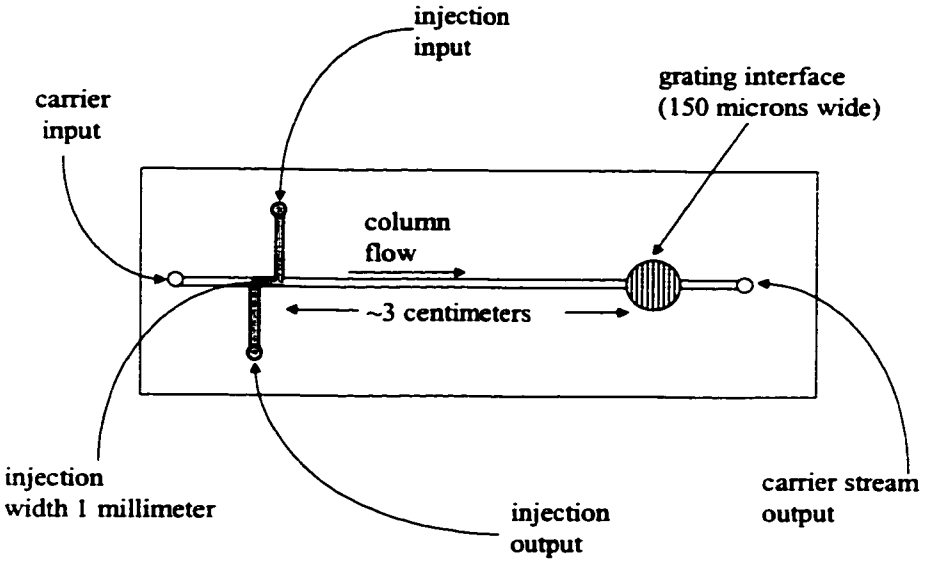

Figure 6.2 Illustration of the various components of the micro-channel chromatographic column formed in the PDMS substrate.

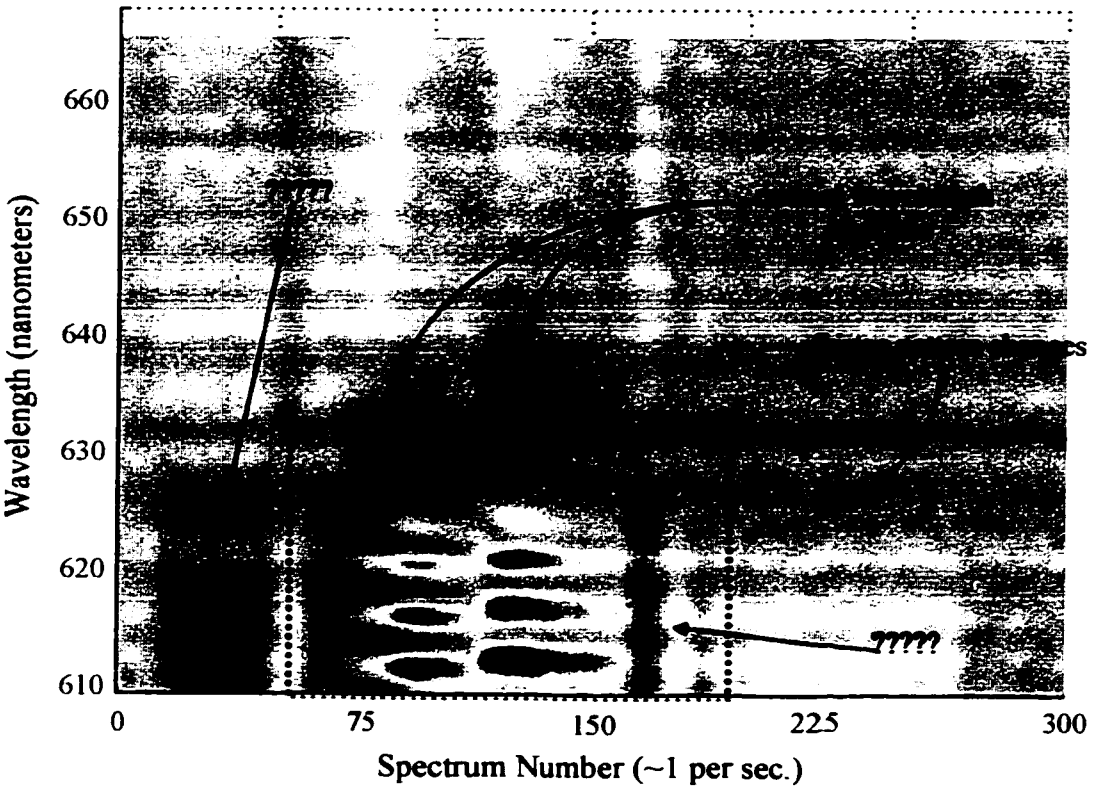

Figure 6.3 3-D chromatogram of 10^{-4}M bromocresol green in an aqueous buffer of 0.125M phosphate with unknown impurities.

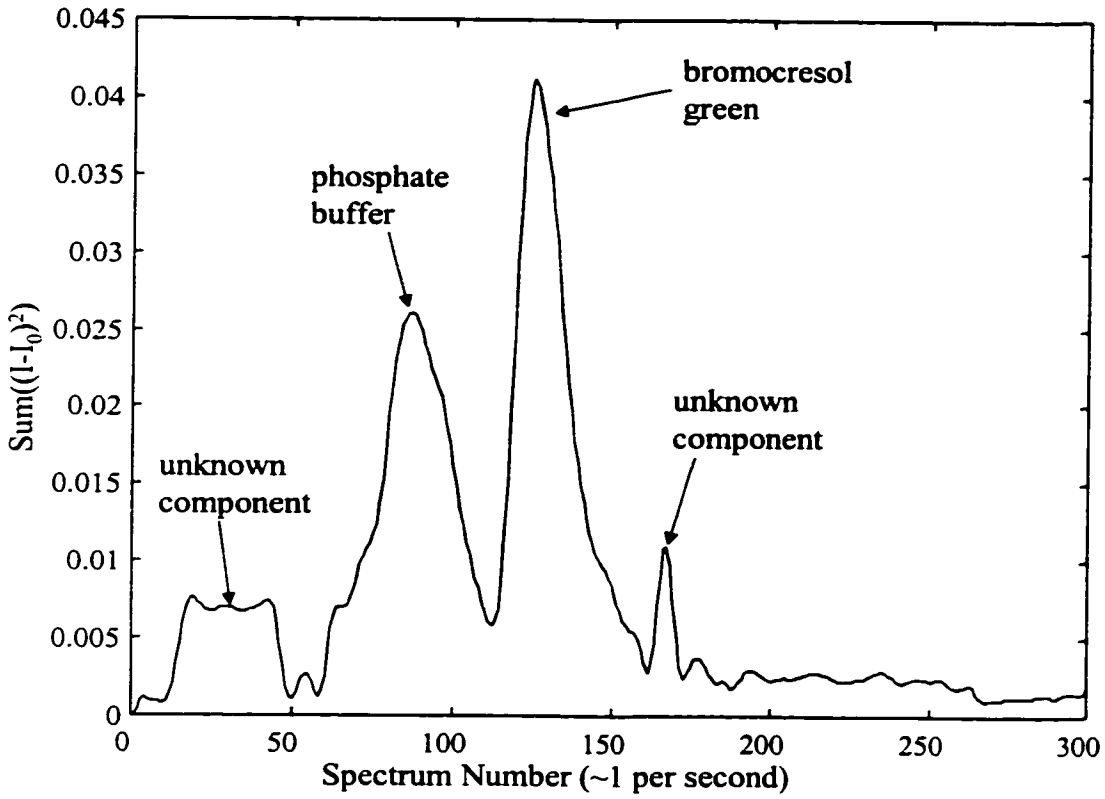

Figure 6.4 Formation of the time-dependent chromatogram by taking the sum of the squared intensity differences between each spectrum and the mean "baseline" (i.e. solvent) spectrum.

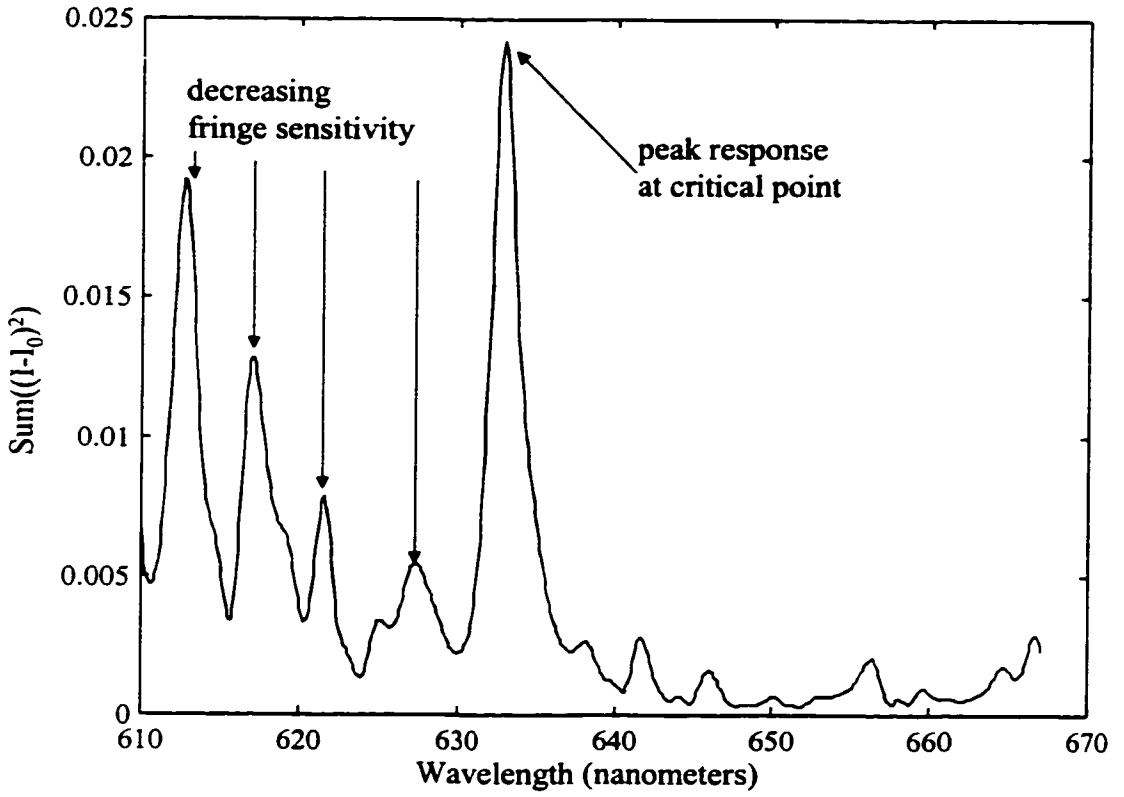

Figure 6.5 Sum of the squared intensity differences for each wavelength over the length of the chromatogram, showing the maximum in the overall response at the critical wavelength.

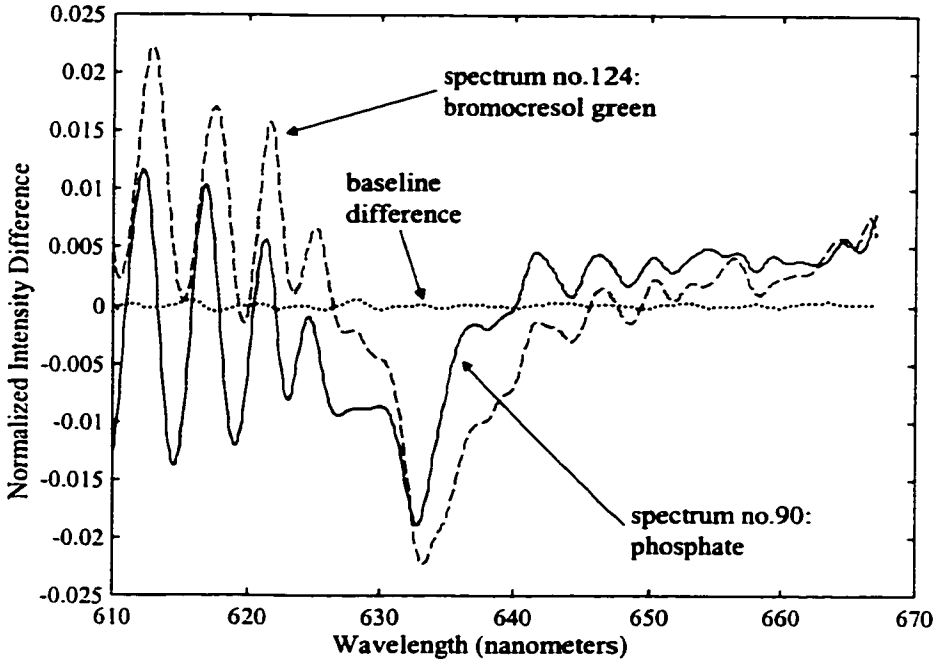

Figure 6.6 Difference spectra corresponding to the tops of the two main peaks in the chromatogram in figure 6.4.

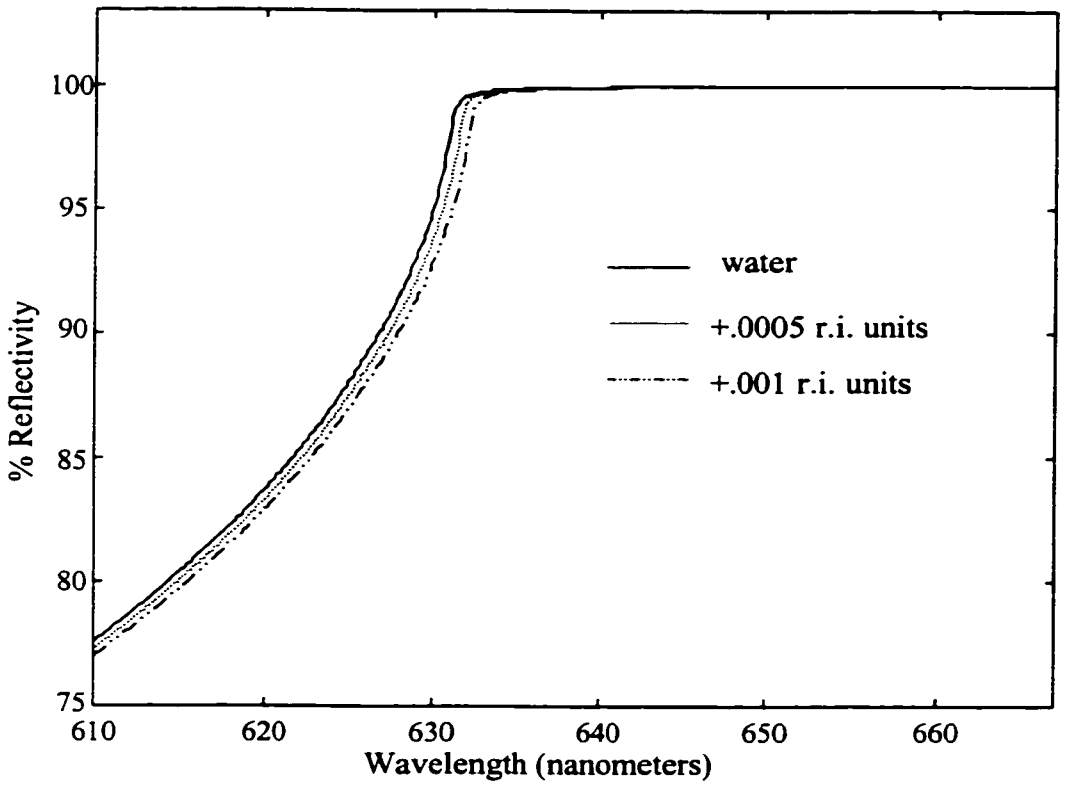

Figure 6.7 Theoretically ideal GLRS Reflectivity spectra as a function of increasing sample refractive index.

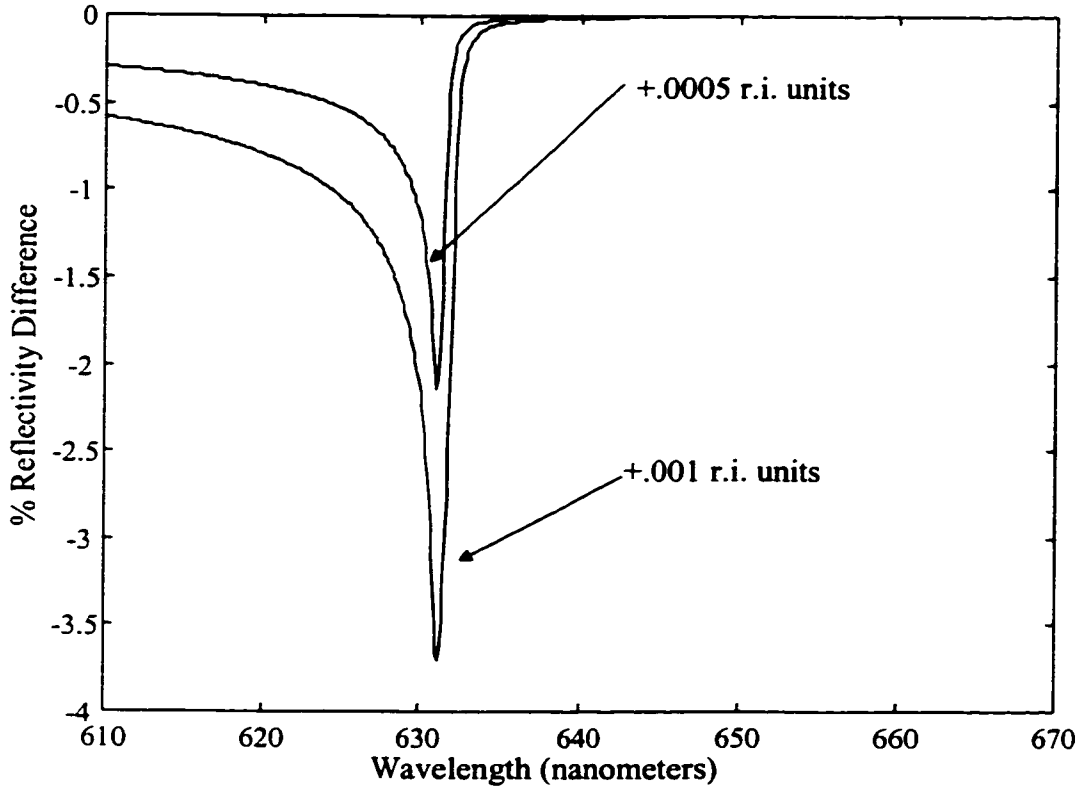

Figure 6.8 Difference spectra generated from the spectra of figure 6.8, showing the effect of sample refractive index changes.

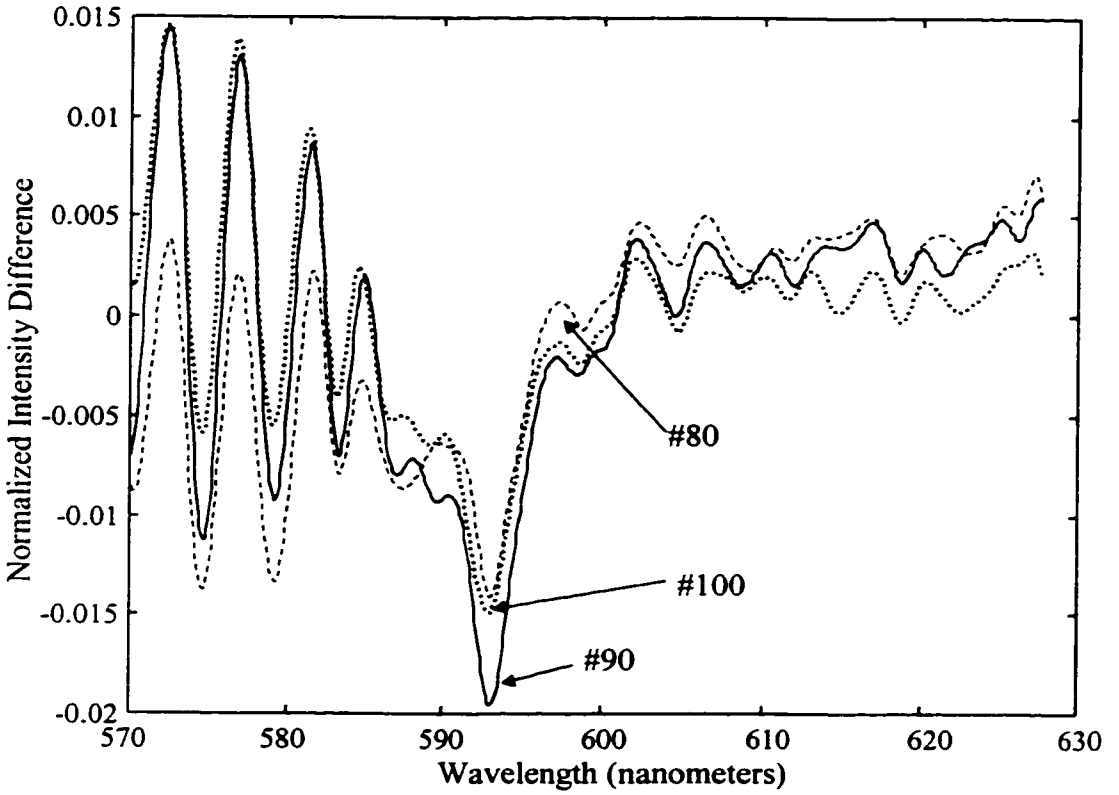

Figure 6.9 Difference spectra spanning the first main elution peak, centered at spectrum #90.

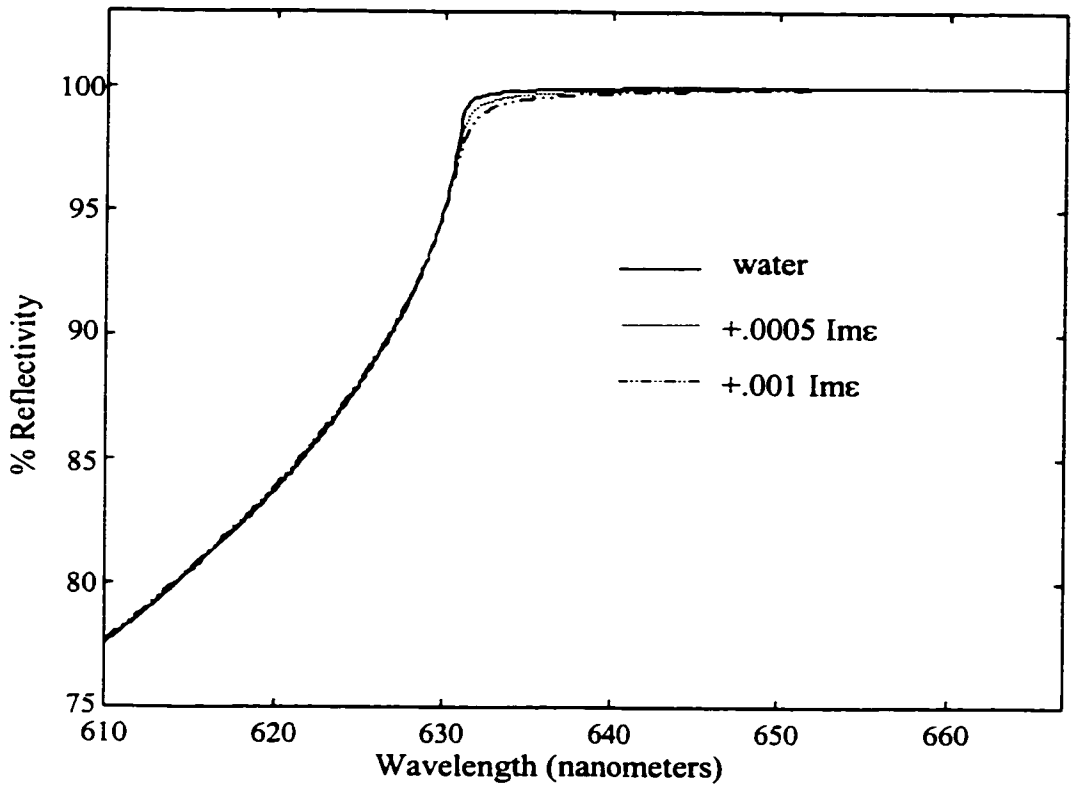

Figure 6.10 Theoretically ideal GLRS Reflectivity spectra as a function of increasing sample absorption.

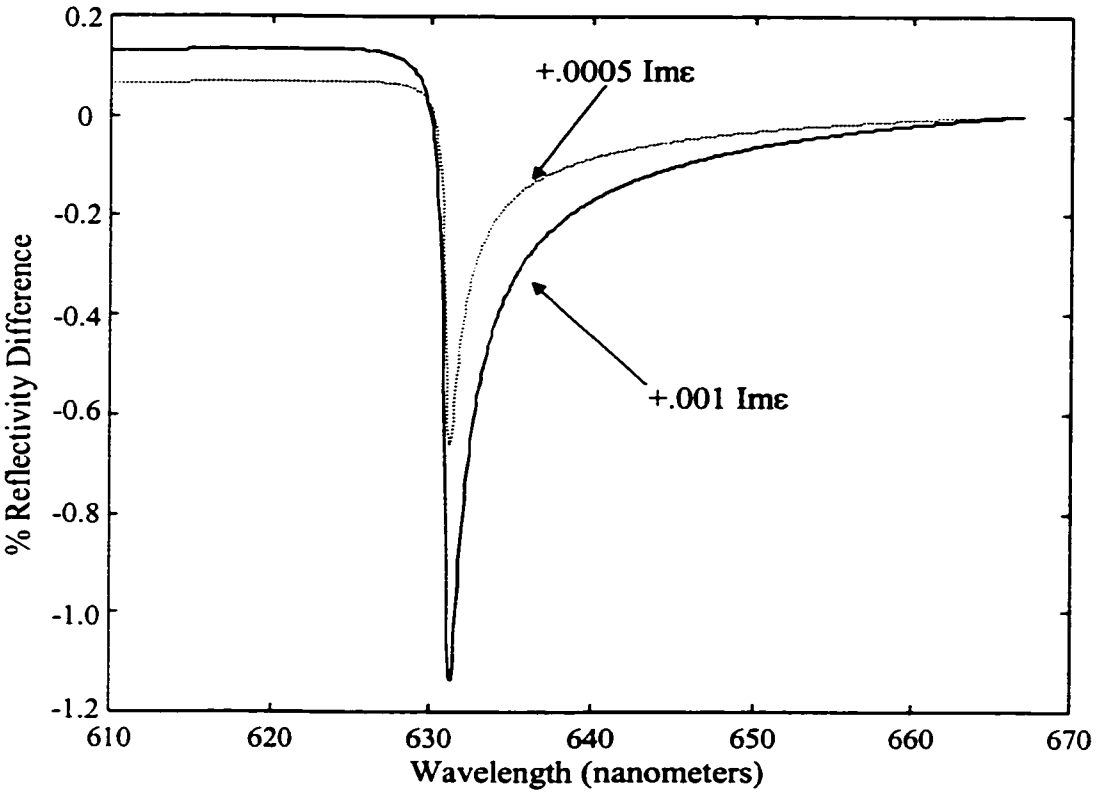

Figure 6.11 Difference spectra generated from the spectra of figure 6.11, showing the effect of sample absorption changes.

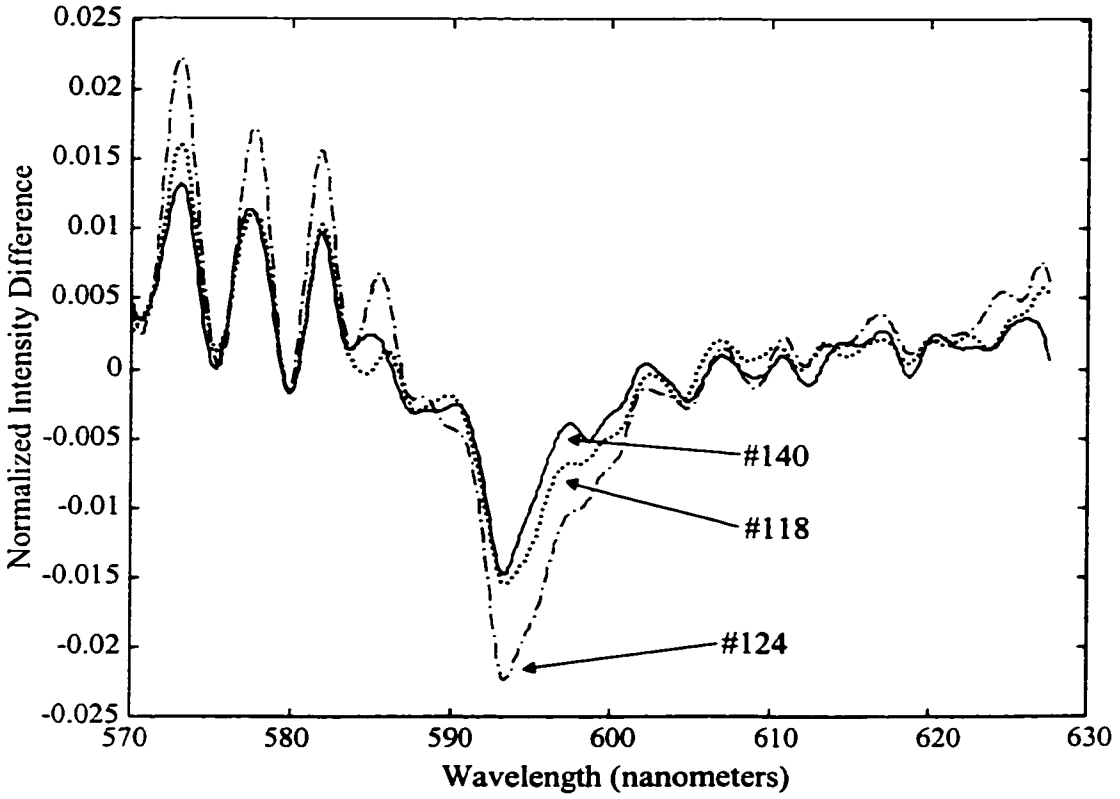

Figure 6.12 Difference spectra spanning the second main elution peak, centered at spectrum #124.

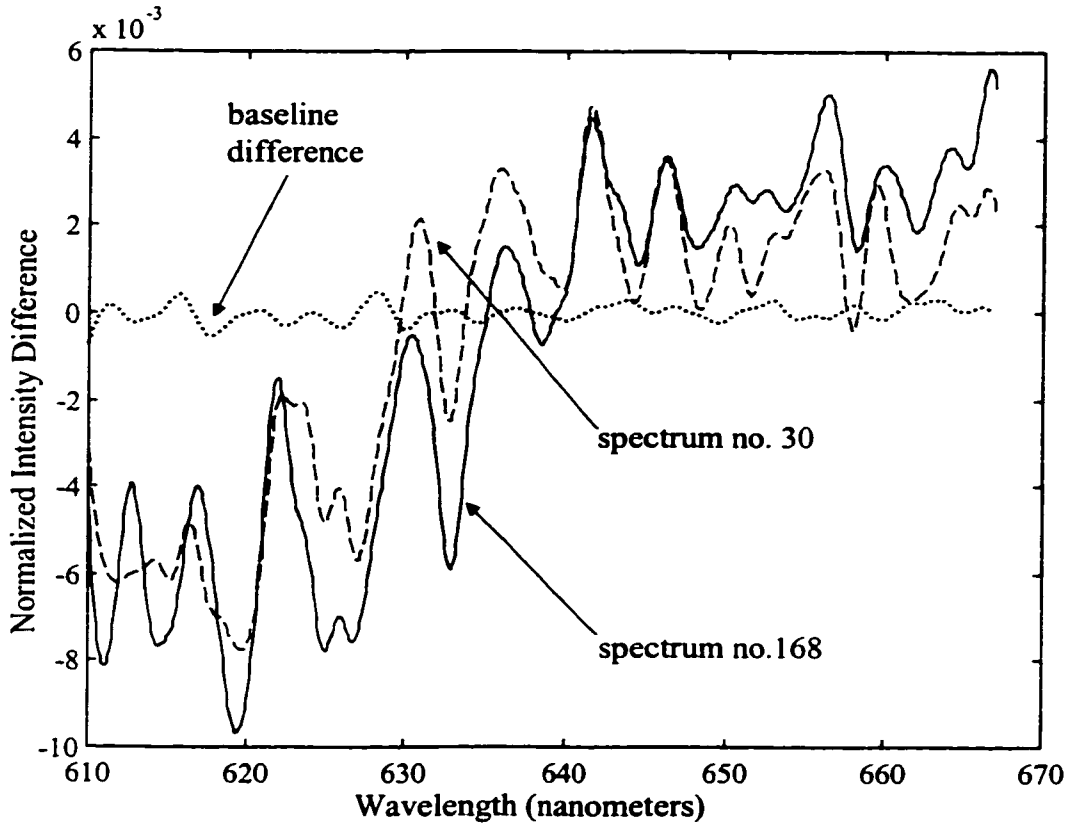

Figure 6.13 Wavelength difference spectra corresponding to the two unknown impurity peaks shown in Figure 6.4.

Chapter 7

Conclusion

7.1 Significance of the Results Presented in this Thesis

GLRS has proven useful in the quantitation of the complex refractive index of homogeneous and heterogeneous sample matrices over a broad dynamic range. Its use as a detector for a micro-capillary liquid chromatography column, where it detected both absorbing and non-absorbing analytes in the same injection sample, has confirmed the combination of sensitivity and versatility inherent in the technique. Furthermore, GLRS has exhibited extreme sensitivity to the size of scattering particles, due to its ability to monitor changes in the single-particle complex forward scattering amplitudes of these heterogeneities at concentrations of several volume percent. These concentrations prohibit the use of transmission-based particle sizing techniques. Finally, the development of a simple and quantitative theoretical model of the data has proven critical to the technique's performance in all of these areas.

Thus, the practice and understanding of GLRS have advanced to the point where we can now fulfill the over-arching goal set for the technique at its inception. That is, to implement a simple, durable, sensitive and versatile chemical sensing probe that relies

only on the interaction of light with a sample in contact with a regular dielectric permittivity modulation (i.e. a diffraction grating).

7.2 Implications of Results On Future Work

The remainder of this chapter will serve to discuss the results presented in this Thesis with regard to their impact on the future of the GLRS technique. Attention will focus in particular on how best to implement the technique as a, mobile independent chemical probe rather than as a laboratory benchtop apparatus.

7.2.1 Absorbing and Non-absorbing Molecules

The observed limits of detection and dynamic ranges of GLRS are more than adequate to implement the technique in a probe format "as-is". Once again, note that the stated limits of detection with respect to refractive index and absorbance are actually limits of the present implementation of the technique, and not of the technique itself. For example, the quantitation of the position and slope of the critical point in a GLRS reflection spectrum depends on the spectroscopic properties of the detector in addition to the properties of the interfacial grating itself. In addition, instrumental instabilities such as mechanical and temperature drift limited the performance of the apparatus. All of these limitations can be overcome in specific implementations of the technique. Witness the

multitude of clever manipulations of the basic Surface Plasmon Resonance technique to achieve higher refractive index sensitivities and optimized selectivity to particular analytes. However, more theoretical and experimental work should be done to determine the diffraction grating properties desired for optimization of the technique. Some ideas for how this work should progress are given below.

In addition to optimizing the grating itself, the selectivity and sensitivity of the technique to specific analytes can be improved by adding a transduction layer to the grating-sample interface. For example, a stationary phase or biomolecular surface could be superimposed on the grating to allow for selective adsorption of analytes. In addition, an electrode material could be deposited over the grating to allow for electrochemical modulation of the sample. In fact, as described in the Introduction, the recently concluded collaboration with Sandia National Laboratory has shown that such a setup allows for ppb detection levels of analytes with absorption bands near the singularity wavelength.

This last result raises another issue: the fact that GLRS will only detect the presence of absorbing molecules that exhibit significant absorption near the critical wavelength. A review of the GLRS theory concludes that, for any particular implementation of the technique to be useful for monitoring a particular wavelength region regardless of the refractive index of the sample, we must be able to change either the incident angle or the period of the grating. While this appears impractical with regard to the operation of a stand-alone chemical sensor, it is in fact possible to simulate these factors by having the incident beam impinge upon the grating at different angles *relative*

to the axis of the grating lines. When this possibility is taken into account, the basic GLRS equation for determining the wavelength position of the singularity becomes:

$$\lambda_{crit} = \Lambda\left(n_{samp} + \sin\theta_i \sin\phi - \sin\theta_i \cos\phi\right) \qquad (1)$$

where all of the familiar terms are present and ϕ is the angle of the incident beam with respect to the grating lines. Note that this is equivalent to changing the grating period, since for values of ϕ other than 90° the incident beam will "experience" a wider grating spacing (see figure 7.1). For example, a mount could be constructed that allows for free rotation of the grating with respect to the incident optical plane, such that the critical wavelength could be tuned to the absorbance maximum of a particular analyte before conducting a measurement. Figure 7.2 shows the critical wavelength versus ϕ for a hypothetical combination of a 450 nanometer period grating with light incident on an aqueous sample (n = 1.33) at an angle of 30°: absorbances throughout the visible spectrum could be "tuned in" by rotating ϕ from 0° to 90°. This situation could also be approximated using no moving parts via the use of multiple input (and output) fibers arranged in a circle around the grating surface.

7.2.2 Scattering Matrices

These results demonstrate that it is possible to distinguish size differences in particles distributed in water whose radii vary by less than 1 nm. More generally, we have demonstrated that the analysis of GLRS experimental data allows us to get

substantive information about structural characteristics of non-uniformities in a strongly scattering medium. This can be done even in the case where the characteristic length of these non-uniformities is substantially less than the scattered light wavelength, and can in fact be on the order of molecular dimensions. Realistic possibilities thus exist for measuring such processes as cluster formation and polymerization reactions, crystal formation, and surface and bulk phase transitions.

This impressive size resolution has implications beyond straightforward particle size determination. We envision GLRS as a general chemical sensing technique that has many applications in areas occupied at the present by more complicated methods. For example, bioanalytical assay methods that rely on conformational changes in proteins upon binding to some target analyte could take advantage of the fine size resolution of GLRS to directly measure changes in protein structure. This relatively simple reflection, which can easily be multiplexed to contain many simultaneous measurement channels, would thus replace less robust and more expensive methods such as SPR adlayer refractive index changes or fluorescent tag detection.

Furthermore, the resolution demonstrated in this work could be improved upon by developing higher quality diffraction gratings with more regular periodicity, and by conducting measurements in the near UV frequency interval, where optical contrasts between organic materials and water (or air) increase dramatically.

Finally, the sensitivity of this method would greatly improve in certain types of gas phase sample matrices such as aerosols, where the optical contrast between the particles and the solvent (air) would be much greater than for the dendrimer samples presented here. This means that each scattering event occurring at these points of high dielectric contrast will result in much more incoherent scattering, and thus a stronger GLRS signal change, than would occur for particles of a similar size in a liquid matrix. Furthermore, the pathlength of such measurements would be far greater than in condensed phase matrices, which would compensate for the diminished number of scattering events per volume occurring in gas phase systems.

7.2.3 Optimum GLRS Grating Characteristics

The most powerful aspect of GLRS is that the properties of its detection interface – the diffraction grating – can be tailored to suit virtually any sample. The materials out of which the grating is made can be either inert to the sample or selective reactive towards an analyte of interest within the sample. In addition, the grating / sample interface can be augmented with a third layer to enhance some property of the sample without destroying the sensing ability of the technique. Furthermore, the period and modulation depth of the grating can be adjusted to provide the best possible optical properties for a given spectral range.

As described in the Theory, larger grating periods are required for optimal refractive index sensitivity. However, the choice to go to larger periods has certain adverse effects that make it an unwise choice with respect to chemical sensing, especially in the visible region of the spectrum. First, according to equation (1), the incident angle required to tune the critical condition to a certain wavelength increases with increasing grating period. This means that in aqueous samples (refractive index ~ 1.33), the theoretically largest possible period that can be used to allow for tuning the critical condition to any wavelength in the visible region of the spectrum is 1200 nanometers. This grating, when used at an incident angle of 89° would place the critical condition at a wavelength of 400 nanometers. Furthermore, even this most extreme case for utilizing GLRS in the visible region of the spectrum yields a refractive index sensitivity increase of only perhaps 1200/500 or 2.4 times that of a 500 nanometer period grating, which allows for comfortable sensing from 237 nanometers at a 60° incident angle to 665 nanometers at 0° incidence. Of course, larger period gratings could be used in higher diffraction orders to tune for lower wavelengths, but the diffraction efficiency in these orders is usually so poor that the analytical performance of such an arrangement would be severely degraded due to low signal-to-noise ratio. Finally, extensive studies on the diffraction efficiencies of gratings[45] have demonstrated that virtually all gratings exhibit their highest efficiencies at wavelengths of between 1x and 2x the grating period (except

---

[45] Petit, R., ed. *Electromagnetic Theory of Gratings*, Springer-Verlag, Berlin, **1980**, Chapter 6.

for blazed gratings, see below). Again, for analytical performance reasons, this makes a grating period of perhaps 300 to 500 nanometers the best choice for GLRS detection in the visible region of the spectrum.

Shorter grating periods are also preferable due to the opportunities that exist for detection in the ultra-violet spectral range. Here many molecules exhibit significant absorption, and the dielectric contrast between water and most organic molecules increases dramatically, so that the evanescent wave at the critical point would experience much more coherence loss in both absorbing and non-absorbing (i.e. scattering) aqueous sample.

The other grating properties of significance are the groove profile and the modulation depth (i.e. the "thickness" of the grating lines). Although an argument might be made that a blazed grating could increase the diffraction efficiency in a certain wavelength region, this would mean that wavelengths outside the optimized region would suffer in performance. Furthermore, research on different grating profiles has shown that square-grooved gratings exhibit the strongest "Rayleigh anomalies" (critical wavelengths), especially at modulation ratios of roughly 0.25 (i.e. groove height divided by grating period).[46] Finally, square profiled gratings exhibit the most uniform efficiency over their spectral range relative to other grating profiles (sinusoidal, triangular, trapezoidal), so that they should prove the most versatile with respect to performance in a

---

[46] Petit, R., ed. *Electromagnetic Theory of Gratings*, Springer-Verlag, Berlin, **1980**, pp .190.

diverse range of chemical sensing applications. The rule of thumb is that a grating's efficiency curve will resemble its groove profile: a square groove will show a flat efficiency vs. wavelength profile, a sinusoidal groove will exhibit a rounded profile, a triangular (i.e. blazed) groove will show a peak in efficiency at a certain wavelength, etc.

7.3 GLRS Probe Construction

Once freed from the laboratory bench, the technique will be able to "flex its muscles" by conducting measurements on systems that are difficult to reproduce in a laboratory setting, such as *in situ* environmental sampling and in-line chemical reaction monitoring. One of the primary difficulties in conducting GLRS research to date has been the engineering of the sampling interface, because we have intentionally directed our work toward analytes that do not behave well using conventional sampling (and detection!) strategies. For example, extremely optically dense samples often contain high concentrations of molecules whose functional groups react adversely with the walls of sample cells by either staining them, or dissolving or leeching into them, or clogging them. Likewise, heterogeneous matrices often clog the tubes of a flow system, preventing the use of sample sets with a broad dynamic range with respect to particle concentration. In addition, many industrially significant matrices may simply be too viscous to flow at all through a laboratory-scale sampling system. Finally, certain matrices, such as those

involving polymerization or crystallization reactions, necessitate the construction of elaborate reaction vessels to control the mixing of analytes and reagents.

Since we are concerned with the implementation of GLRS and not with the implementation of sampling systems, the most efficient strategy for developing these applications of GLRS is to focus on the construction of a durable and versatile sensing vehicle that will allow us to couple GLRS to existing sampling systems. This approach will also render determinations of bulk industrial or environmental samples much more efficient by enabling simple "dip probe" measurements: quick, easy, and verifiable cleaning of the grating between samplings is a far-from-trivial aspect of complex sample matrix sampling. Indeed, many otherwise promising analytical techniques (SPR, electrochemistry) become useless in the face of a fouling analyte matrix due to their fragile sensing interfaces.

Work has recently begun on a probe prototype that utilizes the grating in a 0° incidence setup. This particular incident angle has several useful attributes with respect to the construction of a workable probe. It obviously makes the optical train simpler by allowing the use of only one optical fiber, which serves to both launch the incident beam and collect the zeroth order reflection, which is funneled via a fiber splitter to the detector. In addition, this setup makes polarization of the input beam less important (though in fact polarization is not strictly necessary at any incident angle: the grating and coupling optics will always impose some degree of polarization on the detected light beam). This is because the light is impinging normal to the front surface of the grating

substrate, so that no polarization-dependent reflection losses occur (at any other angle, TE polarized light will be more strongly reflected than TM polarized light). Indeed, this alignment makes it easy to eliminate all reflection losses by "collapsing" all of the necessary optical train elements: that is, the fiber coupler, the collimating lens, and the grating substrate, into a seem-less whole. This can be done virtually using index-matching epoxy, or physically by placing a grating directly on the end of an optical fiber (similar to a Bragg grating, which is made by burning a laser interference pattern into the core material of the fiber). In addition, this alignment results in a degeneracy among the + and – diffraction orders, such that the critical condition appears in both the +1 and -1 transmitted diffraction orders (see figure 7.3). This serves to double the signal-noise ratio and thus improve the analytical performance.

Finally, this optical arrangement results in the widest possible dynamic range with respect to refractive index detection using GLRS. The technique has the advantage of being completely linear in refractive index response over that entire dynamic range, as well. The dynamic range itself is limited only by the bandwidth of the detecting optics. Thus, for this setup, which uses a 500 nanometer sensing grating and a conventional CCD detector, the refractive index range is from 1.0 (critical wavelength at 500 nanometers) to 2.0 or more (critical wavelength of 1000 nanometers). This is with a nominal resolution of .001 refractive index units ($\partial\lambda/\partial n = 1/500 = .002$ with detector resolution of 0.5 nanometers), though of course it can be enhanced through fitting or multivariate analysis techniques. Figure 7.4 shows some typical reflection spectra taken for different refractive

index samples (air r.i. = 1.0, water r.i. = 1.333, ethyl. glycol r.i. = 1.43). (Note: I wish to thank Mazen L. Hamad for collecting these spectra).

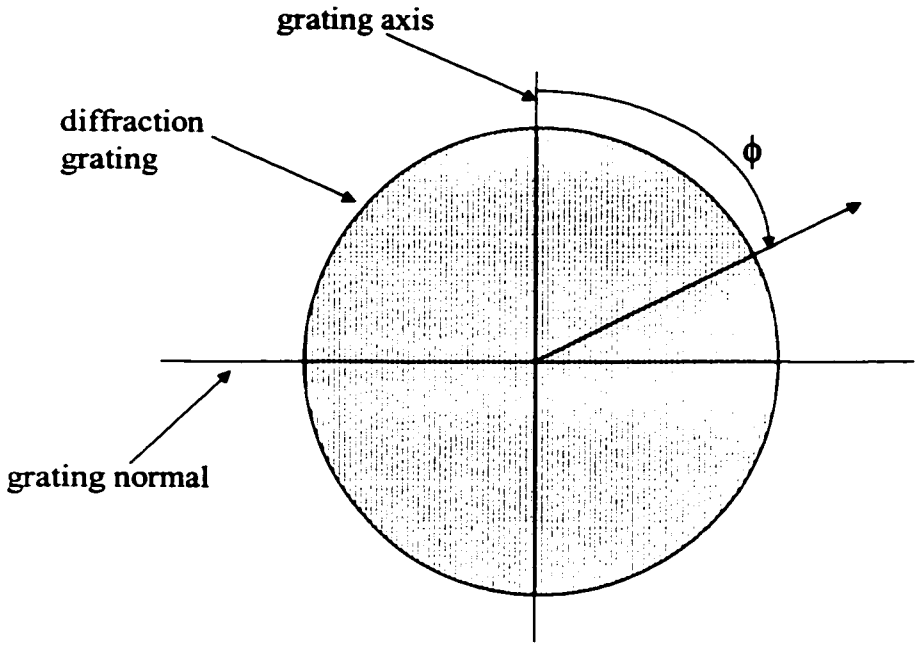

Figure 7.1 Coordinate system for orientation of the grating grooves relative to the optical plane.

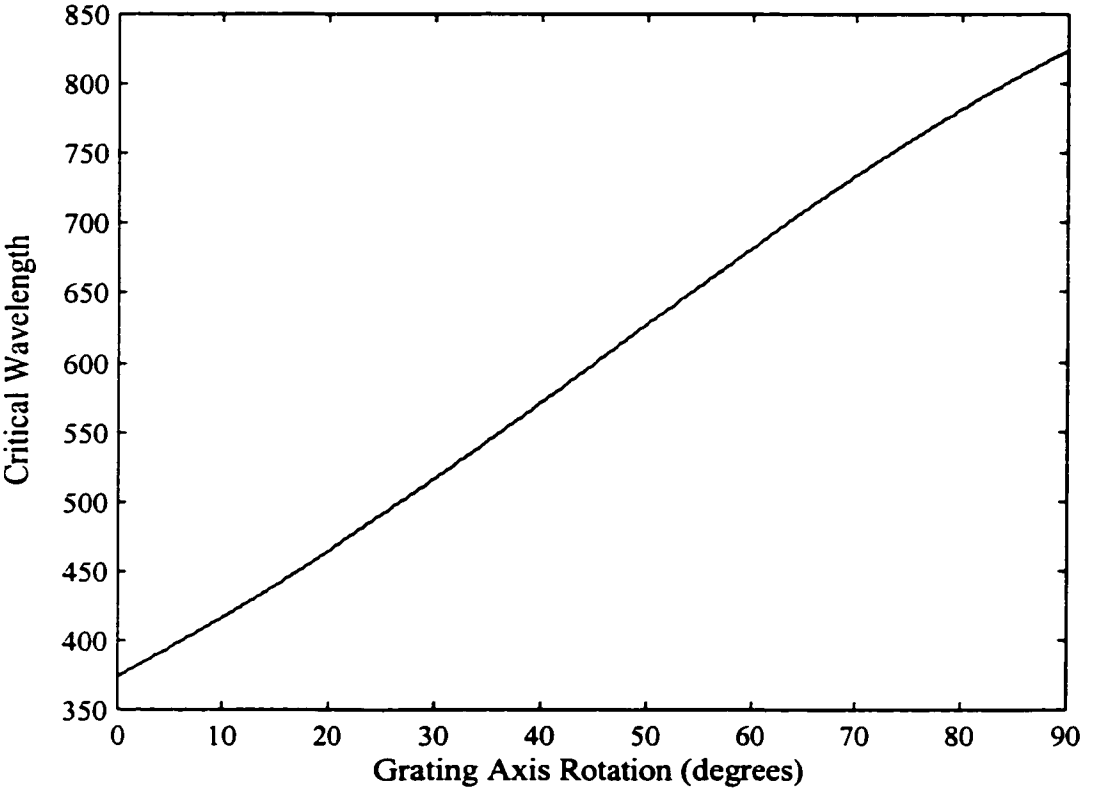

Figure 7.2 Critical wavelength versus ϕ for the hypothetical combination of a 450 nanometer period grating with light incident on an aqueous sample (n = 1.33) at an angle of 30°.

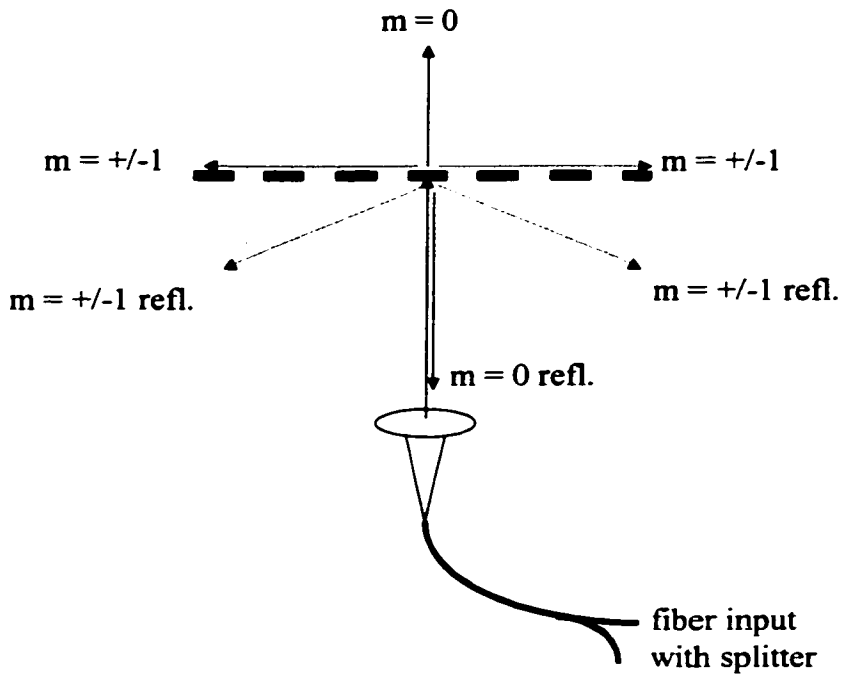

Figure 7.3 Illustration of the degeneracy among the + and – diffraction orders, such that the critical condition appears in both the +1 and -1 transmitted diffraction orders at 0° incidence.

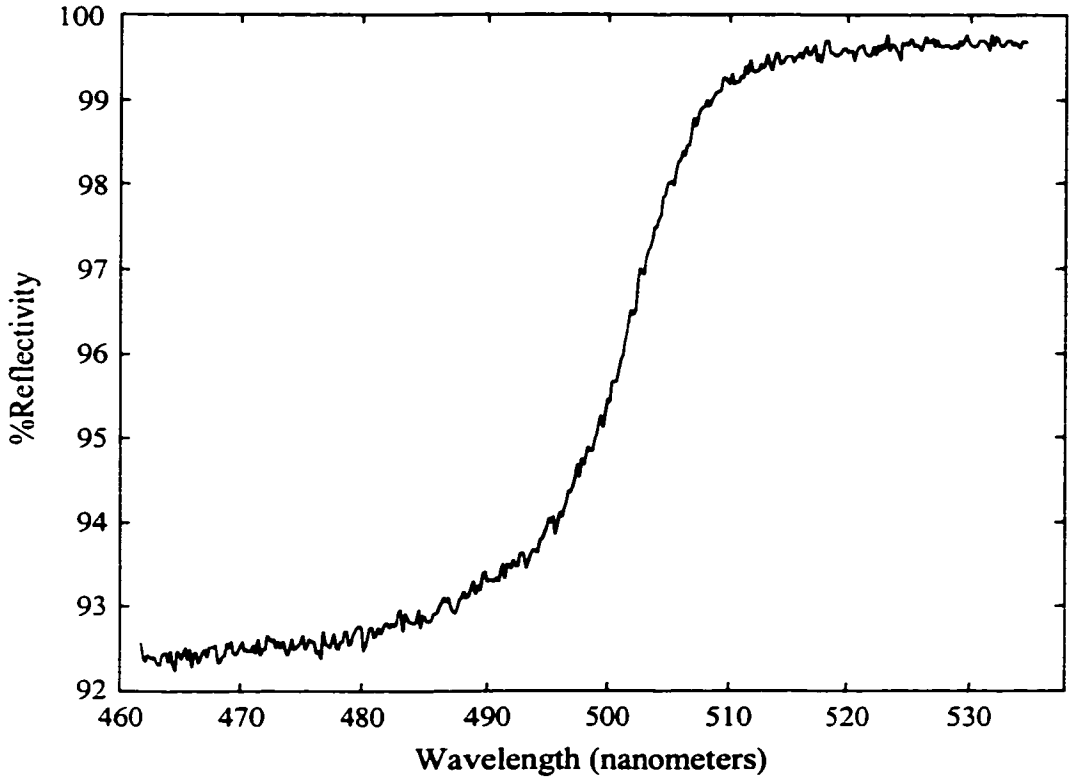

Figure 7.4 Reflectivity spectrum for the 0° incidence apparatus exposed to air (n = 1).

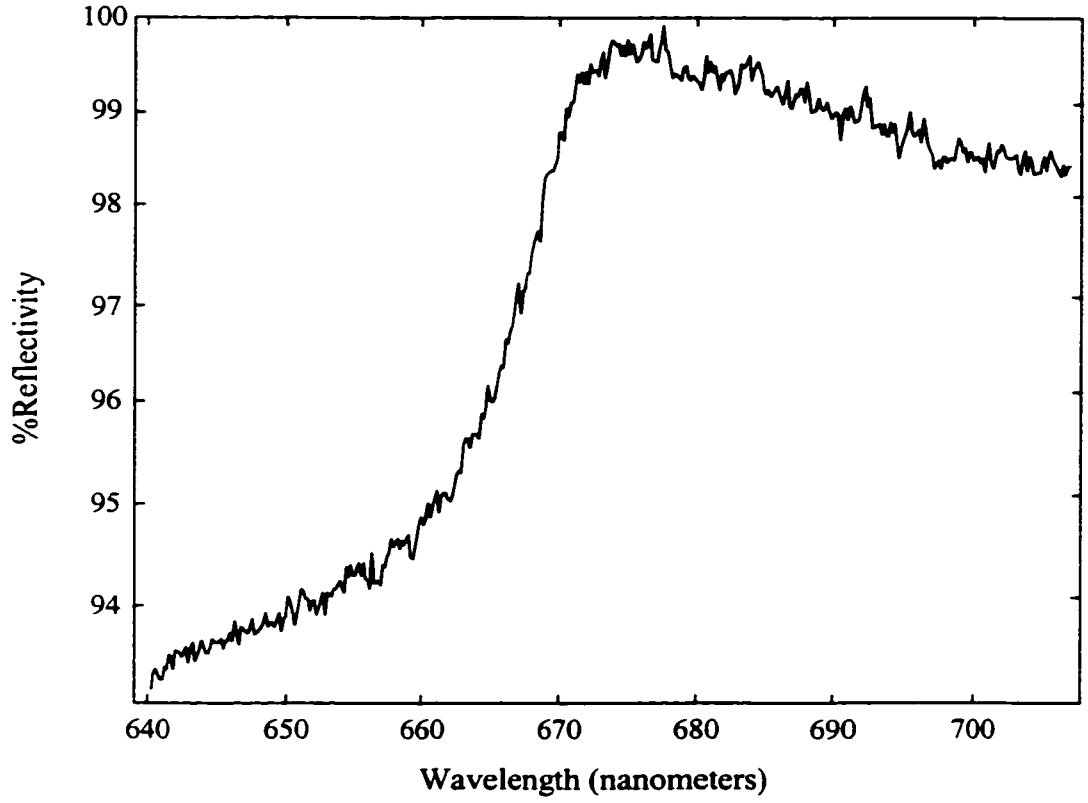

Figure 7.5 Reflectivity spectrum for the 0° incidence apparatus exposed to water (n = 1.33).

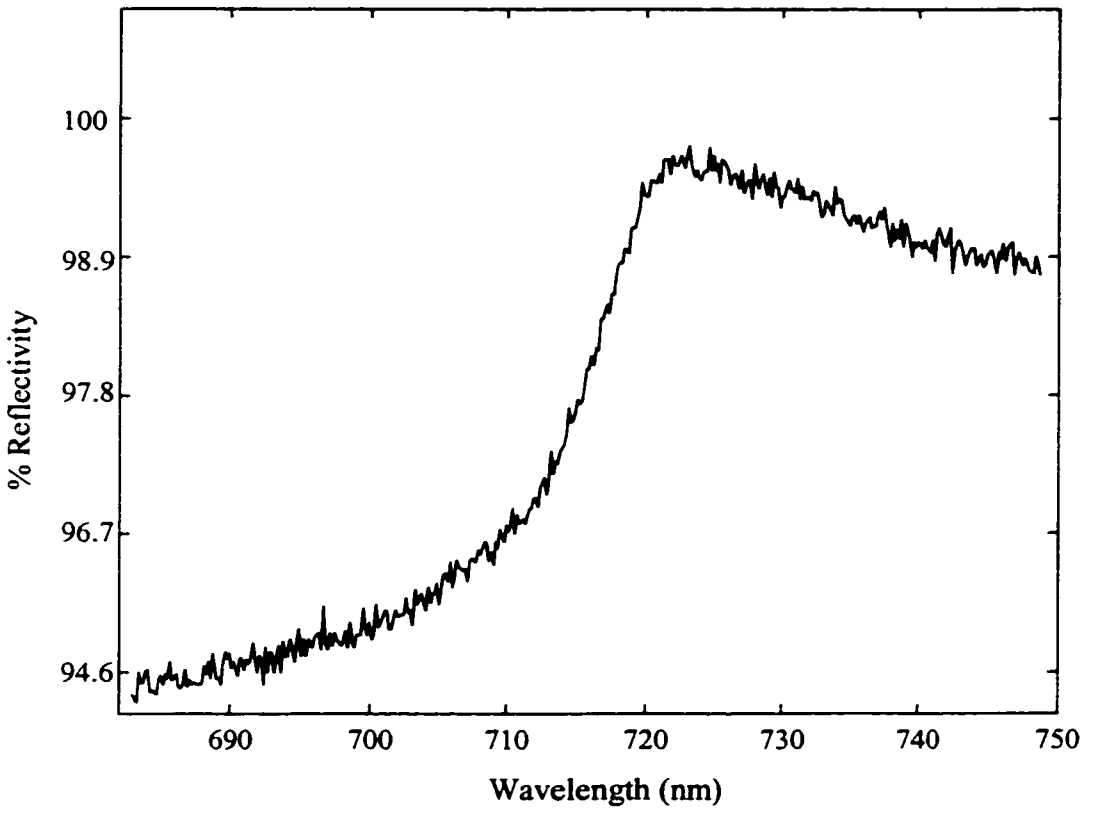

Figure 7.6 Reflectivity spectrum for the 0° incidence apparatus exposed to ethylene glycol (n = 1.43).

References

1. Allen, T. *Particle Size Measurement, Volume 1*, 5th edition, Chapman & Hall, London, **1997**, pp. 426-436.

2. Anderson, B. B. *Grating Light Reflection Spectroscopy*, Thesis (Ph.D.), University of Washington, **1996**.

3. Anderson, B. B.; Brodsky, A. M.; Burgess, L. W. *Analytical Chemistry*, **1996**, vol. 68, no. 7, pp. 1081-1088.

4. Anderson, B. B.; Brodsky, A. M.; Burgess, L. W. *Physical Review E*, **1996**, vol. 54, no. 1, pp. 912-923.

5. Anderson, B. B.; Brodsky, A. M.; Burgess, L. W. *Langmuir*, **1997**, vol. 13, no. 15, 1 Aug, pp. 4273-4281.

6. Atkins, P. W. *Physical Chemistry*, 4th Edition, Oxford University Press, **1990**, p. 471.

7. Born, M.; Wolf, E. *Principles of Optics*, 3rd Edition, Pergamon Press Ltd., Oxford, **1965**.

8. Brodsky, A. M.; Burgess, L. W.; Smith, S. A. *Applied Spectroscopy*, **1998**, vol. 52, no. 9, pp. 332A-343A.

9. Brynda, E.; Houska, M.; Brandenburg, A.; Wikerstal, A.; Skvor, J. *Biosensors & Bioelectronics*, **1999**, vol. 14, no. 4, pp. 363-368.

10. De Jaeger, N.; Demeyere, H.; Finsy, R.; Sneyers, R.; Vanderdeelen, J.; van der Meeren, P.; van Laethem, M. *Particle and Particle Systems Characterization*, **1991**, vol. 8, pp. 179-193.

11. Ditchburn, R. W. *Light*, Dover Publications Inc., New York, **1991**.

12. Duffy, D.C.; McDonald, J.C.; Schueller, O.J.A.; Whitesides, G.M. *Analytical Chemistry*, **1998**, vol. 70, no. 23, pp. 4974-4984.

13. Garbuny, M. *Optical Physics*, Academic Press Inc., New York and London, **1965**.

14. Hanning, A.; Roeraade, J.; Delrow, J. J.; Jorgenson, R. C. *Sensors & Actuators B*, **1999**, vol. 54, pp. 25-36.

15. Harrick, N. J. *Internal Reflection Spectroscopy*, Harrick Scientific Corporation, New York, **1979**.

16. Harris, R. D.; Luff, B. J.; Wilkinson, J. S.; Piehler, P.; Brecht, A.; Gauglitz, G.; Abuknesha, R. A. *Biosensors & Bioelectronics*, **1999**, vol. 14, no. 4, pp. 377-386.

17. Hutley, M.C. *Diffraction Gratings*, Academic Press Inc., New York and London, **1982**.

18. Jeffreys, H.; Jeffreys, B. S. *Methods of Mathematical Physics*, 2nd Ed., Cambridge University Press, **1950**, pp. 333-335.

19. Jorgenson, R. C. *Surface Plasmon Resonance Based Bulk Optic and Fiber Optic Sensors*, Ph.D. Thesis, University of Washington, **1993**, p. 97.

20. Jung, L. S.; Campbell, C.; Chinowsky, T. M.; Mar, M. N.; Yee, S. S. *Langmuir*, **1998**, vol. 14, no. 19, 15 Sept., pp. 5636-5648.

21. Karlsen, S. R.; Johnston, K. S.; Jorgenson, R. C.; Yee, S. S. *Sensors & Actuators B*, **1995**, vol. 24-25, pp. 747-749.

22. Melendez, J.; Carr, R.; Bartholomew, D. U.; Kukanskis, K.; Elkind, J.; Yee, S. S.; Furlong, C.; Woodbury, R. *Sensors & Actuators B*, **1996**, vol. 35-36, pp. 212-216.

23. Nelson, S. G.; Johnston, K. S.; Yee, S. S. *Sensors and Actuators B*, **1996**, vol. 35-36, pp.187-191.

24. Newton, R. *Scattering Theory of Waves and Particles*, McGraw-Hill, New York, **1966**.

25. Pedrotti, F. L.; Pedrotti, L. S. *Introduction to Optics*, Prentice-Hall Inc., Englewood Cliffs, **1987**.

26. Peiponen, K.; Raty, J.; Vartainen, E. M.; Sugiura, T.; Kawata, S. *Measurement Science and Technology*, **1999**, vol. 10, N145-N148.

27. Petit, R., ed. *Electromagnetic Theory of Gratings*, Springer-Verlag, Berlin, **1980**, Chapter 6.

28. Pipino, A. C. R. *SPIE Conference on Advanced Sensors and Monitors for Process Industries and the Environment*, SPIE vol. 3535, **1998**, pp. 57-67.

29. Schipper, E. F.; Kooyman, R. P. H.; Borreman, A.; Greve, J. *Biosensors & Bioelectronics*, **1996**, vol. 11, no. 3, pp. 295-304.

30. Skoog, D. A.; Leary, J. J. *Principles of Instrumental Analysis*, 4th edition, Saunders College Publishing, Fort Worth, **1992**, p. 47.

31. Smith, S. A.; Brodsky, A. M.; Burgess, L. W. "Nanoparticle Characterization in Nanoliter Volumes", submitted to *Analytical Chemistry*, April, **2000**.

32. Thomas, M. J. K. *Ultraviolet and Visible Spectroscopy*, 2nd Edition, John Wiley & Sons, Chichester, **1996**, p. 18.

33. Uppuluri, S.; Keinath, S. E.; Tomalia, D. A.; Dvornic, P. R. *Macromolecules*, **1998**, vol. 31, no. 14, pp. 4498-4509.

34. Van de Hulst, H. C. *Light Scattering by Small Particles*, John Wiley & Sons Inc., New York, **1957**.

35. for general information regarding the structure, production, and potential uses of dendrimers visit: **http:/www.mmi.org/mmi/dendritech**

VITA

Sean A. Smith

EDUCATION

Doctor of Philosophy, Analytical Chemistry (June, 2000)
- University of Washington, Seattle, WA
- Thesis: "Development of Grating Light Reflection Spectroscopy For Sensing Applications"
-Advisor: Dr. Lloyd W. Burgess

Bachelor of Science, Chemistry (1993)
- Trinity University, San Antonio, TX

PUBLICATIONS AND PRESENTATIONS

Sean A. Smith, Anatol M. Brodsky, Lloyd W. Burgess, "Dynamic Nanoparticle Characterization in Nanoliter Sampling Volumes Using Grating Light Reflection Spectroscopy", submitted to Analytical Chemistry April 2000.
Anatol M. Brodsky, Lloyd W. Burgess, Sean A. Smith, "Grating Light Reflection Spectroscopy", Applied Spectroscopy, vol. 52, no. 9, 1998, Focal Point Article.
"GLRS Application to Particle Analysis", 54th Northwest Regional Meeting of the American Chemical Society, 1999.
"Spectroelectrochemistry Using Grating Light Reflection Spectroscopy", Sandia Nat'l Laboratory public document, April 2000.
"Grating Light Reflection Spectroscopy", research presentations conducted at the Spring and Fall CPAC Semiannual Sponsor Meetings from Spring of 1995 to Spring of 2000.
A book review of Infinite Jest by David Foster Wallace in the University of Washington Daily. Visit URL:
www.thedaily.washington.edu/archives/1997_Spring/April31997